1-1-2006

Tensile properties, fracture toughness and crack growth study of alloy C-276

Joydeep Pal
University of Nevada, Las Vegas

TENSILE PROPERTIES, FRACTURE TOUGHNESS AND CRACK GROWTH STUDY OF ALLOY C-276

by

Joydeep Pal

Bachelor of Science in Engineering
Jadavpur University, Kolkata, India
July 2000

A thesis submitted in partial fulfillment
of the requirements for the

Master of Science Degree in Mechanical Engineering
Department of Mechanical Engineering
Howard R. Hughes College of Engineering

Graduate College
University of Nevada, Las Vegas
December 2006

UNLV
UNIVERSITY OF NEVADA LAS VEGAS

Thesis Approval

The Graduate College
University of Nevada, Las Vegas

9th November, 2006

The Thesis prepared by

Joydeep Pal

Entitled

Tensile Properties, Fracture Toughness and Crack Growth Study of Alloy C-276

is approved in partial fulfillment of the requirements for the degree of

Master of Science in Mechanical Engineering

Examination Committee Chair

Dean of the Graduate College

Examination Committee Member

Examination Committee Member

Graduate College Faculty Representative

ABSTRACT

Tensile Properties, Fracture Toughness and Crack Growth Study of Alloy C-276

by

Joydeep Pal

Dr. Ajit K. Roy, Examination Committee Chair
Associate Professor of Mechanical Engineering
University of Nevada, Las Vegas

The results of tensile testing involving austenitic Alloy C-276 indicated that this material is capable of maintaining adequate structural strength at temperatures relevant to the H_2SO_4 decomposition process related to the nuclear hydrogen generation. This alloy exhibited a unique phenomenon known as dynamic strain ageing, which has been studied as a function of both temperature and strain rate. An average value of 55 KJ/mole has been determined to be the activation energy for plastic deformation under tensile loading at different temperatures. Increased crack extension was observed in wedge-loaded double-cantilever-beam specimens exposed to an acidic solution and subjected to higher initial stress intensity factor values. The self-loaded specimens did not exhibit cracking in the same environment. Ductile failures were observed at temperatures up to 600°C. However, intergranular brittle failures were observed at higher temperatures.

TABLE OF CONTENTS

LIST OF TABLES

LIST OF FIGURES

ACKNOWLEDGMENTS

I am extremely happy to take this opportunity to acknowledge my debts of gratitude to them who are associated in the preparation of this thesis.

Words fail to express my profound regards from the inmost recess of my heart to my advisor Dr. Ajit K. Roy for the invaluable help, constant guidance and wide counseling extended by him right from the selection of topic to the successful completion of my thesis work.

I would like to thank my committee members, Dr. Anthony Hechanova, Dr. Daniel Cook and Dr. Edward Neumann, for their direct and indirect contribution throughout this investigation. Special thanks should be given to my project mates Lalit, Pankaj, Debajyoti, and all my colleagues at MPL, who helped me in many ways. I would also like to thank Dr. Chandan Mukhopadhyay for his immense help in my research.

Keeping separate space in my heart, I would like to thank my wife, **Ratnabali** for her great support and encouragement throughout my research.

The zeal, enthusiasm and inspiration provided by my parents Mr. D.C. Pal and Mrs. S. Pal are thankfully acknowledged. I would also like to thank my brother Sudip for his support.

Finally I would like to acknowledge the financial support of the United States Department of Energy (USDOE).

CHAPTER 1

INTRODUCTION

Fossil fuels have been extensively used throughout the world for quite sometime. Since the cost of fossil fuels is escalating at an alarming rate, substantial efforts are currently ongoing to identify and develop alternate sources of energy. Hydrogen is one such energy source, which is known to be available from many sources using techniques such as electrolysis of water. However, the cost of hydrogen generation using the conventional electrolysis technique is unusually high. In view of this rationale, the United States Department of Energy (USDOE) has initiated a bold step to generate hydrogen using thermochemical processes involving chemical reactions at elevated temperatures. The elevated temperatures needed for hydrogen generation will be provided by the nuclear power plants.

A thermochemical water-splitting cycle consists of a series of chemical reactions, some at rather high temperatures. Chemicals are chosen to create a closed loop, where water can be fed to the process, oxygen (O_2) and hydrogen (H_2) are produced and collected, and all other reactants are regenerated and recycled. The two leading thermochemical processes for generation of nuclear hydrogen are the sulfur-iodine (S-I) and the calcium-bromine (Ca-Br) cycles. However, the S-I cycle is preferred to the Ca-Br cycle by USDOE due to the maturity of the technology. The S-I process is described below.

1.1 S-I Cycle

The S-I process consists of three chemical reactions, which can lead to the generation of hydrogen. The S-I process involves chemical reactions to generate and decompose sulfuric acid (H_2SO_4) and hydrogen iodide (HI), respectively. The formation and decomposition of H_2SO_4 and HI occur at different temperatures, as illustrated in Figure 1-1. The formation of these chemical compounds is accomplished by activating chemical reactions among sulfur dioxide (SO_2), iodine (I_2) and water at 120°C. H_2SO_4 and HI are subsequently separated and transferred to two different reaction chambers. The decomposition of H_2SO_4 is proposed to occur at a maximum temperature of 950°C, leading to the formation of O_2, SO_2 and water. Simultaneously, HI will undergo decomposition within a temperature regime of 350-400°C, producing H_2 and I_2. The generated O_2 and H_2 are then transferred to two separate containers. Both SO_2 and I_2 are then recycled to react with water producing H_2SO_4 and HI, as shown in Figure 1-1. Thus, SO_2 and I_2 can act as catalysts to generate H_2SO_4 and HI, and the overall process is repeated.

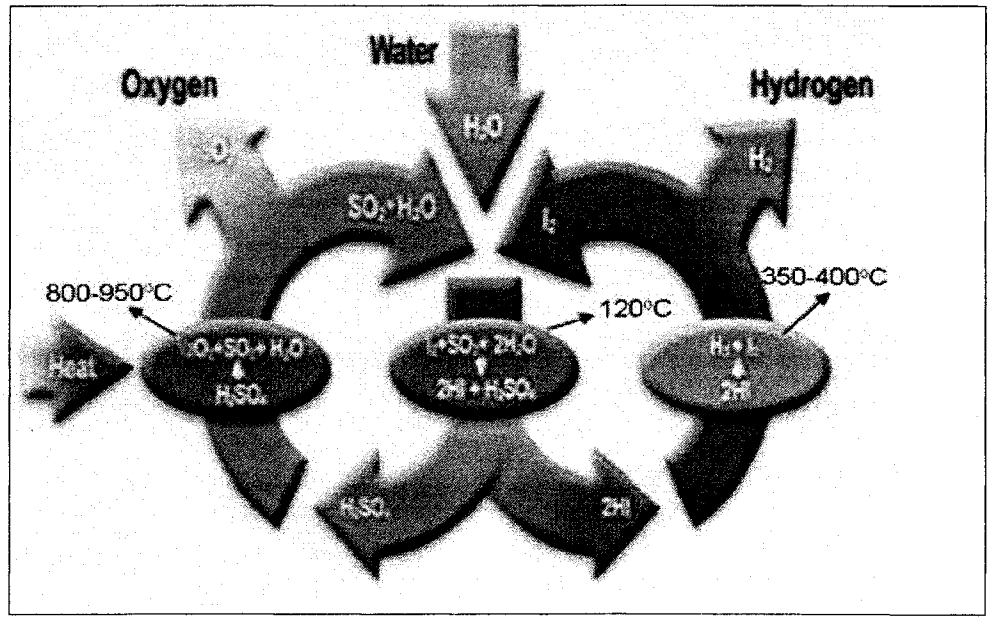

Figure 1-1 The S-I Water Splitting Cycle for Hydrogen Generation

The chemical reactions associated with the S-I cycle are shown below. An examination of these reactions reveals that the formation of HI and H_2SO_4 takes place at a substantially lower temperature compared to that of the H_2SO_4 decomposition process. The application of such an unusually high temperature (800-950°C) during the H_2SO_4 decomposition process is aimed at achieving the maximum possible efficiency in hydrogen generation through utilization of this thermochemical process. A lower operating temperature for H_2SO_4 decomposition would have resulted in a much reduced efficiency.

$I_2 + SO_2 + 2H_2O \rightarrow 2HI + H_2SO_4$ (Temperature ~ 120°C) Reaction 1-1

$H_2SO_4 \rightarrow H_2O + SO_2 + \frac{1}{2} O_2$ (Temperature ~ 800-950°C) Reaction 1-2

$2HI \rightarrow H_2 + I_2$ (Temperature ~ 350-400°C) Reaction 1-3

1.2 Objective of this Investigation

In light of the preceding discussion, it is obvious that the generation of H_2 using nuclear heat and thermochemical reactions is a major challenge to scientists and engineers. This challenge stems from the identification and selection of suitable structural materials possessing the desired metallurgical properties and corrosion resistance needed in successful generation of hydrogen under conditions relevant to the S-I process. A major requirement for the structural materials is their mechanical strength at elevated temperatures approaching almost 1000°C. Simultaneously, these materials have to withstand many hostile chemical species resulting from the formation and decomposition of H_2SO_4 and HI at elevated temperatures. Thus, the structural materials for nuclear hydrogen generation must demonstrate their superior tensile properties including strength and ductility at elevated temperatures, and exhibit excellent corrosion resistance in acidic environments with very low pH values.

The structural materials used in many industrial applications can undergo plastic instability at elevated temperatures. Such phenomenon of plastic instability can lead to reduced tensile strength and ductility. Thus, the identification of a suitable material with superior tensile strength will play a major role in nuclear hydrogen generation using the S-I process. These materials would also suffer from environment-induced degradations including localized corrosion, stress-corrosion-cracking (SCC) and general dissolution while exposed to hostile aqueous environments containing H_2SO_4 and HI. Therefore, the identification of suitable structural materials to circumvent the detrimental effects of elevated temperatures and aggressive chemical species is the first step in developing a strategic plan to generate hydrogen using the S-I cycle, as proposed by the USDOE. In

view of this judgment, a nickel-base Alloy C-276 has been identified as a candidate structural material for heat-exchanger application in the H_2SO_4 decomposition process under the proposed thermochemical cycle. Accordingly, an extensive investigation has been undertaken to evaluate the performance of this alloy for such application, the results of which will follow in the next few sections of this thesis.

Alloy C-276 (UNS N10276) [1] is a wrought nickel-chromium-molybdenum (Ni-Cr-Mo) superalloy possessing high strength, ductility and versatile corrosion resistance. The high strength, ductility and corrosion resistance of this alloy is attributed to the continuous matrix of face centered cubic (fcc) nickel-based solid solution of chromium (Cr), molybdenum (Mo), iron (Fe), cobalt (Co) and tungsten (W).[2] This alloy can provide excellent resistance to corrosion in a wide variety of chemical process environments. It is used in flue gas desulfurization systems because of its excellent resistance to degradation in the presence of sulfur compounds. [1] Alloy C-276 also exhibits enhanced resistance to corrosion in seawater, especially under crevice conditions. The high Mo content imparts the resistance to localized attack such as pitting. The presence of low carbon content in this alloy can also minimize carbide precipitation during welding, providing excellent resistance to intergranular attack in the heat-affected zones of many welded joints and structures. [3]

Alloy C-276 has a wide variety of industrial applications. It has been used in chemical processing, pollution control, pulp and paper production, industrial and municipal waste treatment and the recovery of sour natural gas. Its applications in air pollution control include stack liners, ducts, dampers, scrubbers, stack-gas re-heaters,

fans and fan housings. This alloy has also been used in chemical processing for components such as heat-exchangers, reaction vessels, evaporators and transfer piping. [3]

Since the maximum temperature proposed for H_2SO_4 decomposition process is in the vicinity of 800-950°C, the tensile testing of Alloy C-276 has been performed up to a maximum temperature of 1000°C to determine the structural strength and ductility. The magnitudes of tensile parameters including yield strength (YS), ultimate tensile strength (UTS) and ductility in terms of percent elongation (%El) and percent reduction in area (%RA) have been determined as a function of temperature. Since the structural integrity of an engineering component is known to be influenced by the presence of surface irregularities such as cracks, efforts have been made in this investigation to evaluate the fracture toughness of Alloy C-276 in the presence of a crack using a combination of linear-elastic and elastic-plastic fracture mechanics (LEFM and EPFM, respectively) concepts. Further, the crack propagation behavior of this alloy has been investigated using wedge-loaded fracture-mechanics-based specimens in the presence of an aqueous solution containing H_2SO_4. This method of loading is also capable of providing the stress intensity factor (K) of the specimen before and after exposure to the acidic solution.

The tensile data presented in this thesis have exhibited an interesting phenomenon of reduced ductility within a certain temperature regime. In addition, serrated engineering stress-strain (s-e) diagrams have been observed at some temperatures. Such phenomenon of reduced ductility and formation of serrations during tensile testing is the result of solute diffusion into the metal matrix, preferably at the grain boundary regions. The accumulation of these solute elements near the grain boundaries can impair the movement of lattice defects such as dislocations, thus causing reduced plastic flow even

under tensile loading. Such phenomenon, known as dynamic strain ageing (DSA), have been extensively studied by other investigators [4-7] involving martensitic T91 grade steel and austenitic Types 304 and 316 stainless steels. However, no technical or scientific data exist on the DSA behavior of Alloy C-276. Therefore, significant efforts have been made in this investigation to characterize the concentration of dislocations by transmission electron microscopy (TEM) involving tensile specimens tested in the susceptible temperature regime.

It is well-established that both temperature and strain rate can influence the DSA behavior of susceptible materials by virtue of their dependence on the resultant work-hardening index (n) and the activation energy (Q). [4 - 11] In view of this rationale, the effect of strain rate on the s-e diagrams have been studied by applying both faster and slower strain rates during tensile testing within the susceptible temperature regime. At relatively higher temperatures beyond this temperature regime, brittle failure can occur due to the formation of undesirable phases resulting from metallurgical transformations.[8] Therefore, efforts have also been made to characterize the brittle phases, if any, in specimens tested at elevated temperatures by using the x-ray diffraction (XRD) technique.

This thesis presents the results of tensile testing of Alloy C-276 at temperatures relevant to the S-I process at three different strain rates to develop a mechanistic understanding of DSA. The magnitudes of n and Q, determined from the experimental data, have been utilized to come up with a plausible explanation of the DSA behavior of this alloy, as influenced by both the temperature and strain rate. Since the estimation of the dislocation density in the vicinity of the grain boundaries is an alternate way of

characterizing DSA in a susceptible alloy, the calculated dislocation density (ρ) based on the TEM micrographs have also been presented. Since the presence of a flaw such as a crack on the material's surface can adversely influence its performance, the fracture toughness values of Alloy C-276, determined on pre-cracked specimens, have also been included. Further, a quantitative evaluation of the stress intensity factor and crack propagation rate of wedge-loaded specimens exposed to an acidic environment has been included in this thesis. Limited studies have also been performed to determine the corrosion rate based on the weight-loss of coupons immersed in an acidic solution for variable time periods. The susceptibility of Alloy C-276 to SCC has also been evaluated using self-loaded C-ring and U-bend specimens in an identical environment. Finally, the extent and morphology of failure of all tested specimens have been determined by scanning electron microcopy (SEM). In essence, this thesis has highlighted the overall performance capability of Alloy C-276 as functions of different metallurgical, experimental, and environmental variables.

CHAPTER 2

TEST MATERIAL, SPECIMENS AND ENVIRONMENT

2.1 Test Material

As described in the preceding section, the identification and selection of suitable structural materials for prospective application in nuclear hydrogen generation is a difficult task. The major challenge in this task is the identification of heat-exchanger materials having adequate structural strength and excellent corrosion resistance to withstand a hostile H_2SO_4 environment at temperatures approaching 1000°C. Therefore, an extreme caution was exercised to identify the most suitable materials for such applications. The National Materials Advisory Board, tasked with the preliminary identification of suitable candidate alloys, suggested the use of nickel-base alloys such as Alloy C-276. Subsequent to this recommendation, significant literature search [1-3, 12, 13] was performed by the investigators within the UNLV's materials community to justify the characterization of this alloy both from metallurgical and corrosion viewpoints. This effort led to a conviction that, while no technical data exist as to the metallurgical and corrosion aspects related to the operating conditions of nuclear hydrogen generation, it would be worthwhile to include Alloy C-276 as a candidate material for evaluation due to its overall performance, as cited in the open literature. [1-3]

The nickel-base Alloy C-276 was originally developed by the Haynes International Inc. for prospective use in modern day industrial applications due to its exceptional

capability to withstand severe operating conditions including hostile corrosive environments, elevated temperatures, high stresses and a combination of all these factors. The excellent ductility and toughness of this alloy can be attributed to its stable fcc crystal structure maintained even up to its melting temperature. The presence of Ni in this alloy enables significant plastic deformation in multiple slip planes, thus leading to enhanced ductility until it shows its tendency to failure under tensile loading. Further, the presence of high Cr content provides significantly high resistance to environment-induced degradations in normal atmosphere, sea water and acidic environments. [1, 3] This alloy is cited to be resistant to corrosive degradations in many strong acidic species such as H_2SO_4 and hydrochloric acid (HCl) even in the presence of chlorides. In addition, significant resistance to localized attack can be achieved with this alloy due to the presence of Mo. The high levels of Ni, Cr and Mo in Alloy C-276 make this alloy resistant to sour (H_2S) environments even at high temperatures in deep oil and gas wells.

Alloy C-276 is readily weldable and can outperform many commercially available stainless steels. This material can be used in the as-welded conditions, eliminating the need for post-weld thermal treatments. The presence of significantly low carbon and silicon contents in Alloy C-276 is beneficial to prevent grain boundary precipitation/segregation during heating cycles associated with the welding operations. The typical physical properties of Alloy C-276 are given in Table 2-1. [1]

Table 2-1 Physical Properties of Alloy C-276

Physical Property	Temperature(°C)	Metric Units
Density	22	8.89 g/cm^3
Melting Range	1323-1371	--
Electrical Resistivity	24	1.30 microhm-m
Mean Coefficient of Thermal Expansion	24-93	11.2 x 10^{-6}m/m.K
Thermal Conductivity	38	10.2 W/m.K
Specific Heat (Calculated)	Room	427 J/Kg.K

Alloy C-276, tested in this investigation, was procured from two different vendors in properly heat-treated conditions. This heat treatment included solution-annealing at 2050°F (1121°C) followed by rapid cooling, thus providing a fully austenitic microstructure. Both round and flat bars were procured to fabricate the desired types of test specimens. The chemical compositions and the tensile properties of three different heats of as-received bars of Alloy C-276 are given in Table 2-2 [1, 14] and 2-3 [1, 14], respectively. No additional thermal treatments were given to these materials prior to the fabrication of the test specimens.

Table 2-2 Chemical Composition of Alloy C-276 (wt %)

Heat No. / Element	2760 1 3939	2760 5 3882	Z4907CG
C	0.005	0.0045	0.004
Co	1.42	1.3659	0.18
Cr	15.87	15.65	15.71
Fe	5.43	5.36	5.44
Mn	0.52	0.5238	0.40
Mo	15.62	16.08	16.09
Ni	57.40	57.57	58.64
P	0.007	0.0079	0.009
S	0.003	0.0026	<0.001
Si	0.02	<0.02	0.044
V	0.15	0.1757	0.01
W	3.56	3.24	3.47

Table 2-3 Ambient-Temperature Tensile Properties of Alloy C-276

Heat No.	Yield Strength, Ksi (MPa)	Ultimate Strength, Ksi (MPa)	%El
2760 1 3939	50 (345)	114 (786)	64
2760 5 3888	53.5 (369)	110 (758)	65
Z4907CG	48.4 (334)	109.5 (755)	67.9

2.2 Test Specimens

Smooth cylindrical specimens were machined from round bars of Alloy C-276 for evaluation of the tensile properties at different temperatures. The fracture toughness of this alloy was evaluated by using compact-tension (CT) specimens based on conventional fracture-mechanics concepts. Further, fracture-mechanics-based double-cantilever-beam (DCB) specimens were fabricated from plate materials to evaluate the susceptibility of this alloy to stress-corrosion-cracking (SCC), and estimate the average crack growth rate under different stress intensity (K) values while exposed to an acidic solution for a variable time period. The cracking susceptibility in an identical environment was also evaluated by using self-loaded C-ring and U-bend specimens, made of similar material. In addition, rectangular coupons were tested for evaluation of their corrosion rates, and localized corrosion susceptibility in an identical environment.

2.2.1 Tensile Specimen

Cylindrical specimens having 4-inch (101.6 mm) overall length, 1-inch (25.4 mm) gage length, and 0.25-inch (6.35 mm) gage diameter were machined from round bars in such a way that the gage section was parallel to the longitudinal rolling direction. A ratio of 4 was maintained between the gage length and the gage diameter of these cylindrical specimens, as prescribed by the ASTM designated E 08-2004. [15] The configuration showing dimensions of this type of specimen and a pictorial view and are shown in Figure 2-1 (a and b).

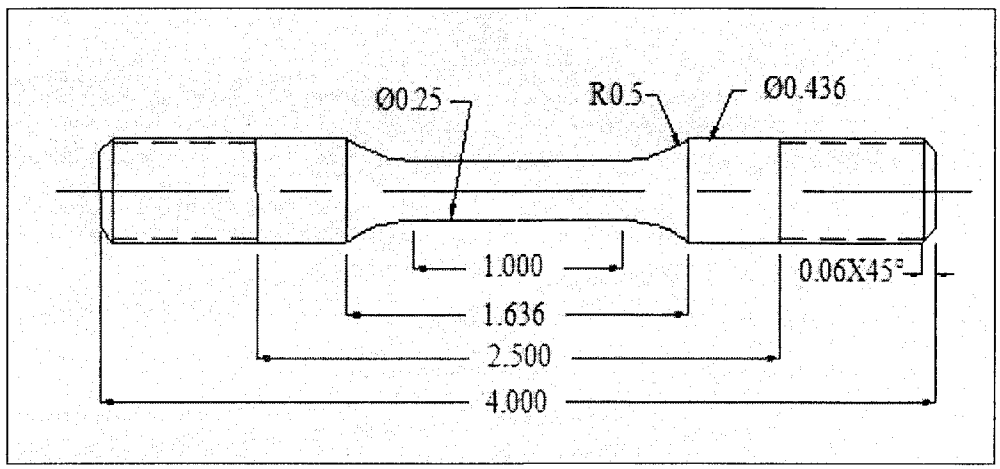

(a)

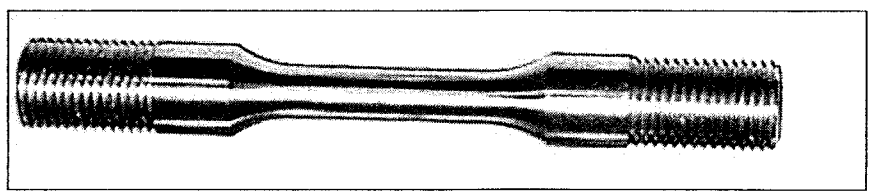

(b)

Figure 2-1 Smooth Cylindrical Specimen

2.2.2 Compact-Tension Specimen

For fracture toughness evaluation, pre-cracked CT specimens having 1.25-inches (31.75 mm) length, 1.2-inches (30.48 mm) width and 0.25-inch (6.35 mm) thickness (Figure 2-2) were used. The machining of these specimens was done to comply with the size requirements as prescribed by the ASTM designations E 399-1990, E 647-2000 and E 1820-2001. [16-18] The intersection of the crack starter notch tips with the two specimen surfaces were made equidistant from the top and bottom edges of the specimen within 0.005W, where W is the width of the specimen. A root radius of 0.003-inch (0.25 mm) was provided for the straight-through slot terminating in the V-notch of the specimen to facilitate fatigue pre-cracking at low stress intensity levels. A W/B ratio of 4 was maintained while machining the CT specimens [18], where B is the thickness of the specimen.

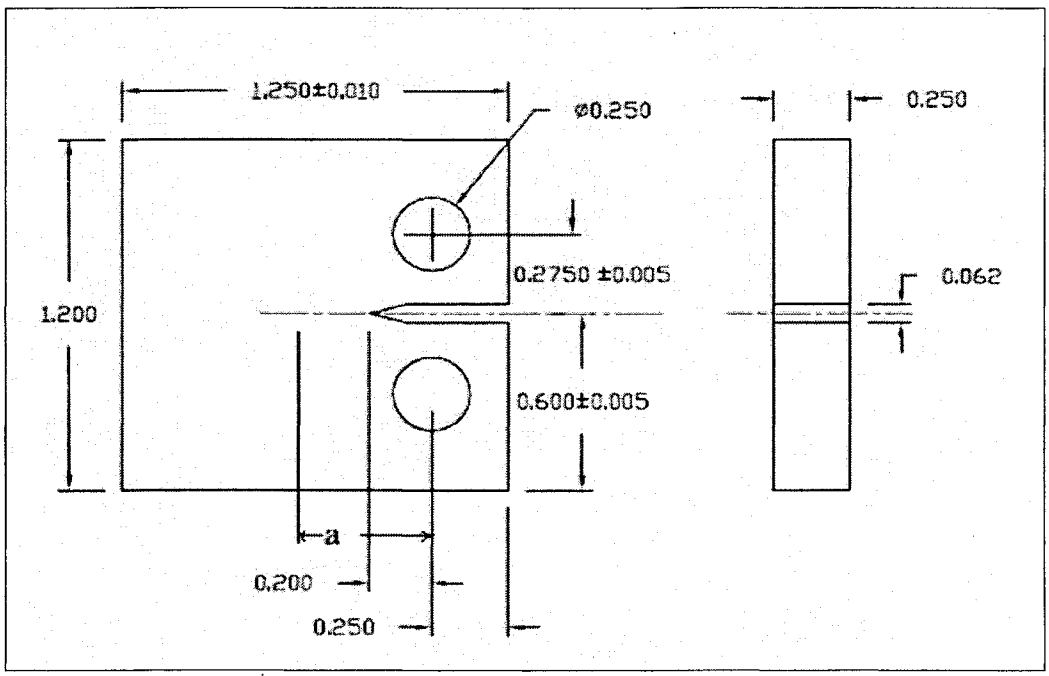

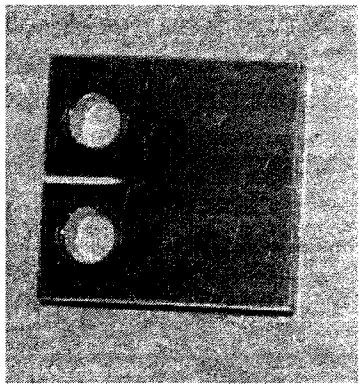

Figure 2-2 CT Specimen

2.2.3 Double-Cantilever-Beam Specimen

Rectangular DCB specimens, 4-inches (101.6 mm) long, 1-inch (25.4 mm) wide and 0.375-inch (9.525 mm) thick with one end slotted for wedge-loading and V-shaped side grooves extended from the slot to the opposite end, were used for the stress-corrosion-crack-growth study. These specimens were machined according to the NACE Standard TM0177-1990. [19] The side grooves were machined as 20% of the wall thickness, thus maintaining a web thickness (B_n) equal to 60% of the wall thickness (i.e. 0.225-inch or 5.715 mm in this case). The fabrication of the DCB specimens was done in such a way that the crack plane was perpendicular to the short transverse direction, thus ensuring that crack propagation would occur in the longitudinal rolling direction. Machining of the side grooves was done carefully to avoid overheating and cold working. The final two passes in machine operations removed a total of 0.002-inches (0.05 mm) of the metal.

The pre-cracked DCB specimens were loaded by inserting double taper wedges, made of Alloy C-276, into the specimen slots. Wedges of different thickness were inserted into the DCB slot to apply the desired load. Thus, the arm-displacement due to the insertion of the wedge resulted in different initial stress intensity factor values. The thickness of the

wedges varied from 0.113-inch (2.8702 mm) to 0.1235-inch (3.1369 mm) to provide specimen arm-displacement of 0.0176-inch (0.447 mm) to 0.023-inch (0.5842 mm), as shown in Table 2-4. The dimensions of the DCB specimen, and a pictorial view of the wedge-loaded DCB specimen are illustrated in Figure 2-3 (a and b).

Table 2-4 DCB Wedge Configurations

Specimen No.	Specimen arm-displacement inch. (mm)	Wedge Thickness inch. (mm)
1	0.0176 (0.447)	0.113 (2.870)
2	0.02 (0.508)	0.121 (3.073)
3	0.023 (0.584)	0.1235 (3.137)
4	0.015 (0.381)	0.114 (2.896)
5	0.023 (0.584)	0.123 (3.124)
6	0.021 (0.533)	0.123 (3.124)

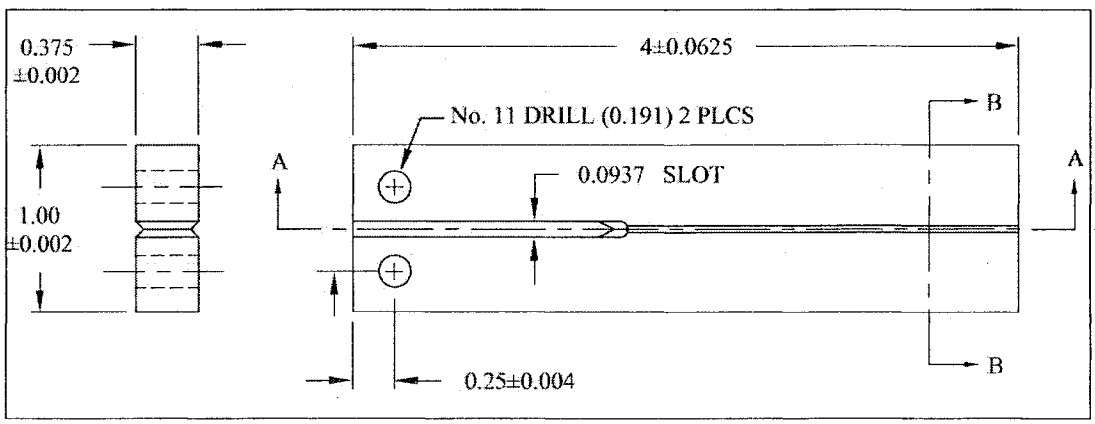

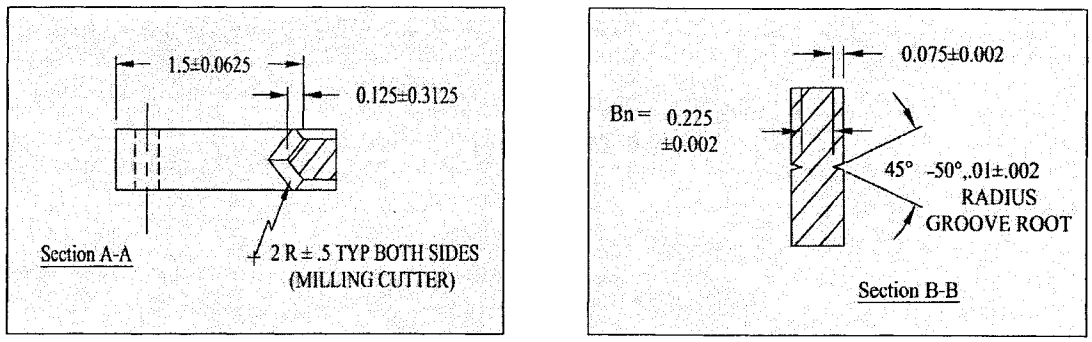

(a)

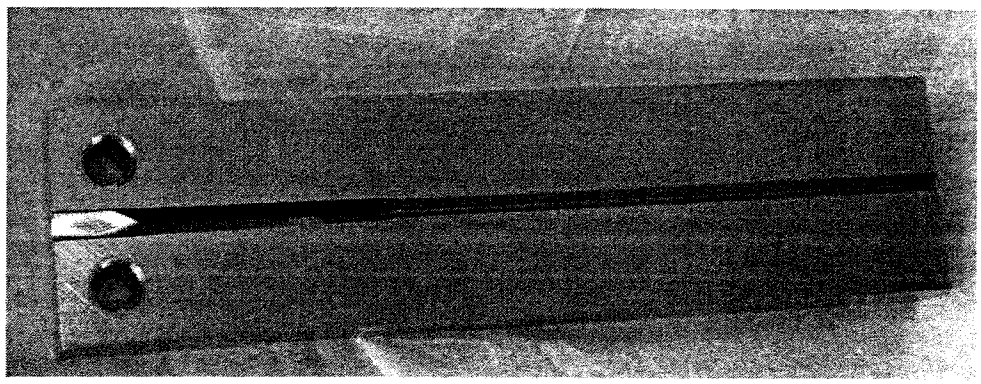

(b)

Figure 2-3 DCB Specimen

2.2.4 C-ring and U-bend Specimens

A limited number of SCC tests were performed in an acidic solution using C-ring and U-bend specimens. The fabrications of the C-ring and U-bend specimens were done according to ASTM designations G 38-2001 [20] and G 30-1997 [21], respectively, in such a way that the resultant tensile stress on the convex surface was parallel to the longitudinal rolling direction. Both the C-ring and U-bend specimens were loaded with bolts made of a similar material to prevent galvanic corrosion. The configurations and the

pictorial views of the C-ring and U-bend specimens are shown in Figures 2-4 and 2-5, respectively.

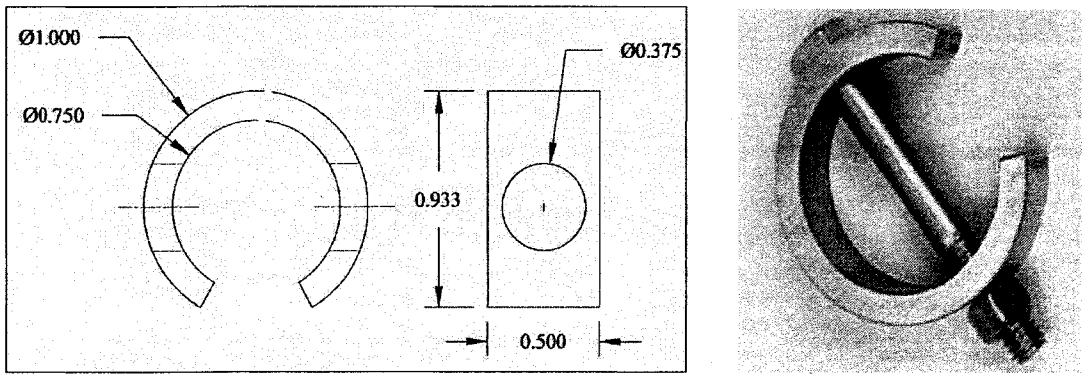

Figure 2-4 C-ring Specimen

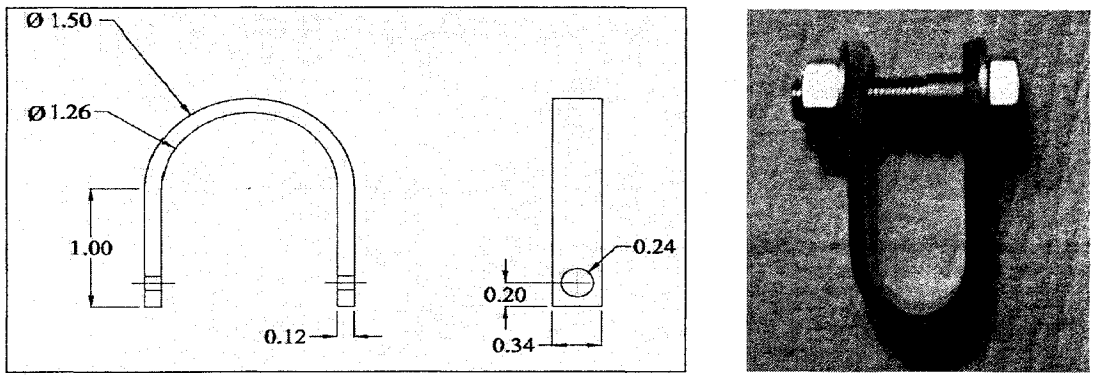

Figure 2-5 U-bend Specimen

2.2.5 Coupon

Rectangular coupons were used to determine the corrosion rate based on weight-loss due to their exposure into an acidic solution for variable time periods. These coupons had 1.25-inches (31.75 mm) length and 0.75-inch (19.05 mm) width. A circular hole of 0.25-inch (6.35 mm) diameter was machined near the top edge of the coupon (Figure 2-6)

to insert a glass rod having grooves to hold it in a glass sample holder while immersing it in the solution contained in an autoclave.

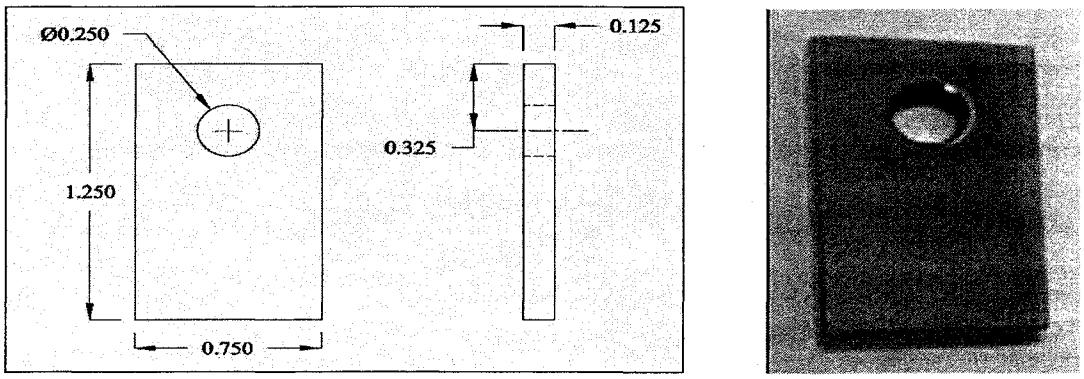

Figure 2-6 Coupon

2.3. Test Environment

Environment can have a profound influence on the performance of structural materials to be used in heat-exchangers related to the nuclear hydrogen generation process. Even though the S-I process involves the formation and decomposition of H_2SO_4 and HI at different temperatures, a prototypic environment could not be accommodated in the current investigation. Further, the present study is primarily focused on the decomposition of H_2SO_4 alone at relatively high temperatures approaching 1000°C. Therefore, an effort was made to evaluate the corrosion behavior of Alloy C-276 in an aqueous solution containing H_2SO_4 at the highest possible temperature achievable at the Materials Performance Laboratory.

An autoclave containing this acidic solution was used to characterize the different modes of degradations that can be expected to occur. In general, a metallic material can experience degradations such as general dissolution, localized attack (pitting and crevice)

and embrittlement under a synergistic effect of applied/residual stress and a potent environment while exposed to a hostile acidic solution. The susceptibility of Alloy C-276 to these degradations was, therefore evaluated in an acidic solution having a composition, as shown in Table 2-5.

Table 2-5 Chemical Composition of Test Solution

Solution (pH)	Deionized Water (ml)	H_2SO_4
Acidic (1.0)	4000	Added to adjust the desired pH

CHAPTER 3

EXPERIMENTAL PROCEDURES

The tensile properties of Alloy C-276 were determined at temperatures ranging from ambient to 1000°C by using an Instron mechanical testing system. The evaluation of fracture toughness using pre-cracked CT specimens was also performed using this equipment. This equipment was also used to determine the initial stress intensity factor (K_I) using wedge-loaded DCB specimens. The evaluation of the susceptibility of this alloy to SCC and the determination of crack propagation, and the final K_I value upon exposure to the test solution was accomplished by immersing the pre-cracked and wedge-loaded DCB specimens inside an autoclave. SCC determination using self-loaded C-ring and U-bend specimens, and weight-loss determination using coupons were performed by exposing them inside the same autoclave. The metallographic and fractographic evaluations of all tested specimens were conducted by using optical microscopy and SEM, respectively. The characterizations of defects, and secondary phases resulting from transformation at higher testing temperatures were performed by TEM and XRD, respectively. The detailed experimental procedures are described in the following subsections.

3.1 Tensile Testing

The tensile properties including the yield strength (YS), ultimate tensile strength (UTS), and the ductility in terms of percent elongation (%El) and percent reduction in

area (%RA) was evaluated using the Instron model 8862 equipment. The smooth cylindrical specimens were loaded in tension at a strain rate of 5×10^{-4} sec^{-1} according to the ASTM Designation E 8-2004. [15] Three specimens were tested under each experimental condition, and the average values of the measured parameters were recorded. The experimental data including the load, engineering stress and strain were recorded in the data file. The engineering stress versus strain (s-e) diagrams were automatically generated using the Bluehill 2 software program [22] that enabled the data acquisition during tensile testing. The magnitudes of YS, UTS and %El (based on the Linear Variable Displacement Transducers) at each temperature were also determined using this software. Upon completion of testing, the ductility parameters (%El and %RA) were calculated using Equations 3-1 through 3-4.

$$\%\ El = \left(\frac{L_f - L_o}{L_g} \right) \times 100 \qquad \text{Equation 3-1}$$

$$\%RA = \left(\frac{A_o - A_f}{A_o} \right) \times 100 \qquad \text{Equation 3-2}$$

$$A_o = \frac{\pi \times D_o^{\,2}}{4} \qquad \text{Equation 3-3}$$

$$A_f = \frac{\pi \times D_f^{\,2}}{4} \qquad \text{Equation 3-4}$$

Where, A_0 = Initial cross sectional area ($inch^2$)

A_f = Cross sectional area at failure ($inch^2$)

L_o = Initial overall length (inch.)

L_f = Final overall length (inch.)

L_g = Initial gage Length (inch.)

D_o= Initial gage diameter (inch.)

D_f= Final gage diameter (inch.)

The Instron testing machine, shown in Figure 3-1, had an axial load transducer capacity of 22.5 kip (100 kN). It had a single screw electromechanical top actuator that was developed for static and quasi-dynamic cyclic testing at slow speed. This equipment consisted of a large heavy-duty load frame with an adjustable crosshead attached to the top grip, and a movable actuator with another grip at the bottom to enable loading and unloading of the test specimen. The axial motion was controlled by force, displacement, or an external signal from the strain gage. The specimen was mounted between the two grips and pulled by the movable actuator. The load cell measured the applied force on the tensile specimen. The movement of the upper crosshead relative to the lower one measured the strain within the specimen and consequently, the applied load. The key specifications of the Instron equipment are given in Table 3-1. [23]

Table 3-1 Specifications of Instron Model 8862 System

Load Capacity	Total Actuator Stroke	Maximum Ramp Rate	Actuator Attachment Threads	Load Cell Attachment Threads
100 kN	100 mm	350 mm/min	M30 × 2	M30 × 2

A split furnace (model MDS1735A) was attached to the testing system for evaluating the tensile properties at elevated temperatures in the presence of nitrogen. This furnace was capable of sustaining a maximum temperature of 1500°C, and consisted of two water-cooled stainless steel jackets that provided a safe ergonomic outer surface for operation. This furnace had two layers of micro-pores and ceramic fibers over them. Six U-shaped molybdenum disilicide heating elements were used for attaining the desired testing temperature. The specimen temperature during straining was monitored by three B-type thermocouples contained inside the test chamber. A separate control panel (model CU666F) was used to perform the overall monitoring of temperature during tensile loading. A maximum heating rate of 10°C per minute could be achieved by this control panel. However, a slow heating rate of 4°C per minute was used during testing to prevent any thermal shock of the pull rods and the fixtures inside the furnace. Since the grip material could undergo phase transformation and plastic deformation at elevated temperatures during straining of the specimen, a pair of custom-made grips of high strength and temperature resistant MarM 246 alloy was used to hold the tensile specimen in an aligned position. A positive pressure inside the heating chamber was maintained by continuously purging nitrogen through it, which also ensured the elimination of oxygen from the test chamber, thereby preventing surface contamination of the specimen.

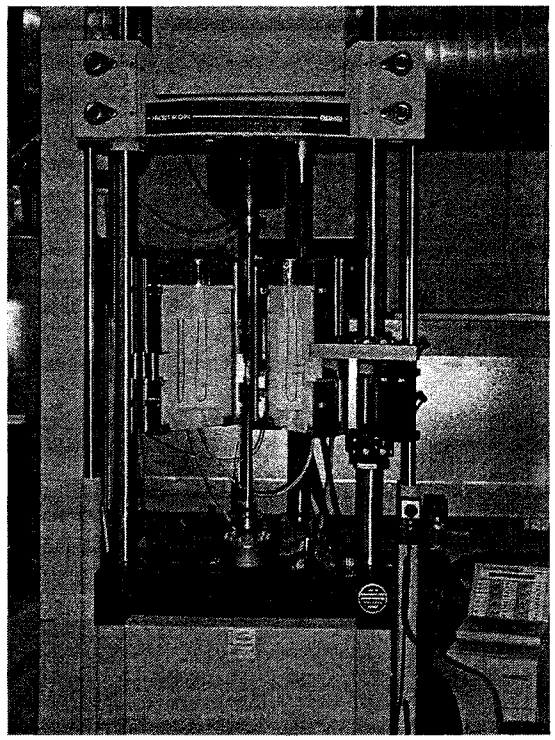

Figure 3-1 Instron Testing Machine

3.1.1 Activation Energy Evaluation

As mentioned in an earlier section, the phenomenon of DSA showing reduced failure strain and serrations within a certain temperature regime, is a function of both temperature and strain rate. The gradual reduction in failure strain (e_f) was initially observed at an applied strain rate of 5×10^{-4} sec^{-1}. In order to study the effect of strain rate on the DSA behavior of Alloy C-276, two additional strain rates, above and below this rate (i.e., 10^{-3} and 10^{-4} sec^{-1}, respectively) were later used within the susceptible temperature range for DSA to occur. Since the magnitude of e_f was higher at 450°C, additional tensile testing was conducted at this temperature using these two strain rates. A minimum of two tests was performed at all three strain rates at temperatures within and above the susceptible temperature regime that exhibited DSA tendency of Alloy C-276.

It is well-known [8-10] that the occurrence of DSA is the result of the diffusion of interstitial and substitutional solute elements into the matrix of a susceptible material. Since diffusion is a thermally-activated process, the determination of the activation energy (Q) based on the testing temperatures seems appropriate to develop a fundamental understanding of the mechanism of plastic deformation of the tested alloy. Further, it has been suggested [8-10, 24, 25] that the critical plastic strain (ε_c) to initiate the formation of serrations is a function of both the temperature and strain rate ($\dot{\varepsilon}$) according to the following equation. [24, 25]

$$\varepsilon_c^{(m+\beta)} = K\dot{\varepsilon}\exp\left(\frac{Q}{RT}\right) \qquad \text{Equation 3-5}$$

Where, Q = Activation energy at the onset of serrations (KJ/mole)

R = Universal Gas Constant (0.83144 KJ/mole K)

T = Absolute temperature (K)

m, β = Exponents related to the variation of vacancy concentration (C_v) and mobile dislocation density (ρ_m)

K = Constant

It has been postulated [8, 9] that C_v and ρ_m can be related to the true strain (ε) according to the following empirical relationships, shown by Equations 3-6 and 3-7. The magnitude of Q can be determined by using two methods. The first method [8, 9] is based on the application of Equation 3-5, in which the natural logarithm of ε_c is plotted as a

function of $\frac{1}{T}$ at a constant $\dot{\varepsilon}$, thus giving a straight line having a slope of $\frac{Q}{R(m+\beta)}$. A mathematical treatment of this method of Q calculation can be given, as shown below.

$$C_v \propto \varepsilon^m \qquad \text{Equation 3-6}$$

$$\rho_m \propto \varepsilon^\beta \qquad \text{Equation 3-7}$$

As shown earlier, $\varepsilon_c^{(m+\beta)} = K\dot{\varepsilon}\exp\left(\frac{Q}{RT}\right)$ Equation 3-5

Taking natural logarithm (ln) on both sides of Equation 3-5,

$$\ln \varepsilon_c^{(m+\beta)} = \ln\left[K\dot{\varepsilon}\exp\left(\frac{Q}{RT}\right)\right]$$

$$\text{Or, } (m+\beta)\ln\varepsilon_c = \ln K + \ln\dot{\varepsilon} + \left(\frac{Q}{RT}\right)$$

$$\text{Or, } \ln\varepsilon_c = \frac{Q}{R(m+\beta)} \times \frac{1}{T} + \frac{\left(\ln K + \ln\dot{\varepsilon}\right)}{(m+\beta)} \qquad \text{Equation 3-8}$$

Equation 3-8 represents a straight line in the form of y = Ax + B, where A is the slope of the straight line expressed as $\frac{Q}{R(m+\beta)}$. Equation 3-5 can also be rearranged, as shown by Equation 3-9, which represents a straight line with a slope of $(m+\beta)$ when $\ln\dot{\varepsilon}$ is

plotted as a function of $\ln \varepsilon_c$ at a constant T. Knowing the value of $(m+\beta)$, the magnitude of Q can be determined from the slope $\left(\frac{Q}{R(m+\beta)}\right)$, as shown in Equation 3-8.

$$\ln \dot{\varepsilon} = (m+\beta)\ln \varepsilon_c - \left[\ln K + \frac{Q}{RT}\right] \qquad \text{Equation 3-9}$$

The second method [8, 9] of Q calculation is based on the McCormick's strain aging model which is governed by the following equation. [26]

$$\frac{\varepsilon_c^{(m+\beta)}}{T} = \left(\frac{C_1}{\phi C_0}\right)^{3/2} \frac{kb}{LNU_m} \frac{\exp(Q/kT)}{D_0} \dot{\varepsilon} \qquad \text{Equation 3-10}$$

Where, C_0 = Initial concentration of solute in the alloy

C_1 = The local concentration of the solute at dislocation

L = The obstacle spacing

U_m = The maximum solute-dislocation interaction energy

D_0 = The frequency factor

b = The Burger's vector

k = Boltzman constant (1.3807×10^{-23} J/K)

N and ϕ = Constants

Taking natural logarithm (ln) on both sides of Equation 3-10, one can get an expression, given by Equation 3-11. Once again, this equation represents a straight line with a slope

of $\frac{Q}{k}$ when $\ln\left[\frac{\varepsilon_c^{(m+\beta)}}{T}\right]$ is plotted as a function of $\frac{1}{T}$ at a constant $\dot{\varepsilon}$. Substituting a standard value of k in this slope, one can determine the magnitude of Q. [8, 10, 26] A comparative analysis of the Q values calculated by the two methods will be presented in Chapter 4 of this thesis.

$$\ln\left[\frac{\varepsilon_c^{(m+\beta)}}{T}\right]=\frac{Q}{k}\left(\frac{1}{T}\right)+\ln\left[\left(\frac{C_1}{\phi C_0}\right)^{3/2}\frac{kb}{LNU_m D_0}\dot{\varepsilon}\right] \qquad \text{Equation 3-11}$$

3.1.2 Computation of Strain Hardening Exponent

Metallic materials can experience work hardening resulting from dynamic loading beyond the elastic limit. [27] The extent of work hardening, commonly expressed as the strain hardening exponent, is known to be related to both the true stress and true strain by the equation given below. [27, 28] This equation is also known as the Hollomon relationship. [29, 30]

$$\sigma = K\varepsilon^n \qquad \text{Equation 3-12}$$

Where, σ = True stress (ksi or MPa)

ε = True strain

n = Strain hardening exponent

K = Constant, known as strain hardening (strength) coefficient

Under an ideal condition, the magnitude of n can be determined from the slope of a straight line obtained by plotting $\log\sigma$ vs. $\log\varepsilon$ at a constant temperature. However, depending on the test material, a linear relationship between $\log\sigma$ and $\log\varepsilon$ may not always be achieved. [29, 31, 32] Rather, a non-linear relationship between $\log\sigma$ and $\log\varepsilon$ can be seen in some nickel-base alloys. [31, 32, 34, 35] In view of this rationale, an alternate relationship had been proposed by Ludwigson [33] that includes a second term (Δ) in Equation 3-12, as shown by Equation 3-13. In this equation, $\Delta = \exp\left(K_1 + n^1\varepsilon\right)$ and K_1 and n^1 are the intercept and the slope of a line, respectively generated from the plot of $\log\Delta$ vs. $\log\varepsilon$.

$$\sigma = K\varepsilon^n + \Delta \qquad \text{Equation 3-13}$$

Under such a non-ideal condition, the magnitude of n can be determined from the plot of $\log\sigma$ vs. $\log\varepsilon$ using the best linear part of the resultant non-linear shape of this plot. A superimposition of both the linear and non-linear relationships between $\log\sigma$ and $\log\varepsilon$ is illustrated in Figure 3-2. As shown in this figure, the linear portion of Ludwigson's curve coincides with the straight line obtained from the conventional Hollomon relationship between σ and ε. Such coincidence of both plots occurs at relatively higher strain (ε) values. The magnitudes of n at different temperatures and strain rates can eventually be determined using the true strain values corresponding to this linear portion of the superimposed plots. [29-32] It should be noted that a minimum value of Δ was taken into consideration to determine n using this approach.

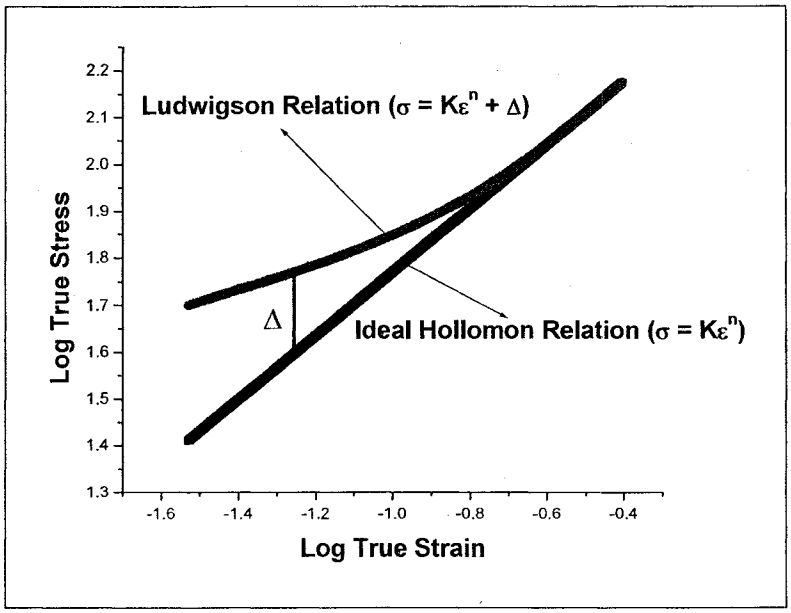

Figure 3-2 Hollomon vs. Ludwigson σ vs. ε Plot

3.2 Fracture Toughness Evaluation

The determination of the plane strain fracture toughness (K_{IC}) of Alloy C-276 was accomplished by using CT specimens in the Instron 8862 testing equipment according to ASTM Standard E 399-1990. [16] The CT specimens were pre-cracked up to a maximum length of 2 mm at a stress ratio ($R = \frac{\sigma_{min}}{\sigma_{max}}$) of 0.1 using an applied load below the material's yield point at a frequency of 1 Hz. The testing was performed using the K_{IC} Fracture Toughness Software Program provided by the Instron Corporation. An extensometer was attached to the test specimen during straining of the CT specimen at a rate of 2 mm per minute to determine the conditional stress intensity factor (K_Q) value. Depending on the type of the test material, three different types of load-displacement (P vs. v) curves are obtained, as illustrated in Figure 3-3. [16, 17] Type I represents a classical P vs. v plot for ductile materials such as Alloy C-276. A line OA was drawn

tangent to the initial linear portion of this curve. A second line OB, known as the 5% secant line, with a slope equal to 95% of the initial load line, was then drawn. The point at which the load-displacement curve intersected the 5% secant line determined a point represented by P_5. The load value at P_5 was taken as the critical or conditional load (P_Q), which was used to calculate K_Q according to the Equation 3-14.

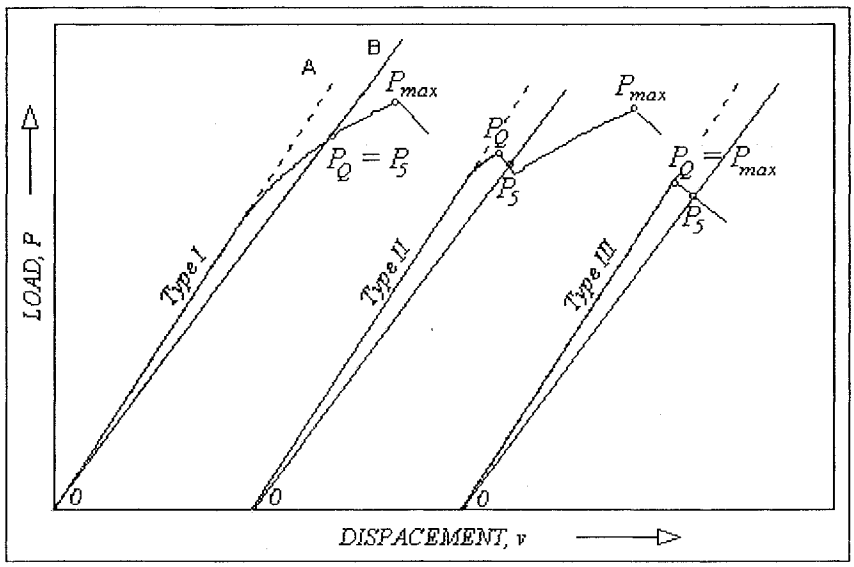

Figure 3-3 Three Types of Load-displacement Curves

$$K_Q = \frac{P_Q}{B\sqrt{W}} f\left(\frac{a}{W}\right) \qquad \text{Equation 3-14}$$

Where, B = Specimen thickness (mm)

a = Crack length (mm)

W = Specimen width (mm)

$f\left(\frac{a}{W}\right)$ = A dimensionless function of a/W, also known as geometric factor, determined using the following equation. [16, 17]

$$f\left(\frac{a}{W}\right)=\frac{\left[2+\frac{a}{W}\right]\left[0.886+4.64\frac{a}{W}-13.32\left(\frac{a}{W}\right)^2+14.72\left(\frac{a}{W}\right)^3-5.6\left(\frac{a}{W}\right)^4\right]}{\left(1-\frac{a}{W}\right)^{\frac{3}{2}}}$$

Equation 3-15

The resultant K_Q value, obtained by this method, is considered to be a valid K_{1C}, if the following relationships are met. [16, 17]

$$0.45 \le \frac{a}{W} \le 0.55 \qquad \text{Equation 3-16}$$

$$P_{\max} \le 1.1P_Q \qquad \text{Equation 3-17}$$

$$a, b, (W-a) \ge 2.5\left(\frac{K_Q}{\sigma_{YS}}\right)^2 \qquad \text{Equation 3-18}$$

Where, P_{max} = Maximum load

σ_{YS} = Yield strength of the test material

3.3 Stress-corrosion-cracking

SCC tests were performed in an autoclave using self-loaded specimens including DCB, C-ring and U-bend in an aqueous solution containing H_2SO_4 having a pH value of 1.0

3.3.1 SCC Testing using DCB Specimens

The DCB specimens were loaded by inserting double-tapered wedges of different thickness into their slots. [36] Prior to their loading, they were pre-cracked up to a length of 2 mm in the Instron equipment according to ASTM standard E 399–1990. [16] A cyclic loading with a R value of 0.1 and frequency of 1 Hz was used during pre-cracking. The thickness of the wedge was determined based on the displacements corresponding to different load levels within the elastic limit of Alloy C-276. Three sets of load and displacement were selected to load the DCB specimens by inserting wedges of different thickness. The wedge thickness was calculated using the following equation.

$$W = t + \delta \qquad \text{Equation 3-19}$$

Where, W = Wedge thickness

t = Initial gap between the two arms of the DCB specimen

δ = Displacement corresponding to the desired load (from the load-displacement plot)

The initial stress intensity factor (K_I) was computed using Equation 3-20, as prescribed by the Nace Standard TM0177-1990. [19] The wedge-loaded specimens were then

immersed into the acidic solution contained in an autoclave for periods of 15 and 30 days, respectively.

$$K = \frac{Pa\left(2\sqrt{3} + 2.38h/a\right)\left(B/B_n\right)^{1/\sqrt{3}}}{Bh^{3/2}} \qquad \text{Equation 3-20}$$

Where, P = Wedge load (before or after exposure to the environment), measured in the loading plane (lb-force)

a = The initial or final crack length, measured from the load line (inch.)

h = The height of each arm (inch.)

B = The specimen thickness (inch.)

B_n = The web thickness (inch.)

Upon completion of testing, the specimens were pulled apart in the Instron machine and the final crack length was measured on the broken faces. The final load and the crack length were used to calculate the final stress intensity factor for SCC (K_{1SCC}). Fractographic studies were subsequently conducted on the broken specimens to determine the mode of fracture.

3.3.2 SCC Testing with C-ring and U-bend Specimens

A limited number of C-ring and U-bend specimens of Alloy C-276 was tested in the acidic solution contained in the autoclave at 150°C, for variable periods of 7, 14, 28 and 56 days, to evaluate the effect of the circumferential stress on the cracking susceptibility of this material. Even though the autoclave (Figure 3-4) was designed to sustain a maximum temperature of 600°C and high pressures, testing could not be performed beyond 150°C. Leaks started at temperature above 150°C.

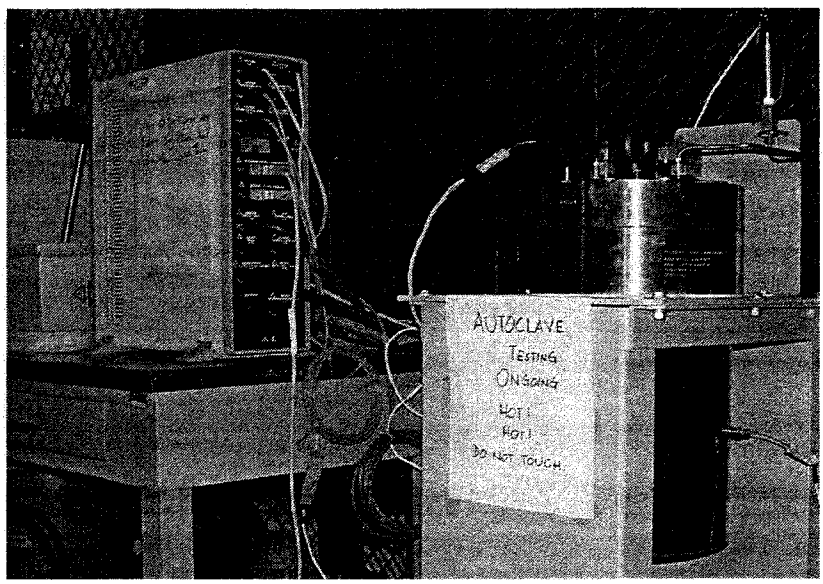

Figure 3-4 Autoclave System

The C-ring specimens were loaded at 98% of the material's ambient temperature YS value according to the ASTM designation G 38-2001. [20] The displacement (Δ) of the outer diameter of the C-ring specimen was calculated using Equation 3-21. A correction factor (Z) for the curved beam was obtained using Figure 3-5 [20] based on the ratio of the mean diameter to the wall thickness of the C-ring specimen.

$$OD_f = OD_i - \Delta \qquad \text{Equation 3-21}$$

Where, $\Delta = \dfrac{f \Pi D^2}{4EtZ}$

OD_f = Outside diameter of the stressed C-ring specimen

OD_i = Outside diameter before stressing

f = Desired stress (psi)

Δ = Change of outer diameter after applying the desired stress

D = Mean diameter (OD_i-t)

t = Wall thickness

E = Modulus of elasticity

Z = Correction factor for curved beam

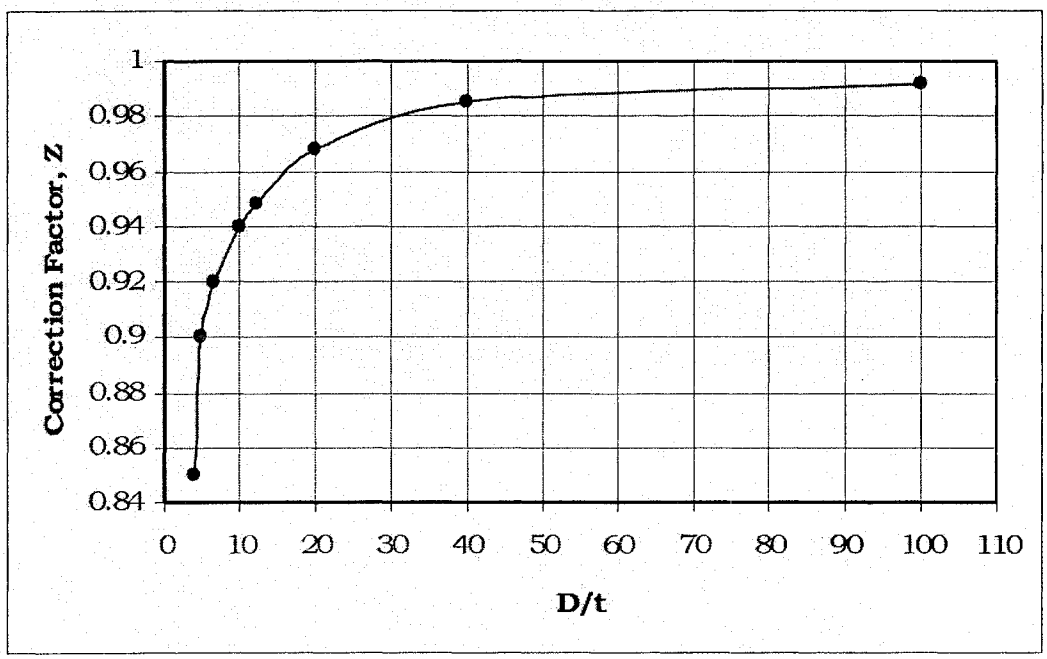

Figure 3-5 Correction Factor for Curved Beams

The U-bend specimens were loaded with bolts according to the ASTM designation G 30-1997. [21] The applied stress for the U-bend specimens was varied with different deflections of two legs from the original position. A line was marked with a constant distance between the two legs. The distance between the two legs at the marked points was measured. This distance between the two legs at these points was varied for

application of load of different magnitude. After the test, both the C-ring and U-bend specimens were visually examined for cracks on the convex surface, which is expected to undergo sustained tensile loading. [37]

3.4 General Corrosion Testing

Rectangular coupons of Alloy C-276 were immersed in the H_2SO_4 solution contained inside the autoclave at 150°C for periods of 7, 14, 28 and 56 days to determine the weight-loss. The average corrosion rate, based on duplicate specimens, was then calculated from the weight-loss according to Equation 3-22. [38]

$$mpy = \frac{534W}{DAT} \qquad \text{Equation 3-22}$$

Where, mpy = Corrosion rate in mils per year

W = Weight-loss in milligrams

D = Density of the material in gms/cm^3

A = Total exposed surface area of the specimen in sq.inch.

T = Total exposure time (test duration) in hrs

3.5 Metallographic Evaluations

The metallographic technique using an optical microscope enables the characterization of phases present, their distributions within grains and their sizes that depend on the chemical composition and the thermal treatments of the test material. The principle of an optical microscope is based on the impingement of a light source perpendicular to the test specimen. The light rays pass through the system of condensing lenses and the shutters up to the half-penetrating mirror. This brings the light rays

through the objective to the surface of the specimen. Light rays are reflected off the surface of the sample, which then return to the objective, where they are gathered and focused to form the primary image. This image is then projected to the magnifying system of the eyepiece. The contrast observed under the microscope results from either an inherent difference in intensity or wavelength of the light absorption characteristics of the phases present. It may also be induced by preferential staining or attack of the surface by etching with a chemical reagent.

The test specimen was sectioned and mounted using the standard metallographic technique, followed by polishing and etching to reveal the microstructures. The etchant used was "Glyceregia", composed of 15 ml of concentrated hydrochloric acid (HCl), 10 ml of glycerol and 5 ml of concentrated nitric acid (HNO_3). [39, 40] The polished and etched specimen was then evaluated for its microstructure by using a Leica optical microscope, shown in Figure 3-6. This microscope was capable of evaluation with a resolution of up to 1000X. A digital camera with a resolution of 1 Mega pixel enabled the image capture on a computer screen, utilizing the Leica software.

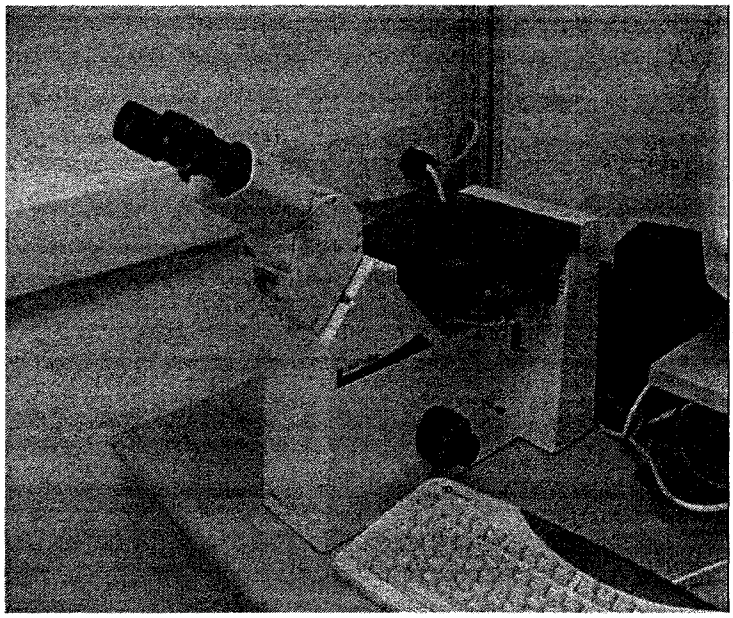

Figure 3-6 Leica Optical Microscope

3.6 Fractographic Evaluations

The extent and morphology of failure of the tested tensile specimens were determined by a Scanning Electron Microscope (SEM). Analysis of failure in metals and alloys involves identification of the type of failure. The test specimens were sectioned into 1/2 to 3/4 of an inch in length to accommodate them in the vacuum chamber of the SEM. Failures can usually be classified into two types including ductile and brittle. [58] Dimpled microstructure is a characteristic of ductile failure. Brittle failure can be of two types, intergranular and transgranular. An intergranular brittle failure is characterized by crack propagation along the grain boundaries while a transgranular failure is characterized by crack propagation across the grains.

In SEM evaluations, electrons from a metal filament are collected and focused, just like light waves, into a narrow beam. The beam scans across the subject, synchronized

with a spot on a computer screen. Electrons scattered from the subject are detected and can create a current, the strength of which makes the spot on the computer brighter or darker. This current can create a photograph-like image with an exceptional depth of field. Magnifications of several thousands are possible to achieve. A JEOL-5600 scanning electron microscope, shown in Figure 3-7, capable of resolution of up to 50 nm at magnifications of up to 100,000 times, was used in this study. The manual stage of this SEM unit can accommodate four 1 cm diameter samples or one sample with up to 3.2 cm diameter. This SEM was used for the fractographic evaluation of the failure surfaces of the tested specimens.

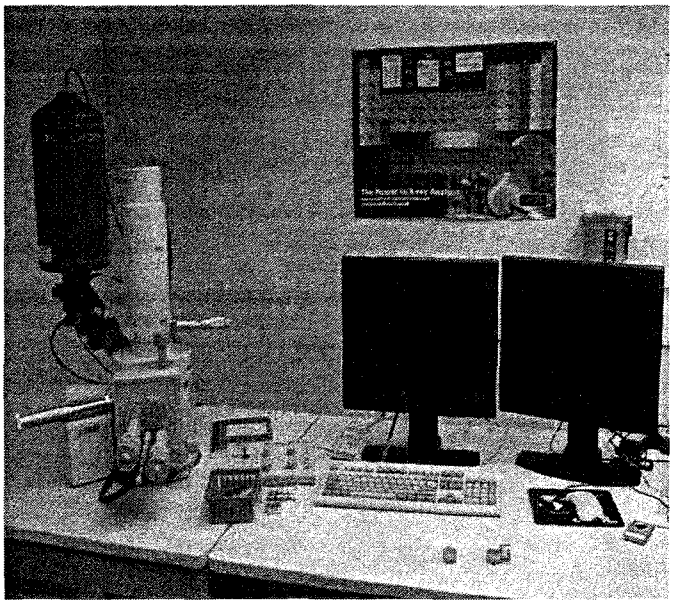

Figure 3-7 Scanning Electron Microscope

3.7 Transmission Electron Microscopy

TEM studies were conducted to characterize defects including dislocations in the tested tensile specimens using a Tecnai G^2 F30 S-TWIN Transmission Electron Microscope (Figure 3-8). This equipment operates with as high as 300kV acceleration voltage that allows a point-to-point resolution of 0.2 nanometer. Magnifications up to 1,000,000 times can be achieved with this TEM. This system is fully loaded including HAADF (high angle annular dark field) detector, EDX (X-ray energy disperse spectrometry), and GIF (Gatan Image Filter). Multiple samples were prepared from each tested specimen condition to obtain TEM micrographs. The sample preparation technique is described in details in the next subsection.

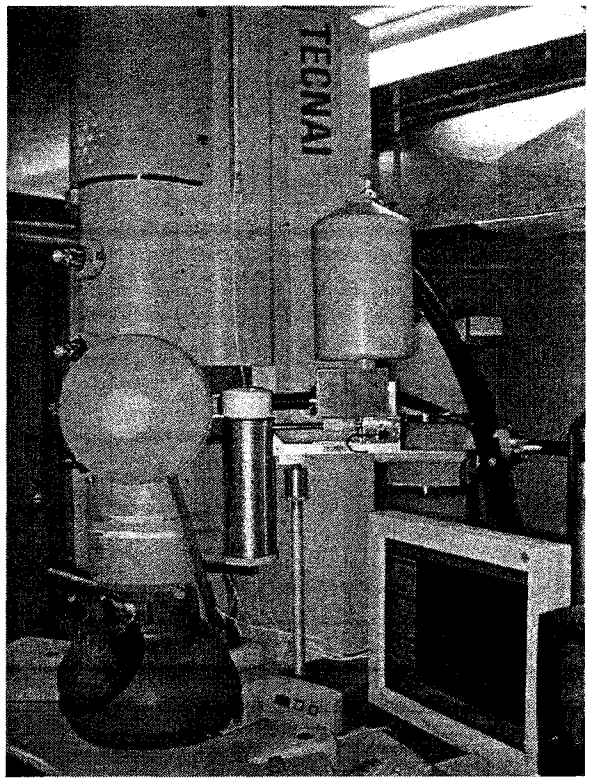

Figure 3-8 Transmission Electron Microscope

3.7.1 TEM Sample Preparation

Sample preparation for the TEM study involves a state-of-art technique. To ensure electron transparency of the sample by the TEM method, the specimen thickness was maintained between 50-100 nanometers. This was achieved through a series of operations, as described below. [41-43]

- Initially, multiple circular disc-shaped samples were cut from the gage length of the failed tensile specimens up to a thickness of 500–700μm, using a precision cutter in the Materials Performance Laboratory (MPL).
- Samples were then mechanically ground (Figure 3-9) to about 100–150 μm using a grinder in the TEM Sample Preparation Laboratory. This process involved two steps; rough-grinding and fine-polishing. Specimen thickness was monitored periodically during this process.
- The samples were then punched into 3mm diameter discs, using a disc puncher (Figure 3-10).
- Finally, electro-polishing was done to achieve the desired specimen thickness. A twin-jet TenuPol-5 electro polisher (Figure 3-11) was used for this purpose. This process involved removal of material from the sample surface as well as surface finish prior to TEM observation. The thinnest area was obtained around the perforation area. The composition of the electrolyte used for the process was 5% perchloric acid ($HClO_4$) in methanol (CH_3OH) with an applied potential of 50V, a pump flow rate of 12 and a temperature of -3°C. [44] Care was taken to control the flow of electrolyte to prevent the formation of anodic film that could cause etching of the specimen rather than polishing. [43, 45]

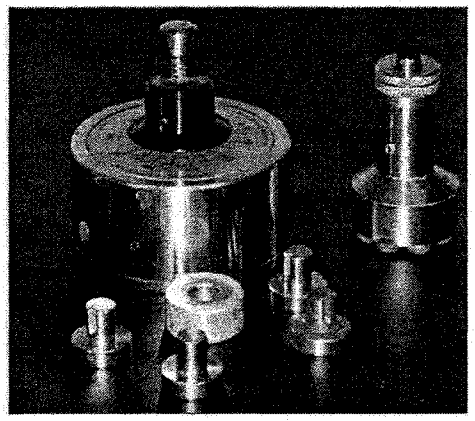

Figure 3-9 Grinding Accessories

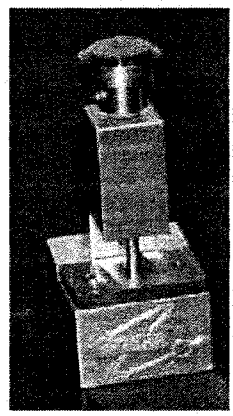

Figure 3-10 Disc Puncher

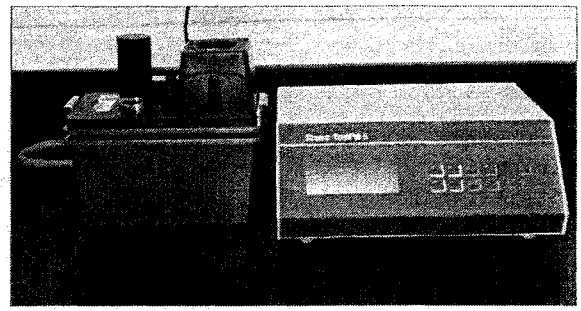

Figure 3-11 TenuPol-5 Electro-polisher

3.7.2 Dislocation Density Calculation

Dislocation density (ρ) was computed from the TEM micrographs of the tested tensile specimens to evaluate the DSA effect at four different temperatures at a strain rate of 5×10^{-4} sec^{-1}. The magnitude of ρ was determined by the line intersection method based on the superimposition of a grid of horizontal and vertical test lines on the TEM micrographs containing dislocations, as shown in Figure 3-12. [43, 46-48] The ρ value was calculated using Equation 3-23. [48]

$$\rho = \frac{1}{t}\left(\frac{\sum n_v}{\sum L_v} + \frac{\sum n_h}{\sum L_h}\right) \qquad \text{Equation 3-23}$$

Where, $\sum n_v$ = Number of intersections of vertical test lines with dislocations

$\sum n_h$ = Number of intersections of horizontal test lines with dislocations

$\sum L_v$ = Total length of vertical test lines (meters)

$\sum L_h$ = Total length of horizontal test lines (meters), and

t = Average thickness of the TEM sample

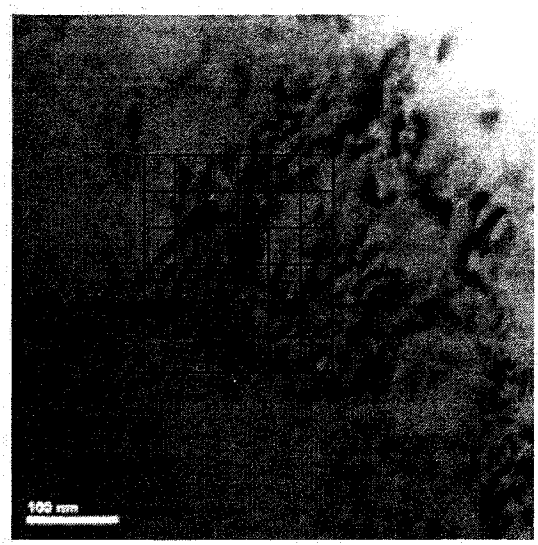

Figure 3-12 Dislocation Density Calculation by Line Intersection Method

The average thickness (t) of the sample was measured using electron energy loss spectroscopy (EELS) technique available in the TEM. EELS was used to measure the thickness of the samples at different locations using Equation 3-24. [49]

$$t = \lambda \ln(I_t / I_o)$$ Equation 3-24

Where, λ = mean free path (calculated using an online software [56])

I_t = total intensity reaching the spectrometer

I_o = zero-loss intensity reaching the spectrometer

An example of the local thickness calculation using EELS is illustrated in Figure 3-13, showing thickness calculations were at six different locations of a tested specimen.

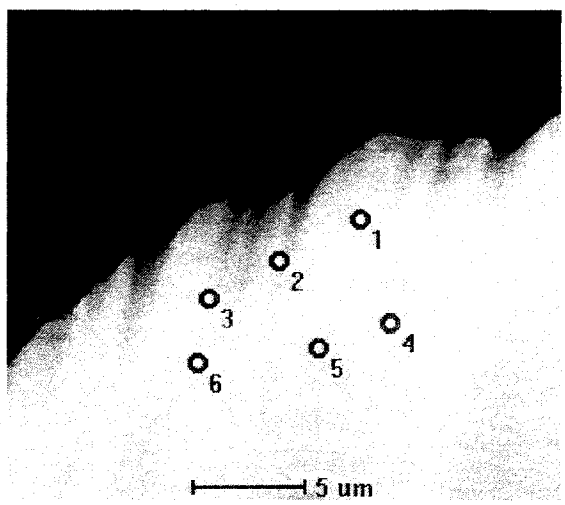

Figure 3-13 EELS Measurement to Compute Average Thickness

3.8 X-Ray Diffraction

XRD was done to characterize the brittle phases [52-55], if any, in the tensile specimens tested at 700 and 800°C. A Panalytical X'PERT Pro X-ray Diffraction Spectrometer (Figure 3-14) with Copper (Cu) K_α radiation was used for this purpose. Measurements

were carried out between angles (2θ) of 6 and 120°, with a step size of 0.017°. The d-spacings were calculated from the intensity (in terms of number of counts) vs. 2θ plots, according to the Equation 3-25. [57] The identification of the formed phases was done by comparing the d-spacing values with those from the available standards. [50, 51]

$$n\lambda = 2d\sin\theta \quad \text{(Bragg's Law)} \qquad \text{Equation 3-25}$$

Where, λ = the wave length of x-rays

d = the spacing between the planes in the atomic lattice

θ = is the angle between the incident ray and the scattering planes

n = an integer (1, in this study)

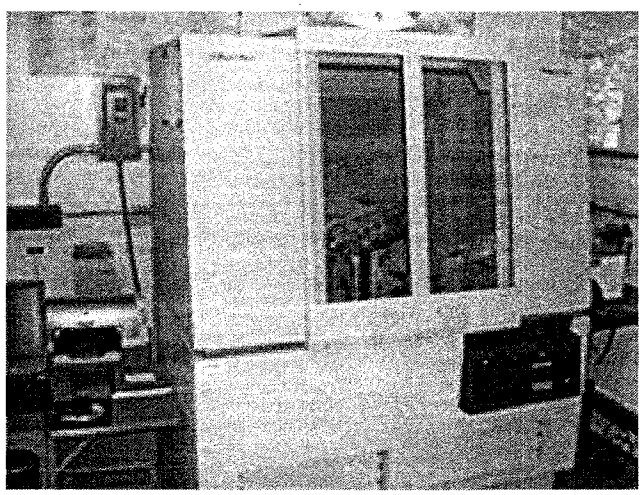

Figure 3-14 X-ray Diffraction Spectrometer

CHAPTER 4

RESULTS

The results of tensile testing of Alloy C-276 at different temperatures and strain rates using smooth cylindrical specimens are presented in this chapter. As indicated in a previous chapter, this alloy exhibited the phenomenon of dynamic strain ageing (DSA), showing reduced failure strain within a critical temperature regime. Since DSA is known to be influenced by both the temperature and strain rate ($\dot{\varepsilon}$), the characterization of DSA of Alloy C-276 has been performed as functions of both mechanical factors. The synergistic effect of applied stress and a potent aqueous environment on the cracking susceptibility of this alloy has been explored in this study through utilization of fracture-mechanics-based pre-cracked double-cantilever-beam (DCB) specimens for two test durations. The cracking susceptibility of this alloy in the presence of an identical aqueous environment has also been evaluated using self-loaded C-ring and U-bend specimens. The corrosion rate based on weight-loss in this environment was determined using rectangular coupons. The characterization of DSA by analyzing defects (dislocations) has been performed by using micrographs obtained from the transmission electron microscopic (TEM) study. The morphology of failures of the tested specimens and the metallurgical microstructures were evaluated by scanning electron microscopy (SEM) and optical microscopy, respectively. Identification of brittle phases, if any, in the specimens tested at elevated temperatures was done by x-ray diffraction (XRD). Efforts

were also made to determine the fracture toughness of compact-tension (CT) specimens at ambient temperature. However, very little success was achieved in this test. The comprehensive results based on the overall experimental work involving Alloy C-276 are presented in the following subsections.

4.1 Metallographic Evaluation

An optical micrograph of an etched Alloy C-276 specimen is illustrated in Figure 4-1. An evaluation of this micrograph reveals a classical metallurgical microstructure of a nickel-base material [59], showing large austenitic grains and annealing twins resulting from solution-annealing and subsequent rapid cooling in water.

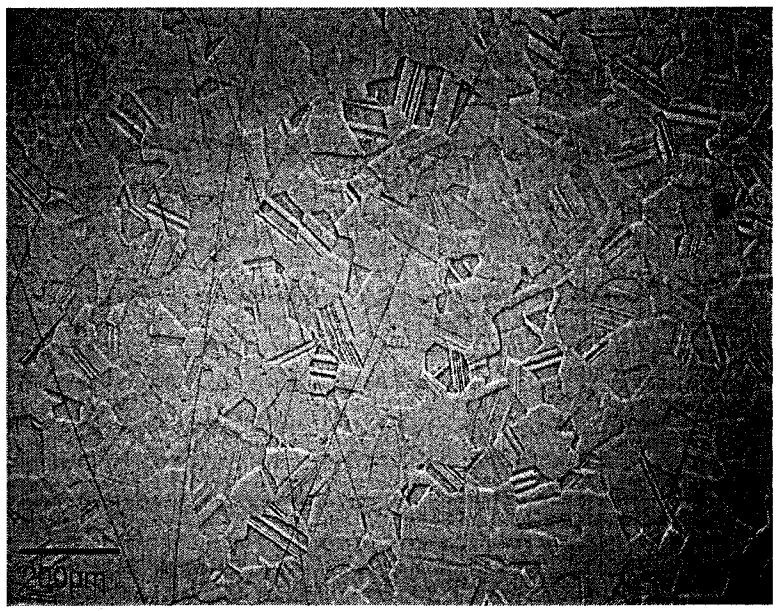

Figure 4-1 Optical Micrograph, Etched (Glyceregia), 50X

4.2 Tensile Properties Evaluations

4.2.1 Stress-Strain Relationships vs. Temperature

The results of tensile testing of Alloy C-276, performed at temperatures ranging from ambient to 1000°C using a strain rate of 5×10^{-4} sec^{-1}, are illustrated in Figure 4-2 in the form of superimposed engineering stress versus strain (s-e) diagrams. An evaluation of these s-e diagrams reveals that the tensile strength of this alloy in terms of the yield strength (YS) and the ultimate tensile strength (UTS) was gradually reduced with increasing temperature. It is however interesting to note that, despite such gradual reduction in tensile strength with increasing temperature, the magnitude of YS of this alloy was relatively higher compared to that of other structural materials currently in use for engineering applications. For some other materials, the tensile strength might be somewhat higher at comparable temperatures. However, the ductility of those alloys is relatively poor compared to that of Alloy C-276. This alloy was also capable of sustaining a high tensile strength at 1000°C. Thus, this alloy should have sufficient structural strength for application in the S-I process, where an operating temperature of 950°C has been proposed to ensure the maximum possible efficiency during the H_2SO_4 decomposition process.

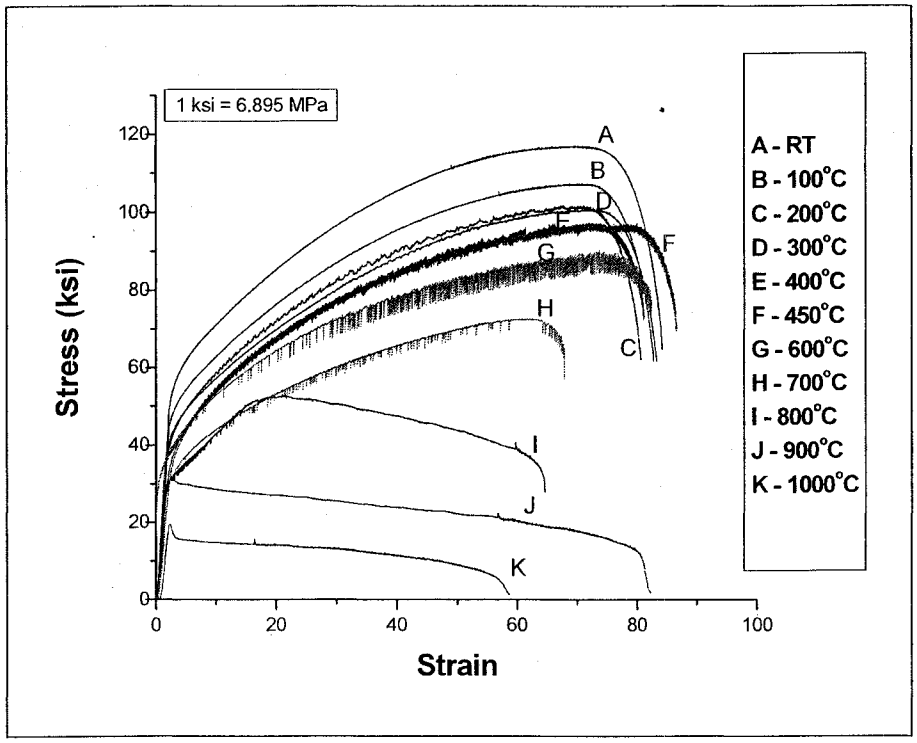

Figure 4-2 S-e Diagrams vs. Temperature

As to the tensile deformation of this alloy at these temperatures, an interesting phenomenon of reduced failure strain (e_f) was observed at temperatures ranging from ambient to 200°C. Beyond this temperature, increased values of e_f were seen up to a temperature of 450°C, above which the magnitude of e_f was drastically reduced up to a temperature of 800°C. This phenomenon of reduced e_f within a susceptible temperature regime (ambient to 200°C) has been cited [4] to be the result of solute diffusion into the metal lattice, causing reduced dislocation mobility in the vicinity of the grain boundaries. Serrations of varying degrees were also noted in the s-e diagrams in the temperature regime of 200-700°C. The occurrence of reduced e_f and development of serrations in the s-e diagrams is a manifestation of a metallurgical phenomenon, commonly known as the dynamic strain ageing (DSA) behavior of engineering metals and alloys.

The average values of different tensile parameters including YS, UTS, percent elongation (%El) and percent reduction in area (%RA), determined from the s-e diagrams and the specimen dimensions before and after testing, are given in Table 4-1. An evaluation of these data reveals that the ductility in terms of %El was gradually reduced up to a temperature of 200°C, followed by its slight enhancement up to a temperature of 400°C. Beyond 400°C, an irregular pattern on the variation of %El with temperature was seen. With respect to %RA, its value was gradually dropped up to a temperature of 400°C, followed by a slight enhancement at 450°C. A similar irregular pattern was also observed with this parameter at higher temperatures. The variations of all four tensile parameters with temperature, shown in Table 4-1, are illustrated in Figures 4-3 through 4-6.

Table 4-1 Average Tensile Properties vs. Temperature

Temperature (°C)	YS, ksi / MPa	UTS, ksi / MPa	%El	%RA
Ambient	51.4 / 354.4	115.2 / 794.3	86.8	78.3
100	44.7 / 308.2	105.0 / 723.9	84.8	76.7
200	39.4 / 271.7	100.7 / 694.3	83.9	75.9
300	37.8 / 260.6	98.9 / 681.9	84.7	72.6
400	33.9 / 233.7	96.0 / 661.9	84.5	72.9
450	32.4 / 223.4	94.7 / 652.9	88.1	76.1
600	30.8 / 212.4	89.2 / 615.0	83.3	67.3
700	30.1 / 207.5	73.7 / 508.2	65.9	52.8
800	28.9 / 199.3	52.0 / 358.5	59.4	48.4
900	27.9 / 192.4	31.7 / 218.6	78.9	61.5
1000	17.8 / 122.7	18.2 / 125.5	55.7	46.5

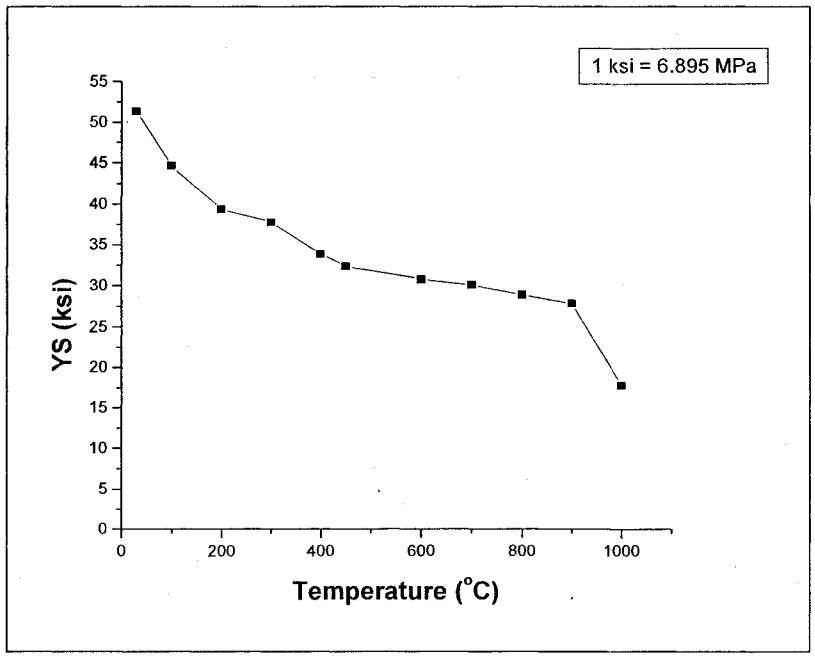

Figure 4-3 YS vs. Temperature

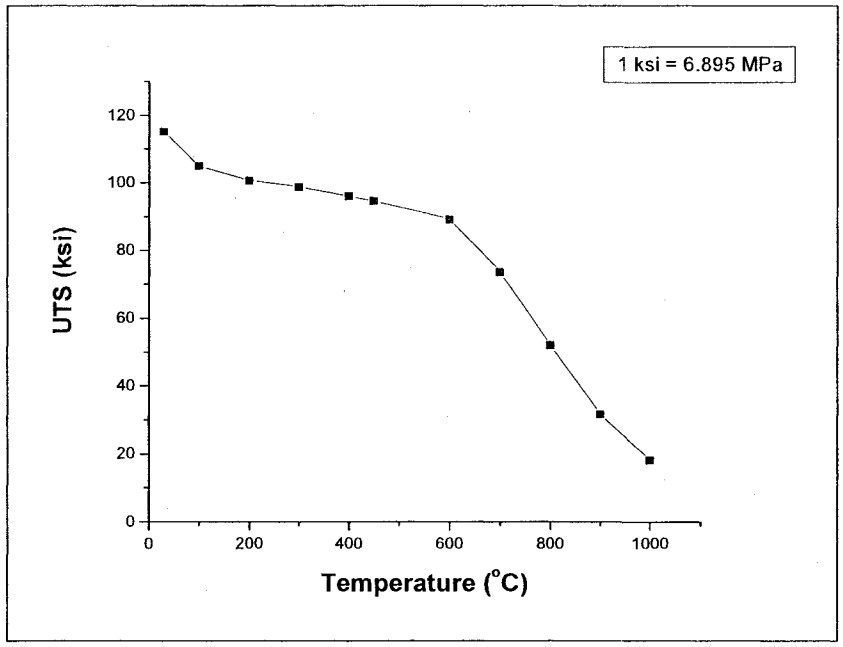

Figure 4-4 UTS vs. Temperature

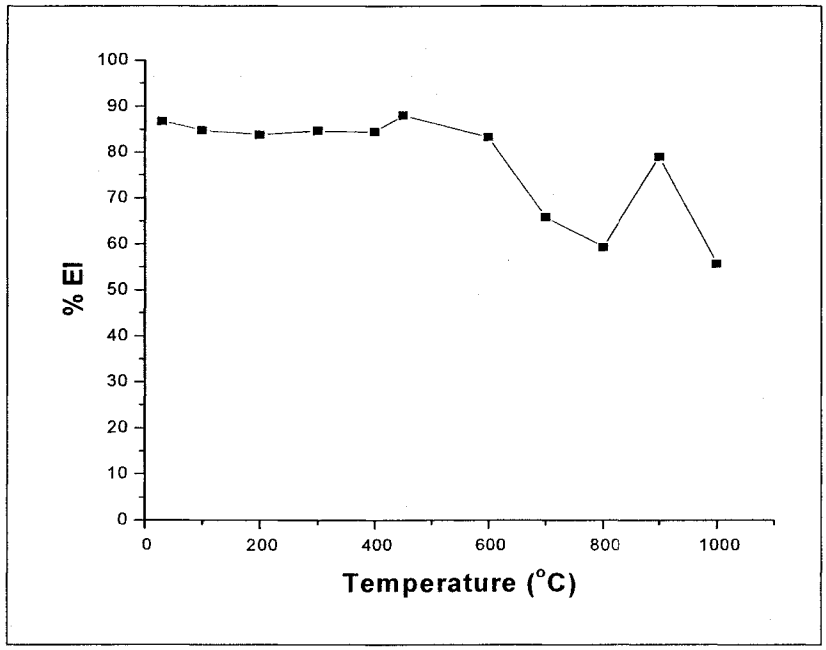

Figure 4-5 %El vs. Temperature

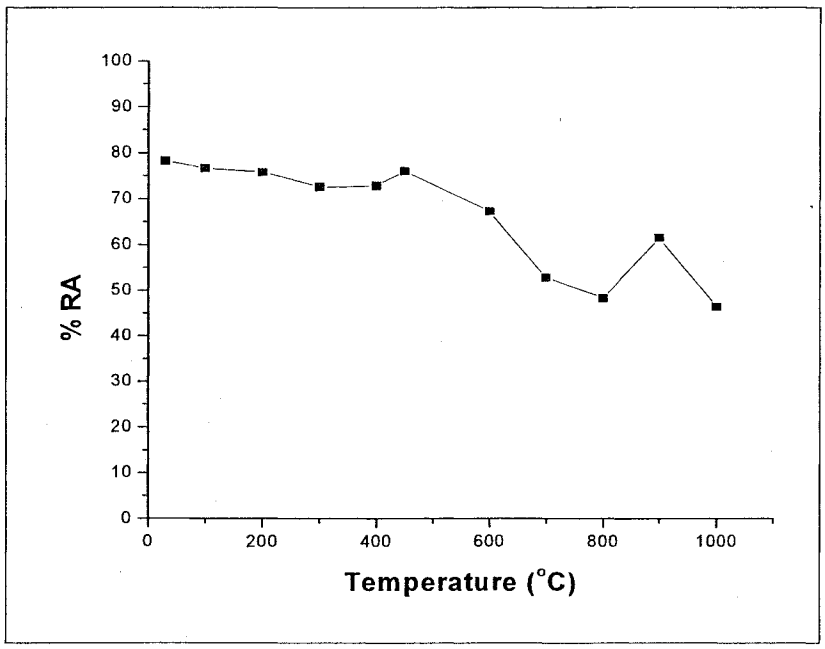

Figure 4-6 %RA vs. Temperature

4.2.2 Characterization of Dislocations by TEM

As indicated earlier in a previous section, the reduced e_f in the temperature regime of ambient to 200°C could be the result of enhanced dislocation concentration near the grain boundaries, thus leading to reduced plastic deformation in terms of e_f. It is also interesting to note that the ductility in terms of %RA was gradually reduced up to a temperature of 300°C. Therefore, efforts were made in this investigation to estimate the dislocation concentration in specimens tested in the temperature regime of ambient to 300°C through utilization of transmission electron microscopy (TEM). Since the magnitudes of %El and %RA were appreciably enhanced at 450°C, TEM was also used on the specimen tested at this temperature to determine the dislocation density (ρ).

For TEM evaluation, thin film specimens of Alloy C-276 were prepared to develop micrographs of specimens tested in the DSA susceptible temperature regime and 450°C. TEM micrographs were obtained at different locations of each specimen at comparable magnifications, and the magnitude of an average value of ρ was determined using these micrographs. The average value of ρ was then plotted as a function of the testing temperature. The resultant TEM micrographs developed at each tested temperature are illustrated in Figure 4-7 (a-e). A qualitative evaluation of these micrographs clearly reveals that the extent of dislocation clusters was gradually increased with increasing temperature up to 300°C. Beyond this temperature, the concentrations of dislocations were significantly reduced, as illustrated in Figure 4-7 (e).

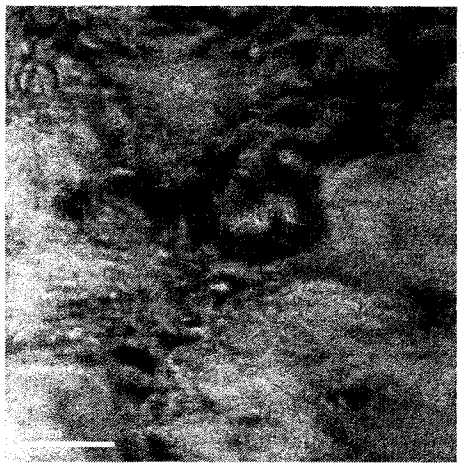

(a) Room Temperature

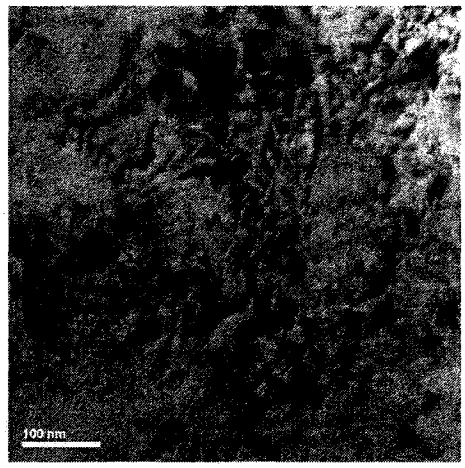

(b) 100°C

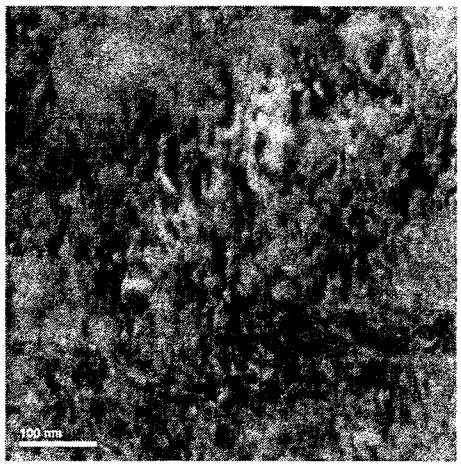

(c) 200°C

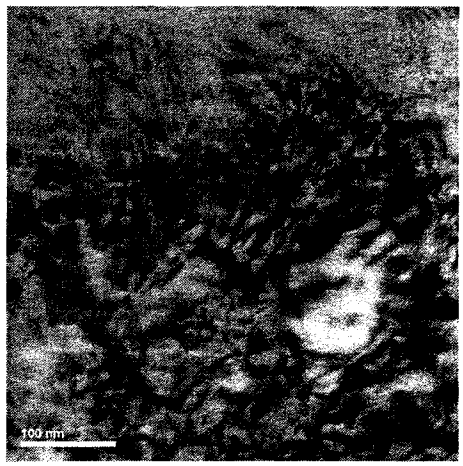

(d) 300°C

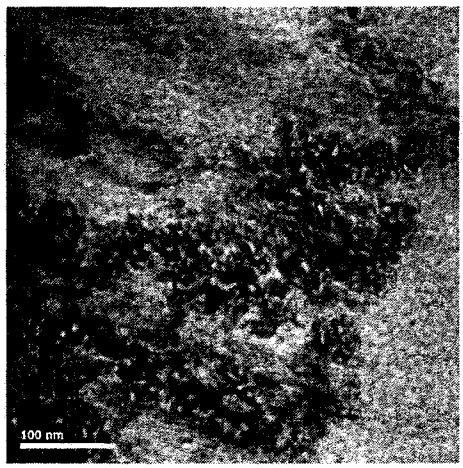

(e) 450°C

Figure 4-7 TEM Micrographs vs. Temperature, 77000X

The magnitude of ρ was determined from the TEM micrographs using the line intersection method, as described in an earlier section of this thesis. An average value of ρ was determined based on at least three TEM micrographs obtained on the same specimen tested at a specific temperature. The average value of ρ, calculated by this method, at each temperature, is given in Table 4-2. A comparative analysis of these data clearly reveals that the concentration of dislocation was relatively higher at 200 and 300°C, which can also be verified by the physical appearance of the TEM micrographs, illustrated in Figure 4-7. The variation of ρ with temperature is illustrated in Figure 4-8. It is of interest to note that the magnitude of ρ at 450°C was somewhat lower compared to those observed in the temperature regime of 100-300°C. The reduced value of ρ at 450°C is primarily due to the enhanced dislocation mobility at higher temperature, which is also substantiated by thinner clusters of dislocations, as shown in Figure 4-7 (e).

Table 4-2 Average Dislocation Density vs. Temperature

Temperature (°C)	Dislocation Density (ρ), no./m^2
Ambient Temperature	1.97×10^{14}
100	3.48×10^{15}
200	4.10×10^{15}
300	4.51×10^{15}
450	1.73×10^{15}

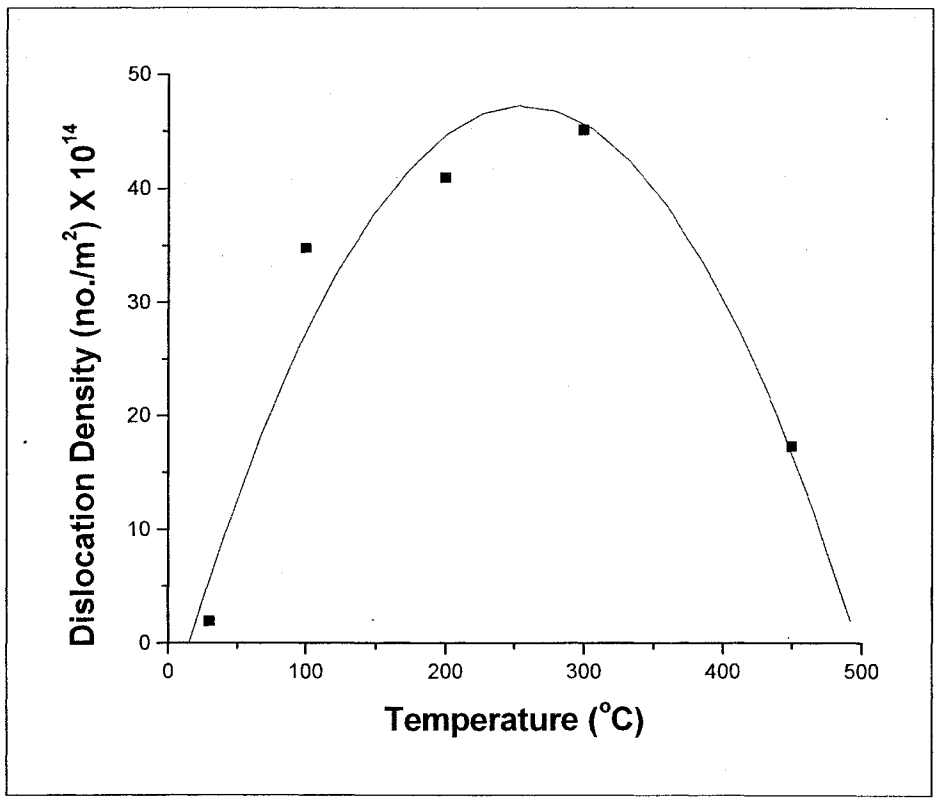

Figure 4-8 Dislocation Density vs. Temperature

4.2.3 Temperature and Strain Rate Effects on DSA

4.2.3.1 Determination of Q

As indicated earlier, the phenomenon of DSA is influenced by both the temperature and $\dot{\varepsilon}$. Therefore, substantial efforts have been made in this investigation to develop a basic understanding on the DSA behavior of Alloy C-276 that exhibited reduced e_f values and formation of serrations within a certain temperature regime. The susceptible temperature regime at which reduced e_f was observed was initially determined by using a $\dot{\varepsilon}$ of 5×10^{-4} sec^{-1}. Thus, in order to study the effect of $\dot{\varepsilon}$ on the DSA behavior of this alloy, strain rates above and below this value were applied at temperatures of 200, 300, 400 and 450°C. The corresponding strain rates were 10^{-3} and 10^{-4} sec^{-1}, respectively.

It is well-known that the plastic deformation of engineering materials is influenced by both temperature and $\dot{\varepsilon}$. The extent of plastic deformation as functions of these two parameters can be estimated by evaluating two important metallurgical parameters, namely the strain hardening exponent (n) and the activation energy (Q). The fundamentals on plastic deformation in terms of n and Q have been extensively explained in the previous chapter of this thesis. In addition, the role of critical plastic strain (ε_c) on the onset of the formation of serrations has been discussed to better understand the concept of DSA as functions of both temperature and $\dot{\varepsilon}$. The variation of ε_c with temperature at different strain rates is illustrated in Figure 4-9. A critical analysis of the data clearly exhibits a gradual drop in ε_c with increasing temperature when tested up to a temperature of 450°C, irrespective of the $\dot{\varepsilon}$. Further, the magnitude of ε_c was higher at

faster strain rates at a constant temperature. A consistent pattern on the variation of ε_c with temperature at different strain rates has been reported in the open literature. [8]

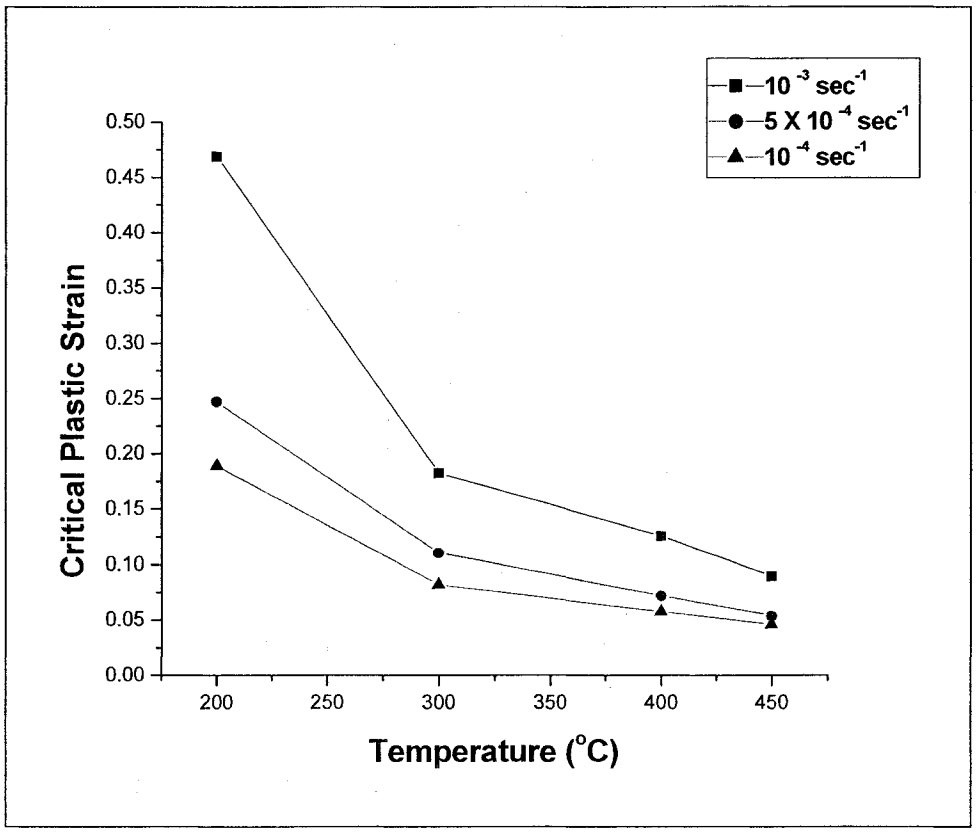

Figure 4-9 Critical Plastic Strain vs. Temperature

As discussed earlier in the previous chapter, two different methods have been used in this investigation to determine Q. The first method of Q calculation is based on the slope $\left(\frac{Q}{R(m+\beta)}\right)$ derived from the plot of ln ε_c vs. $\frac{1}{T}$, as shown in Figure 4-10. The magnitude of $(m+\beta)$ can be determined using the plot of ln $\dot{\varepsilon}$ as a function of $\ln\varepsilon_c$, according to the Equation 3-9. $(m+\beta)$ in this case is simply the slope of the straight line,

as illustrated in Figure 4-11. Duplicate testing was performed at 200, 300, 400 and 450°C at each $\dot{\varepsilon}$. The magnitude of $(m+\beta)$ determined by this method and the average value of Q based on duplicate testing, are given in Table 4-3.

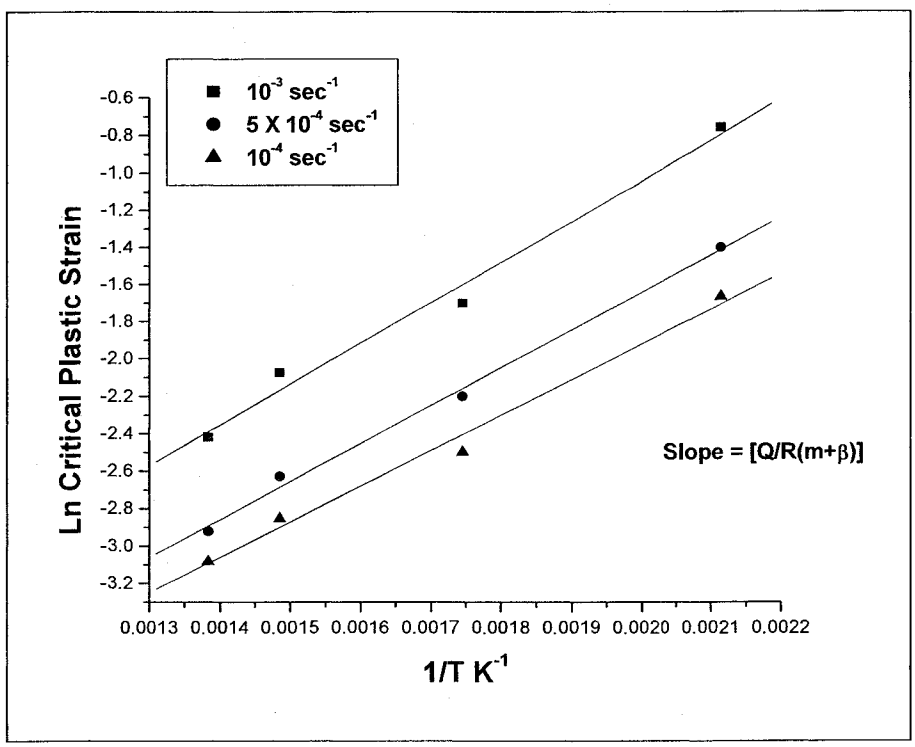

Figure 4-10 ln ε_c vs. $\frac{1}{T}$

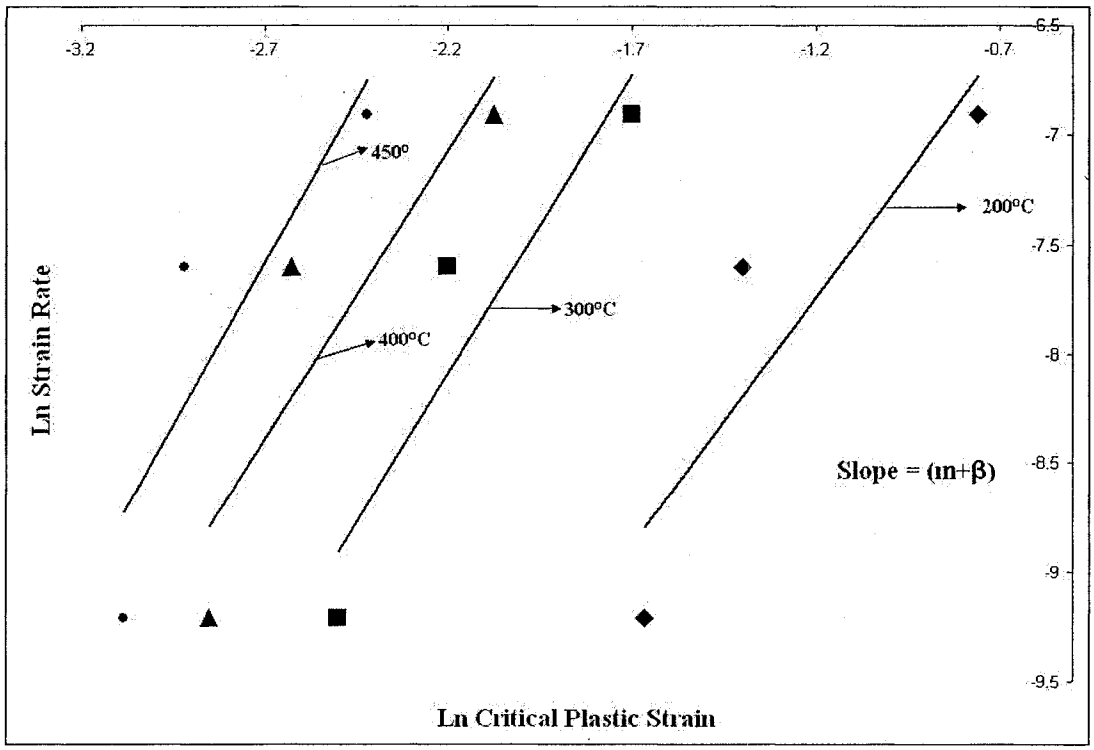

Figure 4-11 $\ln \dot{\varepsilon}$ vs. $\ln \varepsilon_c$

Table 4-3 Calculation of Q based on $(m+\beta)$ Values

Temperature (°C)	Test No.	$(m+\beta)$			Q (KJ/mole)	Average Q (KJ/mole)
		$\dot{\varepsilon}$ (sec^{-1})				
		10^{-3}	5×10^{-4}	10^{-4}		
200	1	2.3	2.3	2.3	38.4	48.3
	2	2.3	2.3	2.3	45.4	
300	1	2.7	2.7	2.7	46.2	
	2	2.8	2.8	2.8	55.8	
400	1	2.6	2.6	2.6	44.7	
	2	2.5	2.5	2.5	49.7	
450	1	2.9	2.9	2.9	50.4	
	2	2.8	2.8	2.8	55.8	

The second method of Q calculation, based on the McCormick's strain ageing model, was accomplished by plotting $\ln\left[\frac{\varepsilon_c^{(m+\beta)}}{T}\right]$ as a function of $\frac{1}{T}$, in which $\frac{Q}{k}$ represented the slope of the straight line. A graphical representation of this plot is illustrated in Figure 4-12. The magnitude of $(m+\beta)$ was still the same as obtained by the first method. Q was calculated from the slope that contained a k term, which represents the Boltzman constant. The individual values of Q at each $\dot{\varepsilon}$ for duplicate testing are given in Table 4-4, from which the magnitude of the average Q based on all three strain rates was

calculated. Thus, the magnitudes of the average Q values based on two different methods of calculation were approximately 48 and 62 KJ/mole, as shown in Tables 4-3 and 4-4, respectively. Variations in the Q values by different magnitudes, as seen in this investigation, have also been reported by other investigators involving different types of austenitic materials having different chemical compositions. [8, 9] Thus, it can be concluded that the activation energy of Alloy C-276 in the tested temperature regime may range between 48 and 62 KJ/mole, giving an average activation energy of 55 KJ/mole.

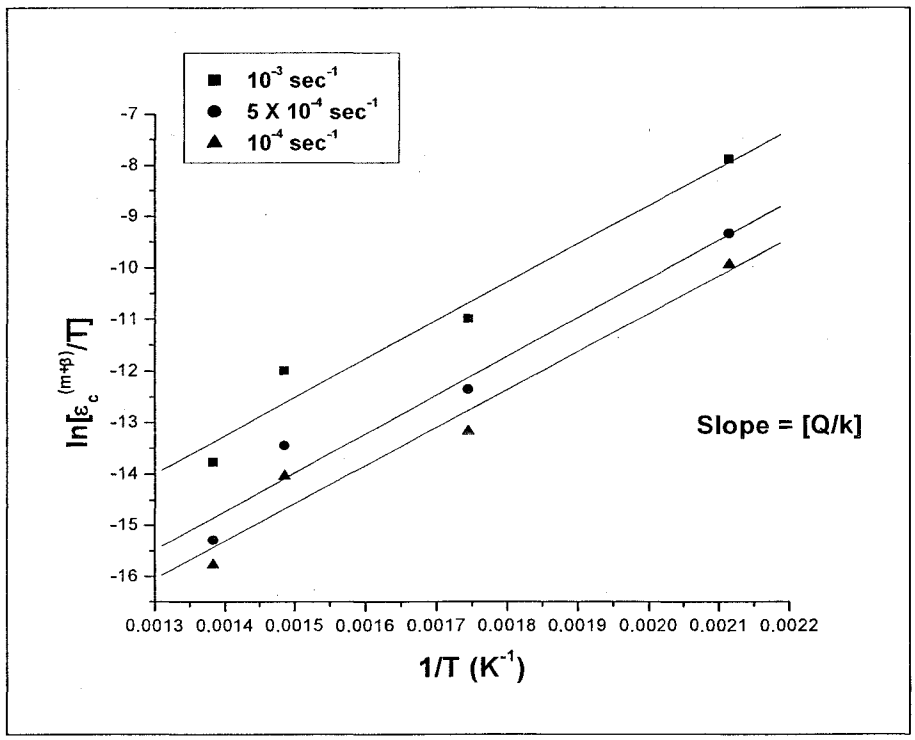

Figure 4-12 Plot of $\ln\left[\frac{\varepsilon_c^{(m+\beta)}}{T}\right]$ vs. $\frac{1}{T}$

Table 4-4 Q value, based on the Second Method

$\dot{\varepsilon}$ (sec^{-1})	Test No.	Q (KJ/mole)	Average Q (KJ/mole)
10^{-3}	1	61.8	62.3
	2	62.3	
5×10^{-4}	1	62.5	
	2	63.8	
10^{-4}	1	61.2	
	2	62.1	

4.2.3.2 Determination of n

As indicated earlier in the previous chapter, the determination of the strain hardening exponent (n) is conventionally based on the log-log plot of Equation 3-12. Since a linear relationship could not be observed using the Hollomon relationship, a non-linear relationship based on the plots of $\log\sigma$ vs. $\log\varepsilon$, proposed by Ludwigson, has been used in this investigation. Based on this rationalization, the magnitude of n was estimated from the best linear part of the resultant non-linear shape of this plot. The average n value based on triplicate testing at a $\dot{\varepsilon}$ of 5×10^{-4} sec^{-1} within a temperature regime of room temperature to 800°C are given in Table 4-5. An evaluation of these data reveals that the magnitude of n varied between 0.67 and 0.73 at temperatures up to 700°C. However, a significant reduction in the n value was noted at a temperature of 800°C, suggesting

reduced work-hardening of this alloy resulting from enhanced plastic flow at this elevated temperature.

Table 4-5 Strain Hardening Exponent (n) vs. Temperature

Temperature (°C)	$\dot{\varepsilon}$ (sec^{-1})	Average n Value
Room Temperature	5×10^{-4}	0.68
100		0.69
200		0.73
300		0.68
400		0.68
450		0.70
600		0.70
700		0.67
800		0.51

Consistent with the previous approach of calculating Q at temperatures of 200, 300, 400 and 450°C under three strain rates (10^{-3}, 5×10^{-4} and 10^{-4} sec^{-1}), a similar effort was made to calculate n as a function of these three strain rates at all four temperatures. The resultant values of n, based on duplicate testing as functions of $\dot{\varepsilon}$ and temperature are shown in Table 4-6. Once again, the magnitude of n ranged between 0.68 and 0.75, which are very similar to the range in n values obtained at temperatures up to 700°C, as shown in Table 4-5.

Table 4-6 Comparison of n vs. Temperature at Different Strain Rates

Strain Rate (sec^{-1})	Average n Value			
	Temperature (°C)			
	200	300	400	450
10^{-3}	0.75	0.72	0.71	0.73
5×10^{-4}	0.73	0.68	0.68	0.70
10^{-4}	0.74	0.75	0.73	0.71

4.3 Determination of Fracture Toughness

Even though significant efforts were made to determine the plane strain fracture toughness (K_{IC}) of Alloy C-276 using conventional linear-elastic-fracture-mechanics (LEFM) concept, a limited success was met with this testing. The hardware (CT grips) in the Instron testing machine was malfunctioning immediately after the first test. Thus, duplicate testing could not be performed to determine K_{IC}. Nevertheless, the resultant plot (Figure 4-13) in the first test was very similar to the conventional load vs. displacement curve cited in the ASTM Standard E 399-1990. [16] A conditional stress intensity factor (K_Q) of 33.7 $MPa\sqrt{m}$ was achieved in this testing. Since K_{IC} value of Alloy C-276 at room temperature is not yet available from the open literature, it is suggested that additional efforts be made in the near future to verify this K_Q value.

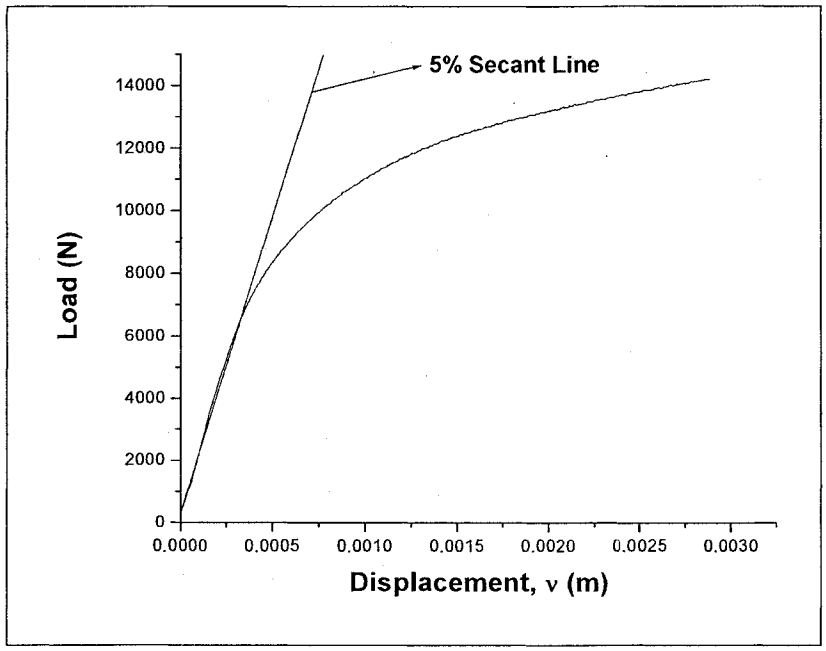

Figure 4-13 Load vs. Displacement

4.4 DCB Test Results

The magnitudes of the stress intensity factor (K) before and after exposure of the pre-cracked wedge-loaded DCB specimens in the acidic solution are given in Table 4-7. The final crack length of the DCB specimens was determined from the SEM micrographs of specimens tested at different initial stress intensity factor (K_I) values during exposure for 15 and 30 days, respectively. The SEM micrographs of Alloy C-276 exposed to the acidic solution for 30 days under three different K_I values are illustrated in Figure 4-14 (a-c). These micrographs clearly identify three types of microstructures corresponding to cyclic loading during pre-cracking, crack extension due to stress-corrosion-cracking (SCC) and ductile failure due to fast fracture. The magnitude of the average crack length upon completion of 30-day testing was determined from these micrographs using an average width of the SCC at multiple locations within the cracking band. An examination

of these micrographs reveals striations characterizing brittle failure under cyclic loading, cleavage failure due to SCC and dimpled microstructure indicating ductile failure resulting from fast fracture. It should be noted that the DCB specimens did not exhibit any crack extension when tested for 15 days under K_1 values of 30.7 and 37.2 $MPa\sqrt{m}$. These results indicate that additional testing should be performed to evaluate cracking under similar levels of K_1 values for longer durations. The final load sustained by the DCB specimens upon completion of testing was determined from the linear portion of the load vs. displacement curve. By knowing the final load and crack length, the final stress intensity factor (K_{1SCC}) was computed using Equation 3-20.

Table 4-7 Results of DCB Testing

Specimen No.	T	P_i	P_f	ΔP	a_i	a_f	Δa	K_1	K_{1SCC}	ΔK
1	15	1925	1408	517	33.2	33.2	None	30.5	22.3	8.2
2		2216	1515	701	33.7	33.7	None	37.0	25.3	11.7
3		2496	1690	806	33.7	33.96	0.26	41.6	28.3	13.3
4	30	1966	1342	624	33.7	34.09	0.39	32.4	22.3	10.1
5		2310	1557	753	34.2	34.77	0.57	38.5	26.3	12.2
6		2675	1886	789	34.2	35.01	0.81	44.5	31.9	12.6

T = Test Duration (days)

P_i = Initial load (N)

P_f = Final load (N)

ΔP = Reduction in Load (N)

a_i = Initial crack length (mm)

a_f = Final crack length (mm)

Δa = Crack extension (mm)

K_1 = Initial stress intensity factor ($MPa\sqrt{m}$)

K_{1SCC} = Final stress intensity factor after exposure ($MPa\sqrt{m}$)

ΔK = Reduction in stress intensity factor after exposure ($MPa\sqrt{m}$)

$1\ MPa\sqrt{m} = 1.1\ ksi\sqrt{inch.}$

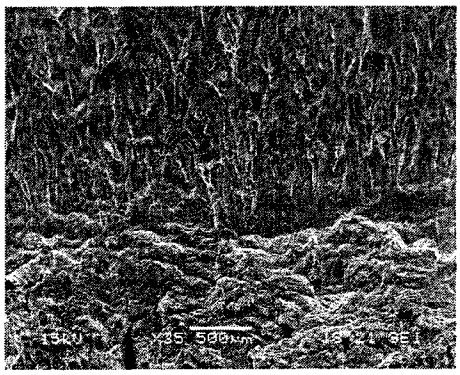

(a) 30 days, Lowest K_1

(b) 30 Days, Intermediate K_1

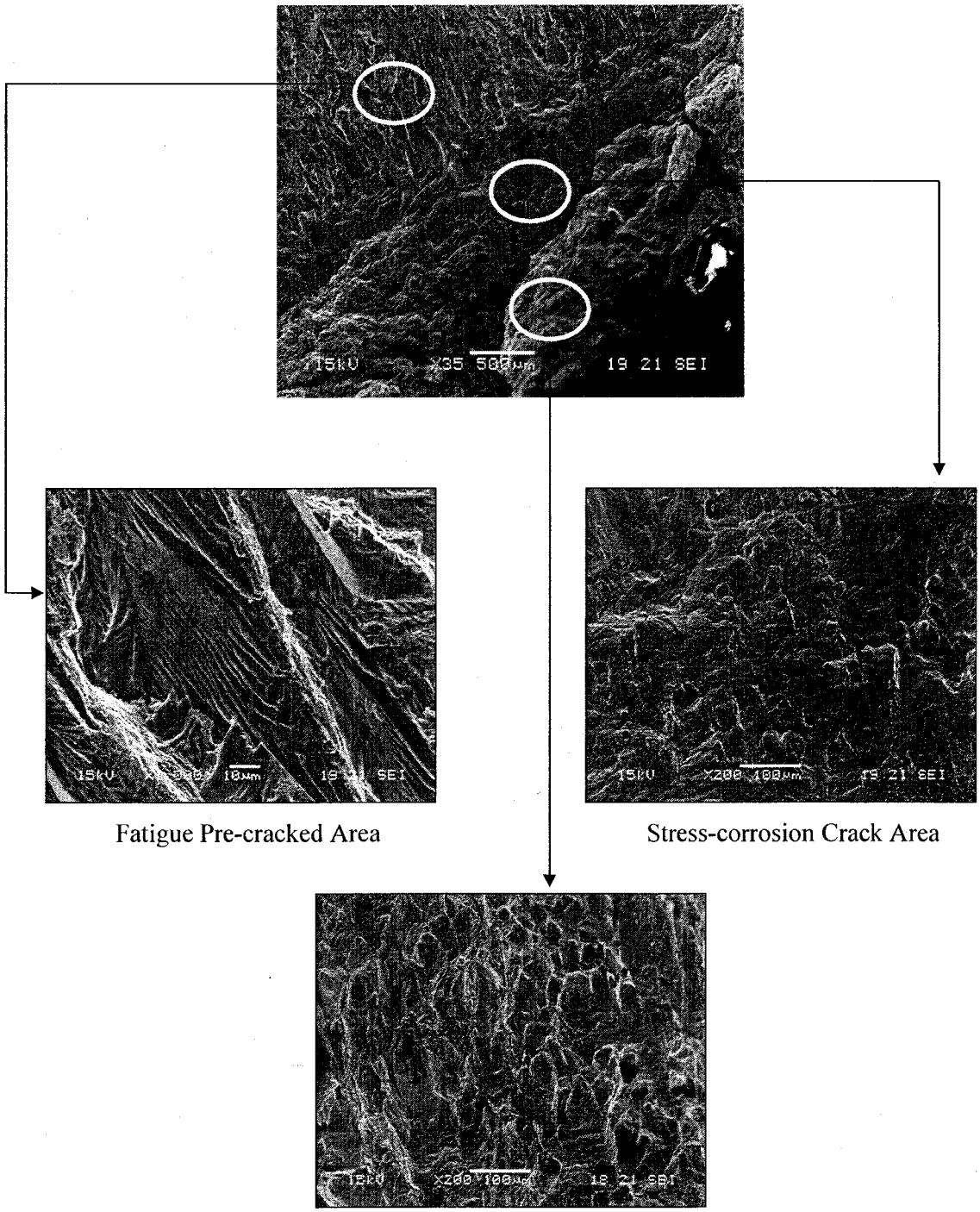

Fatigue Pre-cracked Area

Stress-corrosion Crack Area

Fast Fracture

(c) 30 Days, Highest K_I

Figure 4-14 SEM Micrographs, DCB Specimens

4.5 Corrosion Testing with C-ring, U-bend and Coupons

The results of a limited number of SCC testing involving duplicate C-ring and U-bend specimens of Alloy C-276 indicate that neither type of specimen exhibited any cracking tendency on the convex surface of these specimens. Even though SCC testing up to a temperature of 600°C for longer durations was desired, testing could not be performed at temperature above 150°C for periods ranging between 7 and 56 days. Above 150°C, the autoclave started leaking. The corrosion rate in terms of mpy was also determined using coupons exposed to the 150°C acidic solution for similar durations. A gradual reduction in the average corrosion rate with longer exposure time was observed, as shown in Table 4-8.

Table 4-8 Corrosion Rate vs. Exposure Period

Exposure Period (Days)	Sample No.	Corrosion Rate (mpy)	Average Corrosion Rate (mpy)
7	1	5.30	5.24
	2	5.18	
14	1	4.28	4.29
	2	4.29	
28	1	3.45	3.75
	2	4.05	
56	1	3.11	3.51
	2	3.91	

4.6 Results of SEM and XRD Evaluations

Extensive efforts were made to analyze the extent and morphology of failure of the tensile specimens tested at ambient and elevated temperatures using SEM. An evaluation of the SEM micrographs revealed that the primary fracture surface of the specimens tested at temperatures up to 600°C was characterized predominantly by the presence of dimples, indicating ductile failures. However, intergranular brittle failures were observed in the SEM micrographs for specimens tested at 700 and 800°C. Some of the resultant SEM micrographs are illustrated in Figure 4-15 (a-d).

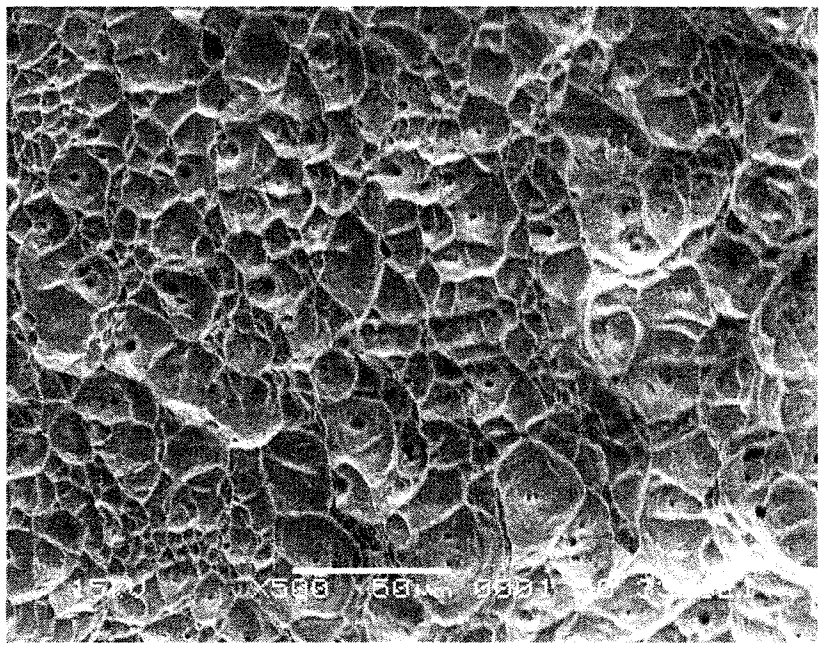

(a) Ambient Temperature

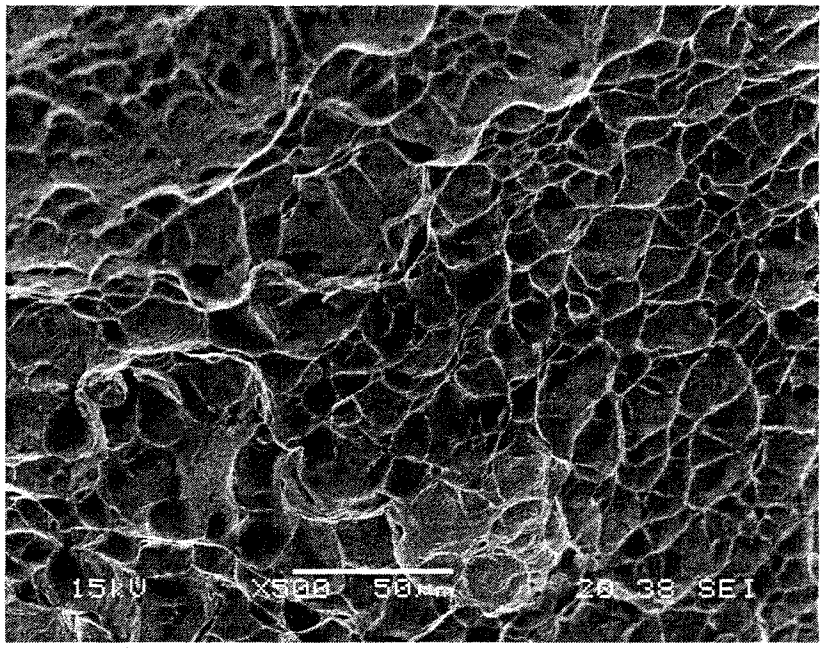

(b) 600°C

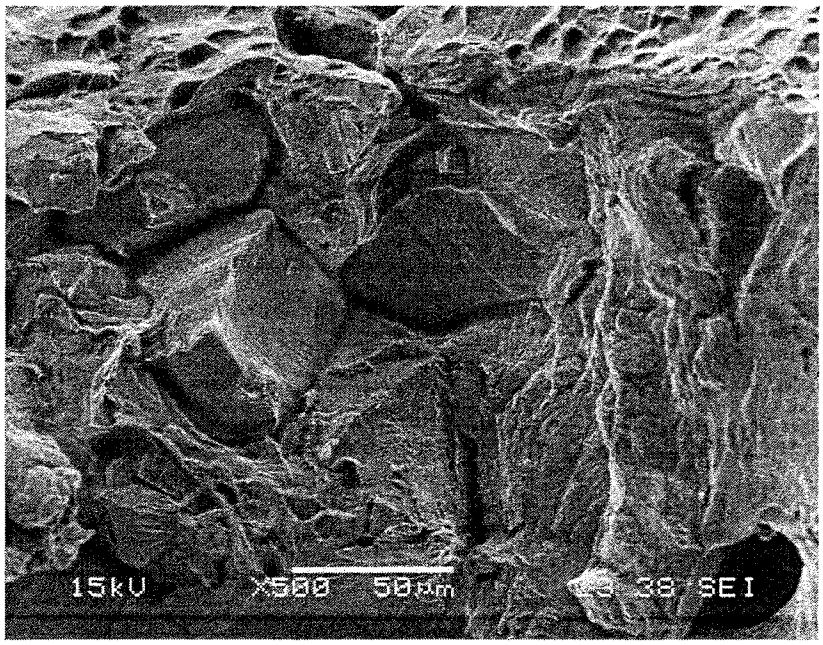

(c) 700°C

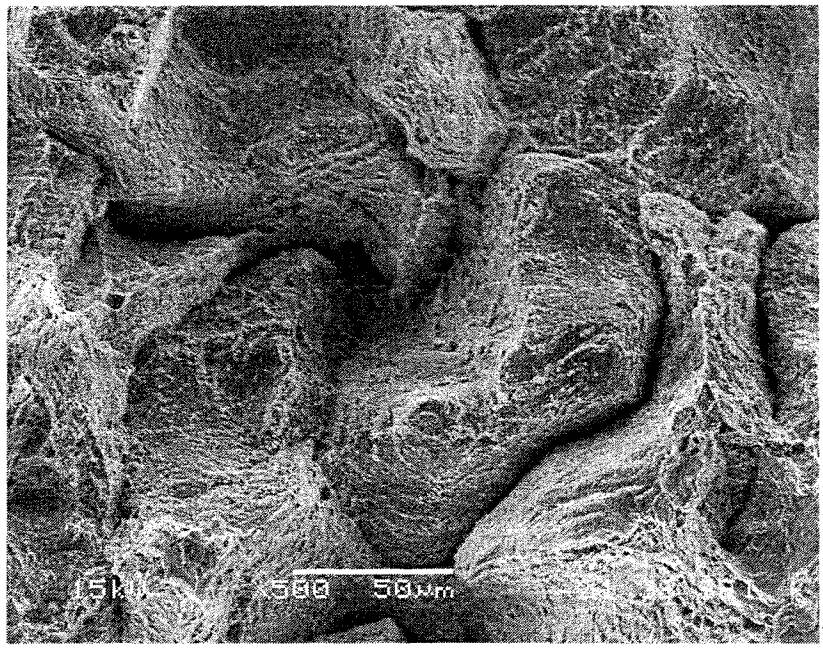

(d) 800°C

Figure 4-15 SEM Micrographs, 500X

Since intergranular brittle failures were seen at 700 and 800°C, XRD was employed to characterize brittle phases, if any, in these specimens. The XRD spectrum, and a comparative analysis of the d-spacing based on the 2θ values corresponding to each peak resulting from the XRD measurements for specimen tested at 800°C are shown in Figure 4-16 and Table 4-9, respectively. An evaluation of the data shown in Table 4-9 indicates that the calculated values of d-spacing of precipitates of $M_{23}C_6$ type. The literature [54] suggests that these precipitates are the carbides of elements including Cr, Mo and Co.

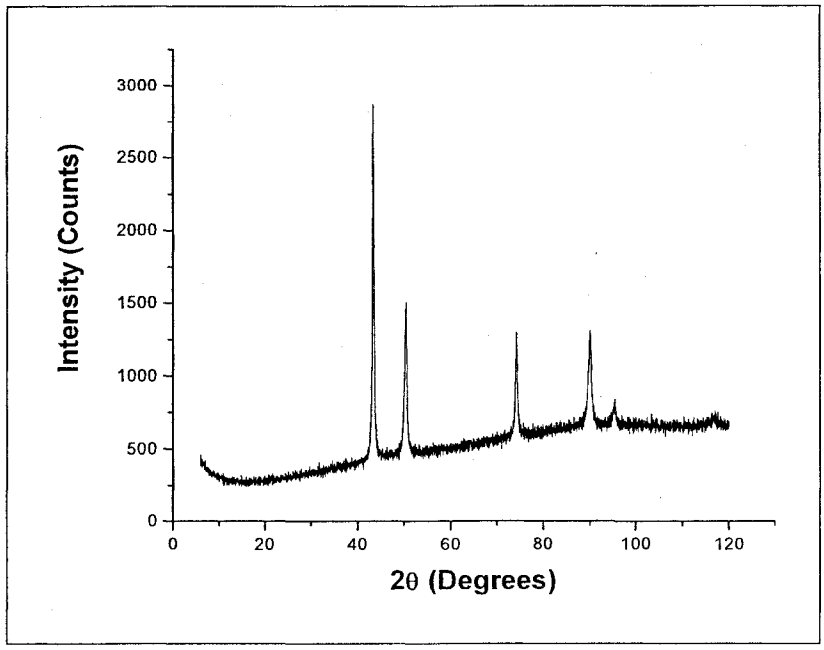

Figure 4-16 Intensity vs. 2θ, 800°C

Table 4-9 XRD Analysis, 800°C

d-spacing (Calculated)	d-spacing of $M_{23}C_6$ (ICDD Standard)
2.085	2.083
1.808	1.810
1.277	1.274
1.089	1.093
1.041	1.041

ICDD: International Centre for Diffraction Data

Chapter 5

DISCUSSION

The results of tensile testing revealed a gradual drop in structural strength in terms of YS and UTS with increasing temperature due to reduced resistance to plastic deformation associated with temperature-induced gradual softening of the test material. However, reduced failure strain (e_f) was observed in the temperature regime of ambient to 200°C, when tested under a strain rate ($\dot{\varepsilon}$) of 5×10^{-4} sec^{-1}. This phenomenon of reduced e_f under tensile loading within a specific temperature regime has been termed as dynamic strain ageing (DSA) of nickel-base superalloys such as Alloy C-276. Literature [4-11] suggests that the occurrence of DSA, showing reduced e_f and serrations in the engineering stress-strain (s-e) diagrams, are often influenced by both the temperature and the $\dot{\varepsilon}$. Therefore, tensile testing involving Alloy C-276 was also performed at two other strain rates (10^{-3} and 10^{-4} sec^{-1}) not only at the susceptible temperature of 200°C but also at temperatures of 300, 400 and 450°C. It is interesting to note that the width of the serrations was enhanced at higher temperatures.

It is well-known that the occurrence of DSA is related to the diffusion of interstitial and/or substitutional solute elements as a function of temperature within a susceptible regime. The plastic deformation of engineering metals and alloys are generally associated

with the formation of lattice defects such as dislocations and voids, and their subsequent movement within the metal lattice. Finally, these dislocations are clustered near the grain boundaries before they can move to the next grains. Some kind of driving forces are needed to activate the movement of these dislocations from one grain to another. Such driving forces include tensile loading at higher temperatures. At relatively lower temperatures, a structural material work hardens, causing reduced e_f. Additionally, the diffusion of solute atoms at relatively higher temperatures tries to block the movement of dislocations by positioning them near the grain boundaries. Such reduction in dislocation mobility through the grain boundaries can result in further reduction in e_f, a phenomenon that was also noted in this investigation, especially in the temperature regime of ambient to 200°C. Beyond 300°C, the dislocations were relatively free to move to the next grains due to higher driving force, thus leading to increased e_f values.

It is obvious from the preceding discussion that the concentration of dislocations can play a significant role in influencing the DSA behavior of an austenitic alloy such as Alloy C-276. Therefore, an extensive effort was made in this investigation to estimate the dislocation density (ρ) based on the TEM micrographs of specimens tested in the temperature regime of ambient to 450°C. The resultant data indicate that the concentration of dislocations in terms of ρ was relatively higher at 200 and 300°C compared to that at 450°C. The relatively lower ρ value at 450°C can be attributed to the enhanced dislocation mobility and plastic flow at this temperature, thus causing reduced concentration of dislocations near the grain boundaries. The calculated values of ρ were consistent with the physical appearance of the TEM micrographs as a function of the testing temperature.

The determination of the activation energy (Q) and the work hardening index (n) is of vital importance to understand the mechanism of DSA as functions of both temperature and $\dot{\varepsilon}$. The magnitude of Q, based on two analytical techniques at temperatures of 200, 300, 400 and 450°C under three different strain rates, ranged between approximately 48 and 62 KJ/mole. Considering an average of these two numbers as Q, it can be stated that an activation energy of 55 KJ/mole can be attained for Alloy C-276 in the tested temperature range. The $(m+\beta)$ values, determined from these analyses, ranged between 2 and 3, which has been cited in the literature [8-11] to be the result of substitutional diffusion of solute elements into the metal lattice. Elements such as Chromium (Cr), Cobalt (Co) and Molybdenum (Mo) that are present in Alloy C-276 could constitute such solute elements. It should, however, be noted that no standard value or ranges in Q for Alloy C-276 are available in the open literature. Thus, additional evaluations using similar techniques are needed in the near future to verify the magnitude of the Q value, estimated in this study.

As indicated in the previous chapter, the strain hardening exponent (n) could not be determined from the conventional Hollomon relationship that provides a linear relationship between the true stress (σ) and the true strain (ε). By superimposing a non-linear relationship between these two parameters, as proposed by Ludwigson on the Hollomon relationship, and considering the best available linear plot, the estimated n value was found to range between 0.68 and 0.75. Once again, no standard value of n exists in the published literature that can be compared to the experimental value determined from this investigation.

As to the determination of the fracture toughness (K_{1C}) value of the tested material, a difficulty was experienced with the testing equipment. Therefore, future efforts are needed to estimate K_{1C} using a similar approach.

The SCC testing involving pre-cracked DCB specimens did not exhibit appreciable crack extension at a shorter duration of 15 days, irrespective of the initial stress intensity factor (K_I) value. However, measurable crack extensions were seen at a longer duration of 30 days for three levels of increasing K_I values. It is also of interest to note that the final loads borne by the DCB specimens at both durations were significantly reduced even though the 15-day test did not exhibit any appreciable crack extension. The lack of crack extension following 15 days exposure of the DCB specimen could be attributed to the weakening of the cohesive bond due to the combined effect of the load imparted by the wedge and the testing environment.

As to the SCC testing using self-loaded C-ring and U-bend specimens, no cracking was initiated along their convex surfaces, which are subjected to tensile loading. Thus, additional testing in a similar environment is recommended to be performed at higher temperatures. The corrosion rate based on the weight-loss of coupons was found to gradually reduce with increasing test duration.

The fractographic evaluation of the specimens, tested up to a temperature of 600°C, revealed predominantly ductile failures characterized by dimples. However, intergranular brittle failures were observed at 700 and 800°C. The analysis of these specimens by XRD revealed the formation of precipitates of $M_{23}C_6$ type, suggesting that the intergranular cracking at these two temperatures could be the result of precipitates of brittle phases containing the carbides of Cr, Mo and Co.

CHAPTER 6

SUMMARY AND CONCLUSIONS

This investigation was focused on characterizing the plastic deformation of a leading candidate structural material, namely austenitic Alloy C-276, under tensile loading at temperatures relevant to the H_2SO_4 decomposition process related to the S-I cycle. Transmission Electron Microscope (TEM) was used to develop a basic understanding of high temperature deformation in terms of dislocation density (ρ). The phenomenon of dynamic strain ageing (DSA), observed with Alloy C-276 was investigated in terms of two important parameters including temperature and strain rate ($\dot{\varepsilon}$). The susceptibility of this alloy to stress-corrosion-cracking (SCC) in the presence of a crack was determined using a fracture mechanics approach. Limited study was also conducted using self-loaded specimens and coupons to evaluate the SCC behavior and general corrosion rate, respectively of this alloy. The evaluation of fracture toughness (K_{1C}) was also attempted. The key results obtained from this investigation are summarized below.

- The tensile strength in terms of YS and UTS was gradually reduced with increasing temperature due to enhanced plastic flow and ease of deformation at elevated temperatures.

- The magnitude of failure strain (e_f) was gradually reduced within an approximate temperature regime of ambient to 300°C. The reduced e_f in this temperature regime is attributed to a well-known metallurgical phenomenon known as DSA.
- DSA is known to be the result of solute diffusion into the metal lattice, thus impeding the dislocation movement from one grain to another. The characterization of defects by TEM revealed relatively higher values of ρ in specimens tested between 200 and 300°C. The magnitude of ρ at 450°C was comparatively lower.
- The determination of the activation energy (Q) based on different temperatures and strain rates revealed an average Q value of 55 KJ/mole.
- The estimated strain hardening exponent (n), determined from the superimposition of Hollomon and Ludwigson approaches ranged between 0.68 and 0.75 for specimens tested at 200, 300, 400 and 450°C.
- The cracking susceptibility of Alloy C-276 in the presence of an acidic solution was more pronounced at longer test duration of 30 days, showing enhanced crack extension. The increase in crack length was directly related to the magnitude of the initial stress intensity factor values.
- The fractographic evaluations of the DCB specimens by scanning electron microscopy (SEM) revealed three distinct regions, namely striations, cleavage failure and dimples, which are the characteristics of cyclic loading, SCC and fast fracture, respectively.

- The C-ring and U-bend specimens did not exhibit any cracking even after an exposure of 56 days in a 150°C acidic solution. Further, the corrosion rate in terms of mpy was gradually reduced with longer exposure time.
- The SEM micrographs of the tensile specimens tested at temperatures ranging from ambient to 600°C showed dimpled microstructures, indicating ductile failures. However, intergranular brittle failures were seen in specimens tested at higher temperatures (700 and 800°C).
- The analysis of precipitates observed at 800°C by x-ray diffraction (XRD) revealed the presence of carbides of $M_{23}C_6$ type. The resultant diffraction patterns resemble the standard peaks corresponding to the carbides of elements including Cr, Mo and Co.

CHAPTER 7

SUGGESTED FUTURE WORK

- Determination of K_{1C} at ambient and elevated temperatures.
- Determination of impact resistance and ductile-brittle transition temperature.
- Determination of K_{1SCC} at higher temperatures and longer test durations.
- SCC evaluation using self-loaded specimens at elevated temperatures.
- Crack initiation and propagation studies in the presence of H_2SO_4 at elevated temperatures using in-situ (DCPD) monitoring device.

APPENDIX A

TENSILE TESTING DATA

A1 Stress-Strain Diagrams using Smooth Specimens Tested at a Strain Rate of 5×10^{-4} sec^{-1}. (Conversion factor of 1 ksi = 6.895 MPa can be used wherever applicable)

A1.1 Stress-Strain Diagrams at Room Temperature

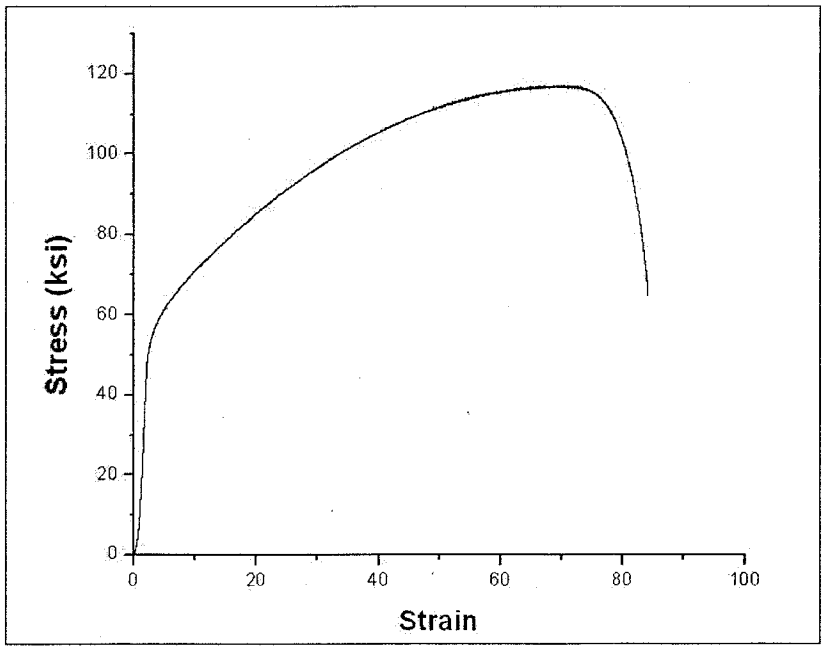

Sample 1

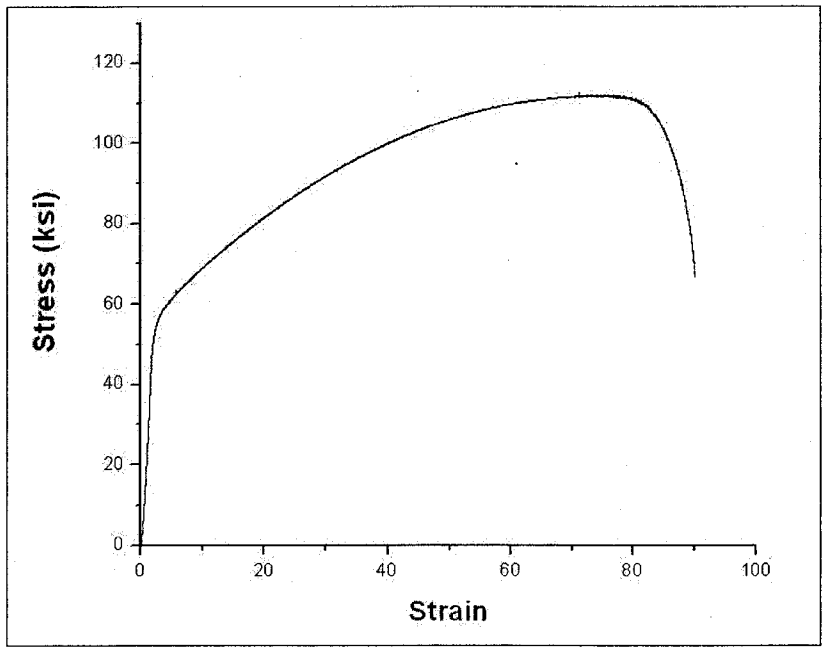

Sample 2

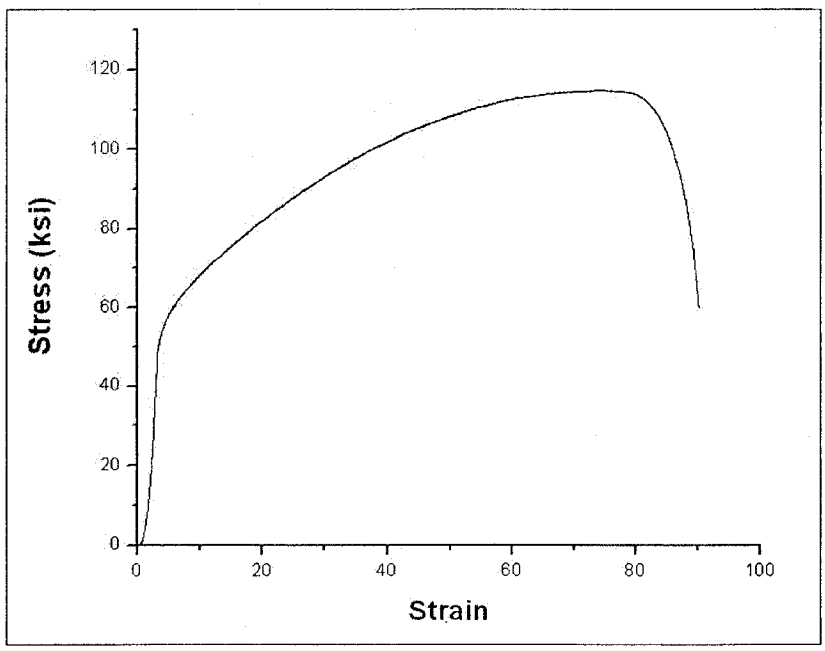

Sample 3

A1.2 Stress-Strain Diagrams at 100°C

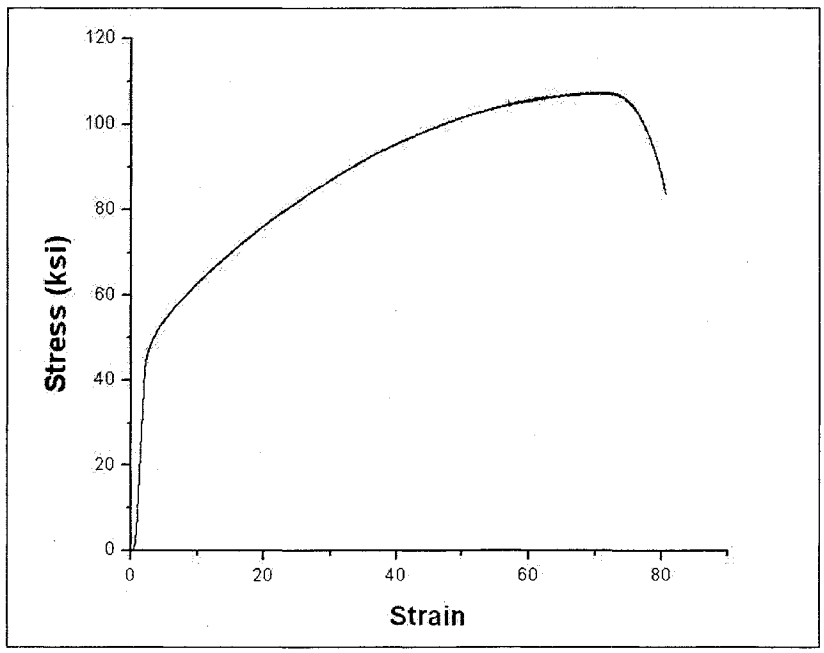

Sample 1

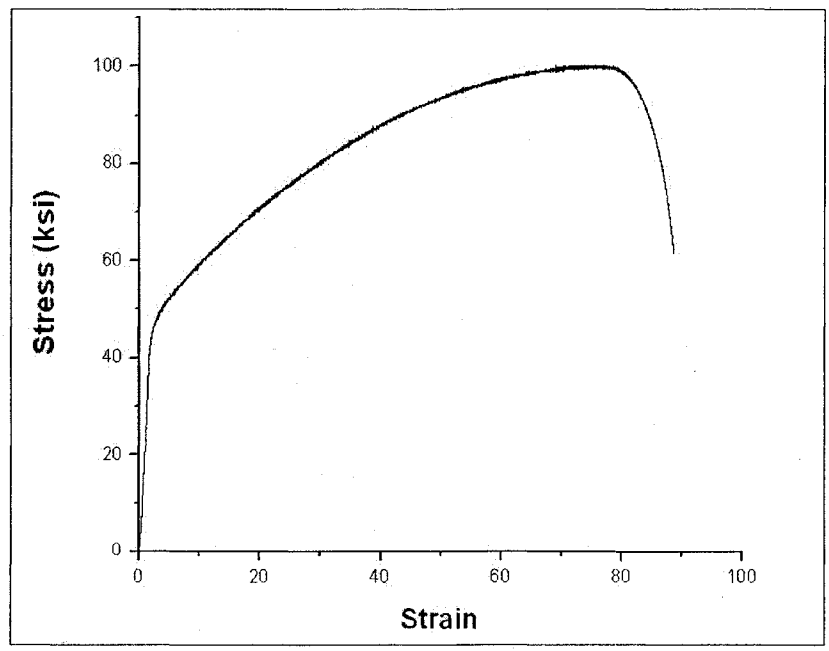

Sample 2

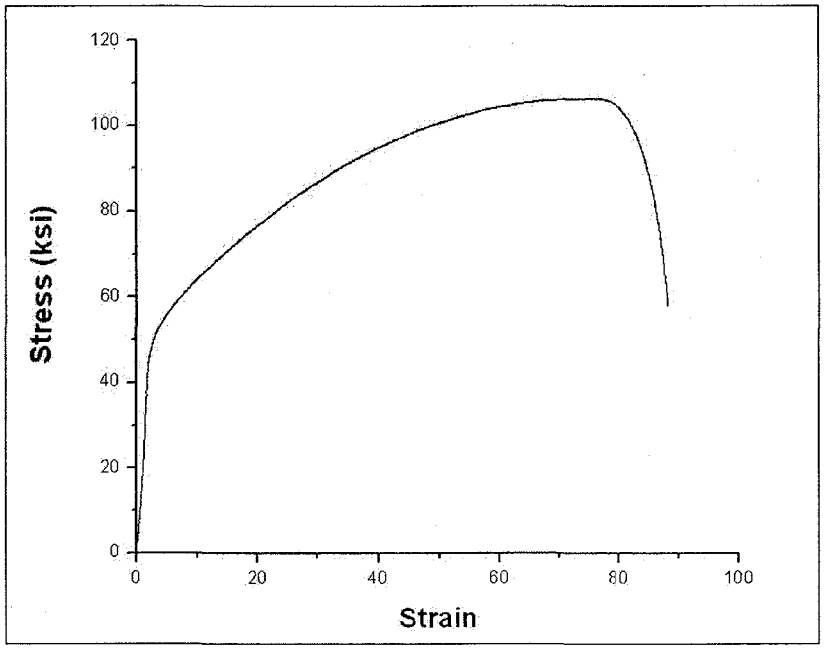

Sample 3

A1.3 Stress-Strain Diagrams at 200°C

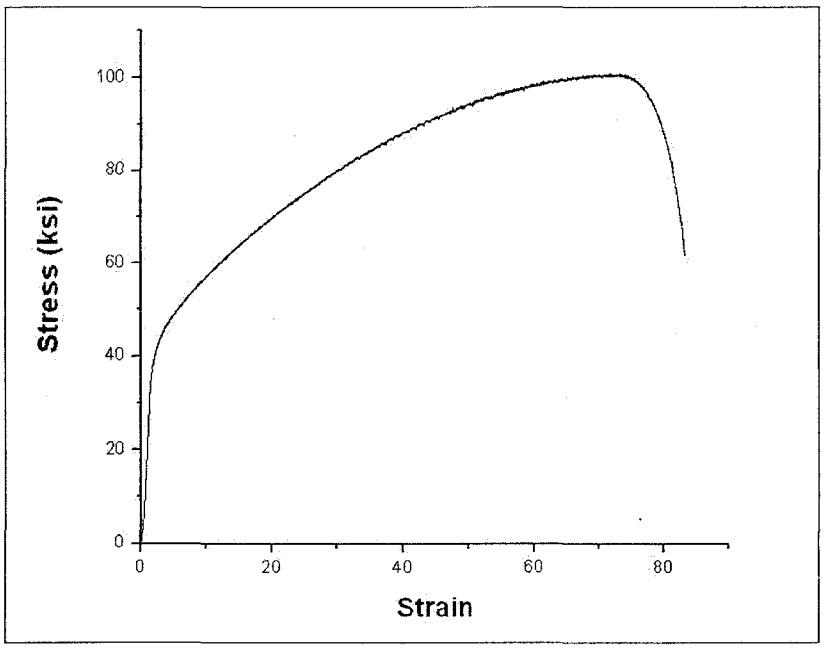

Sample 1

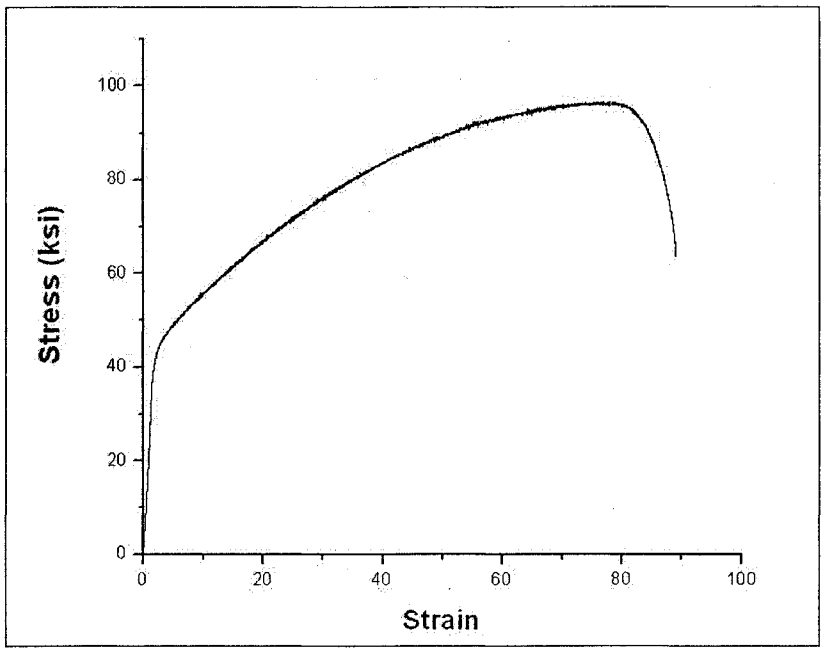

Sample 2

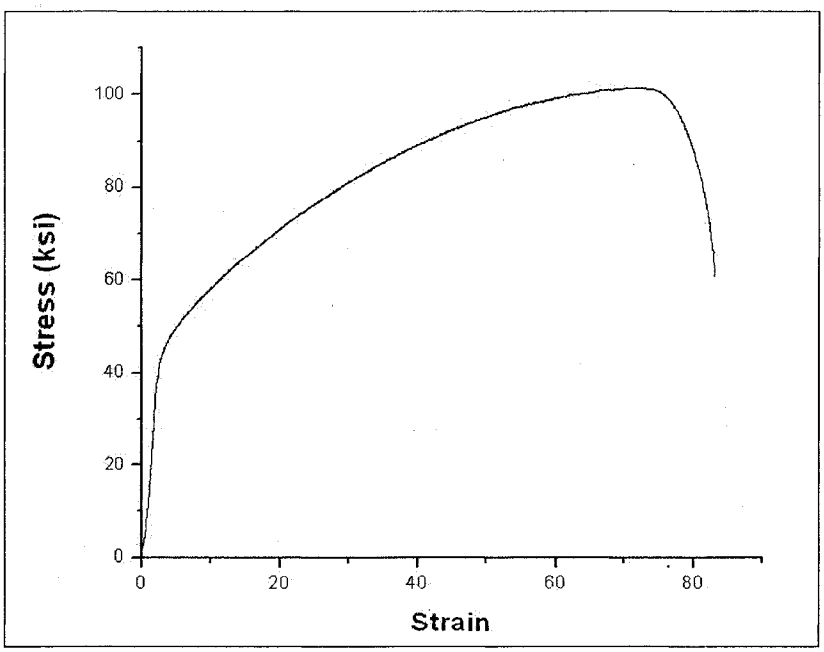

Sample 3

A1.4 Stress-Strain Diagrams at 300°C

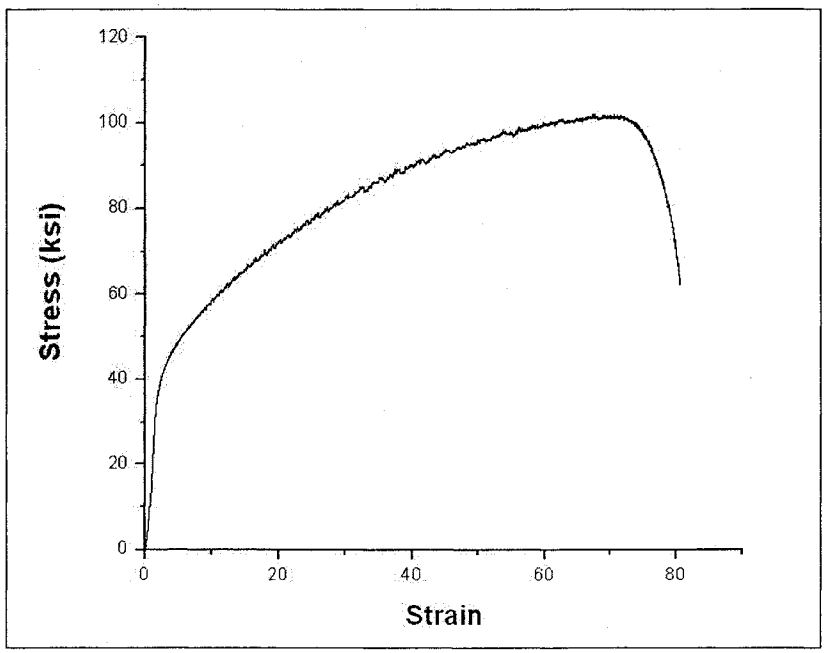

Sample 1

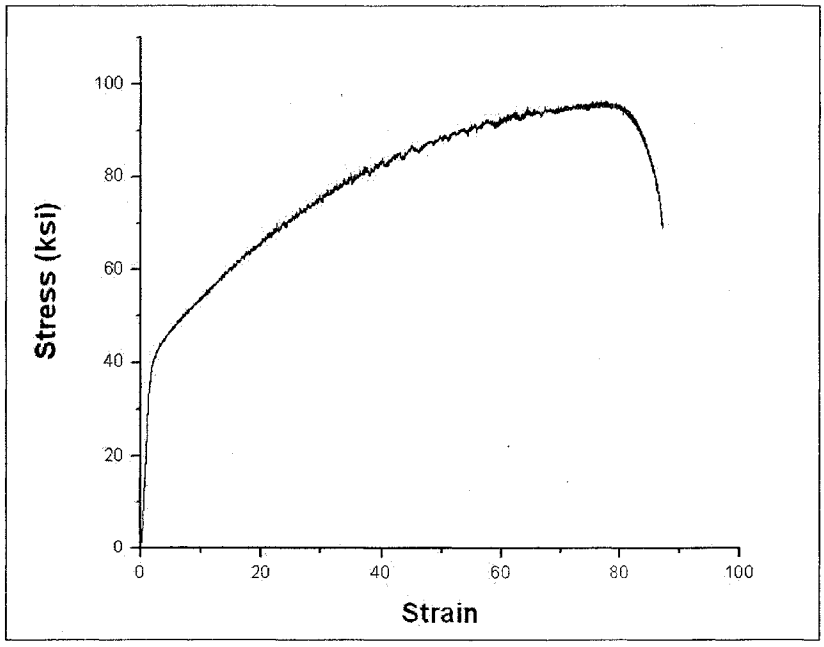

Sample 2

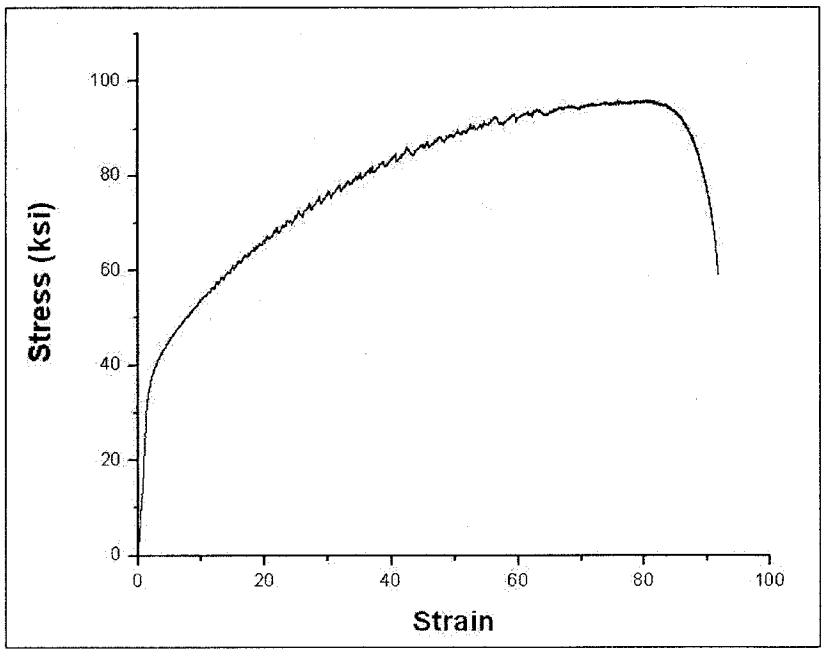

Sample 3

A1.5 Stress-Strain Diagrams at 400°C

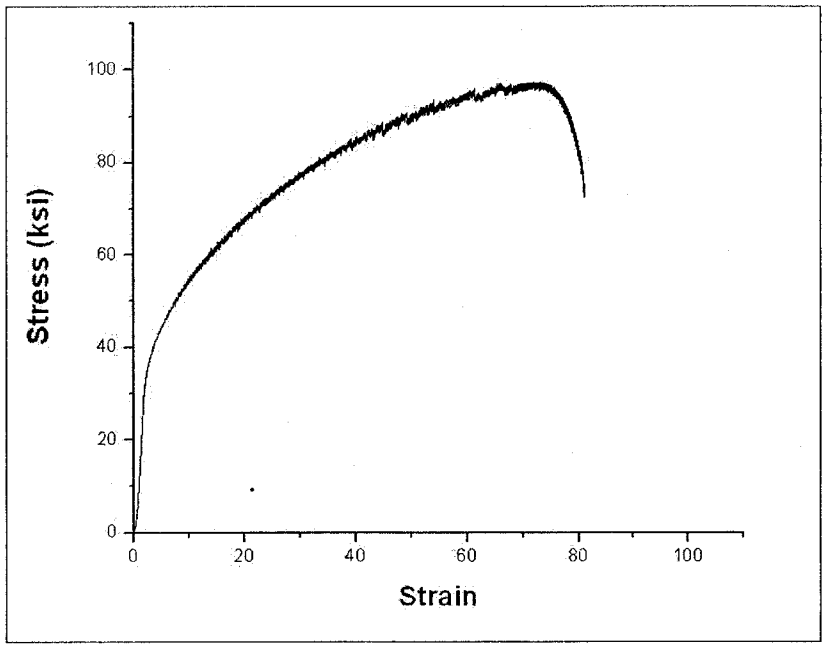

Sample 1

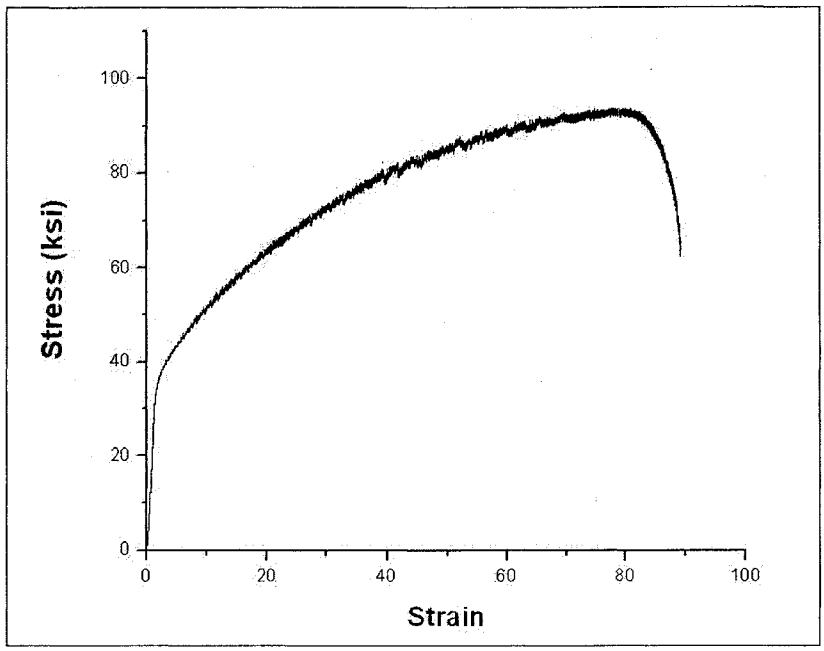

Sample 2

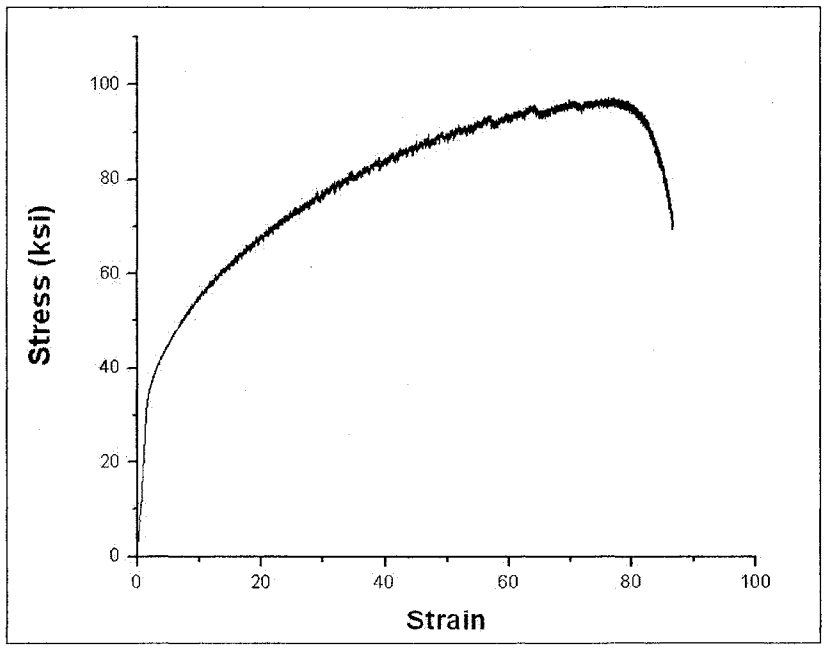

Sample 3

A1.6 Stress-Strain Diagrams at 450°C

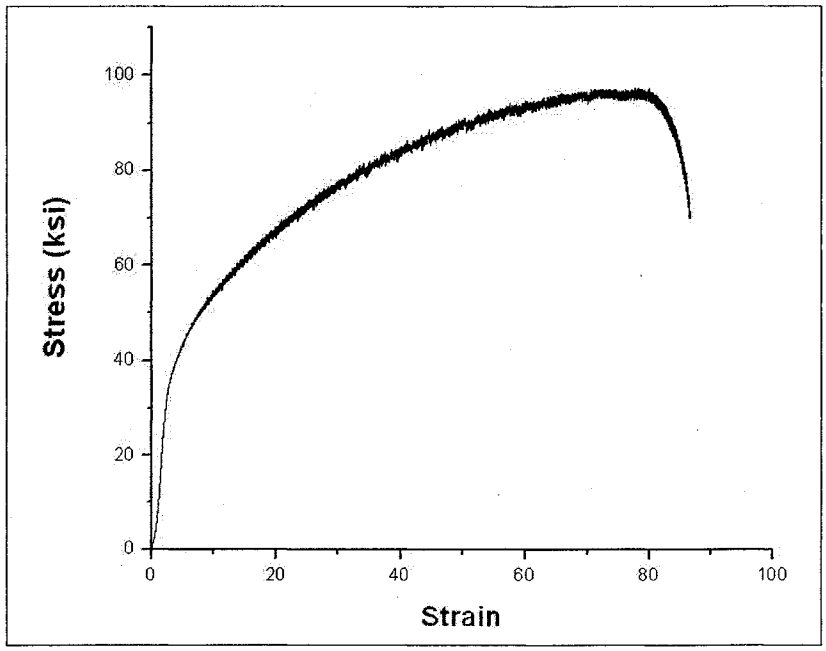

Sample 1

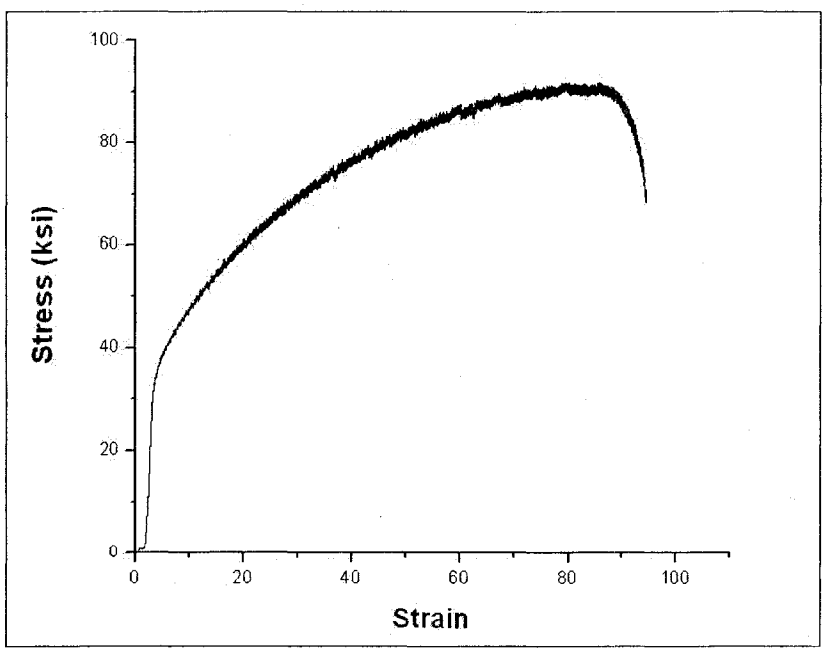

Sample 2

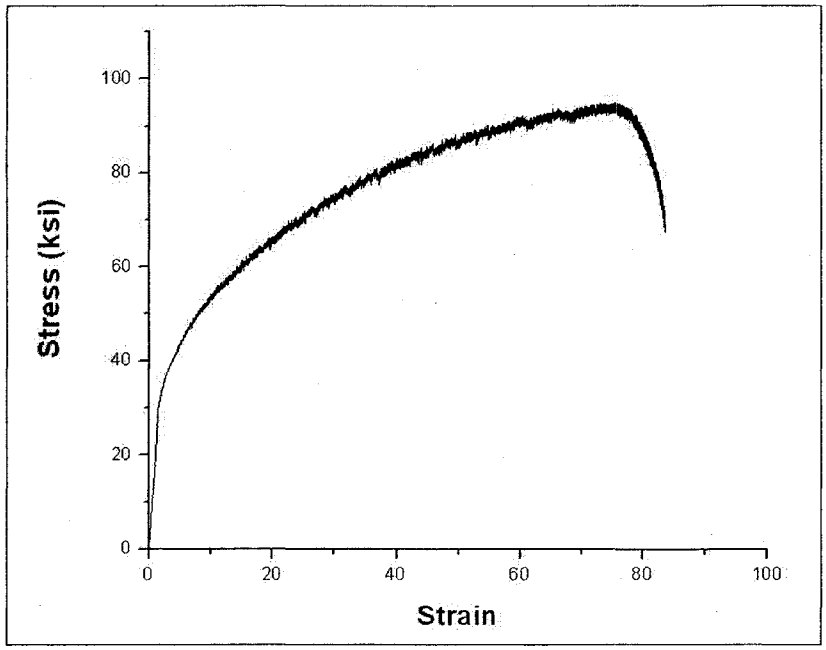

Sample 3

A1.7 Stress-Strain Diagrams at 600°C

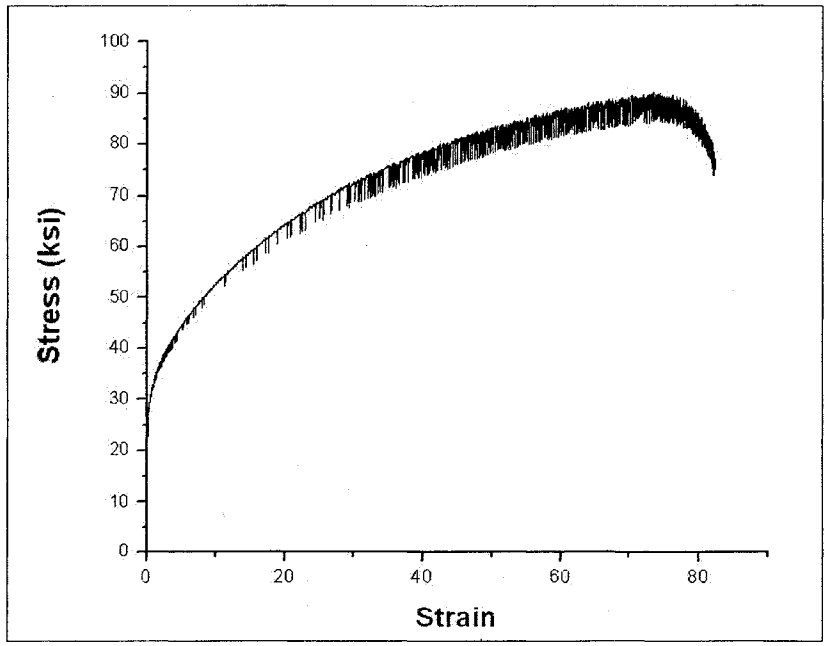

Sample 1

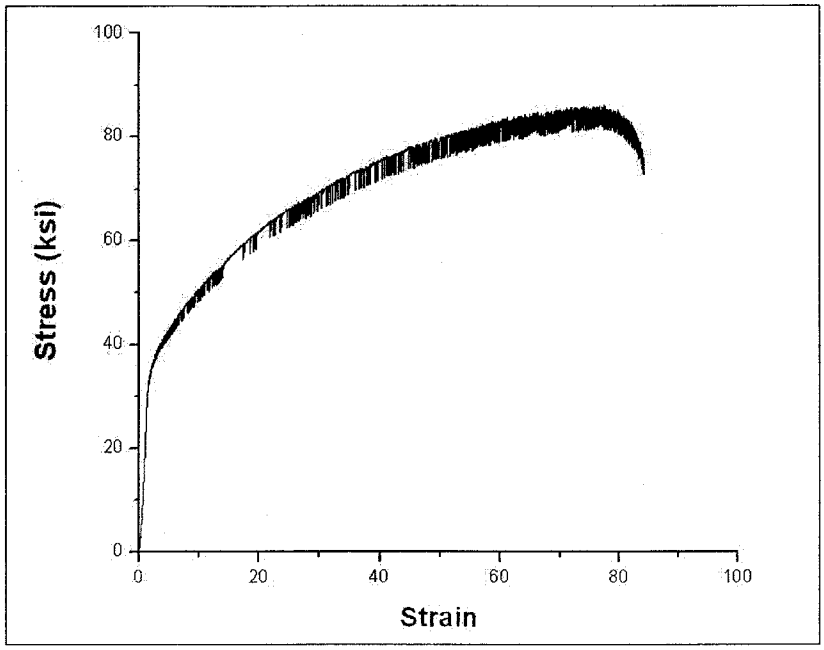

Sample 2

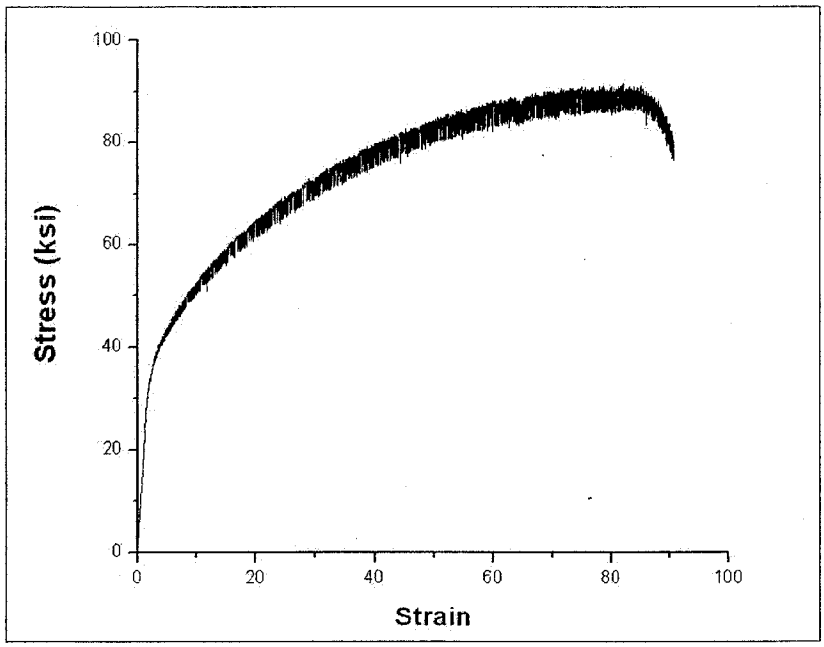

Sample 3

A1.8 Stress-Strain Diagrams at 700°C

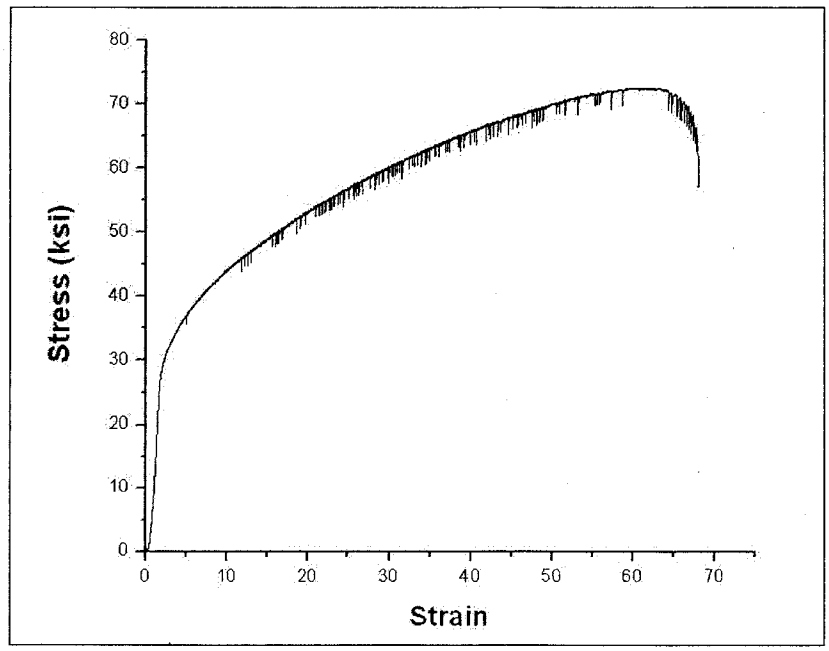

Sample 1

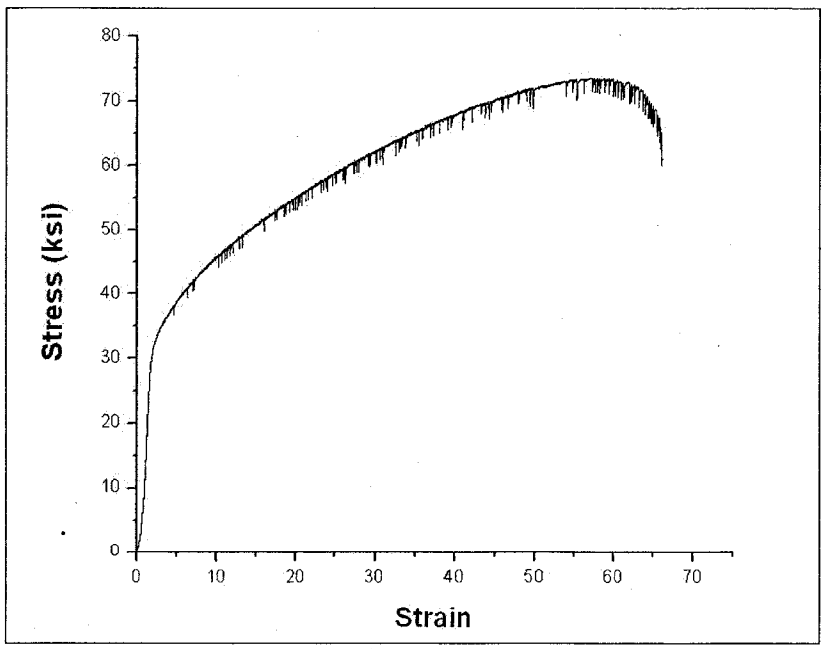

Sample 2

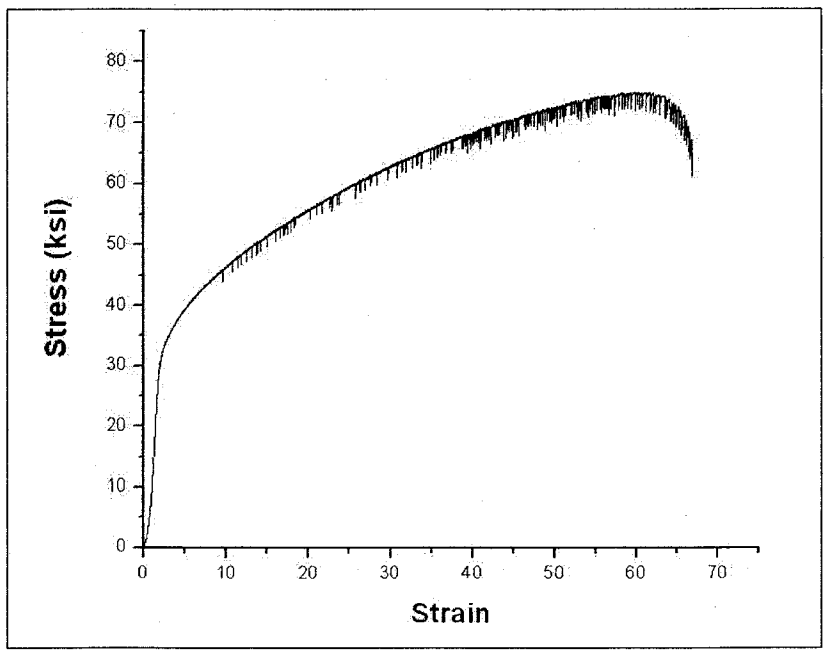

Sample 3

A1.9 Stress-Strain Diagrams at 800°C

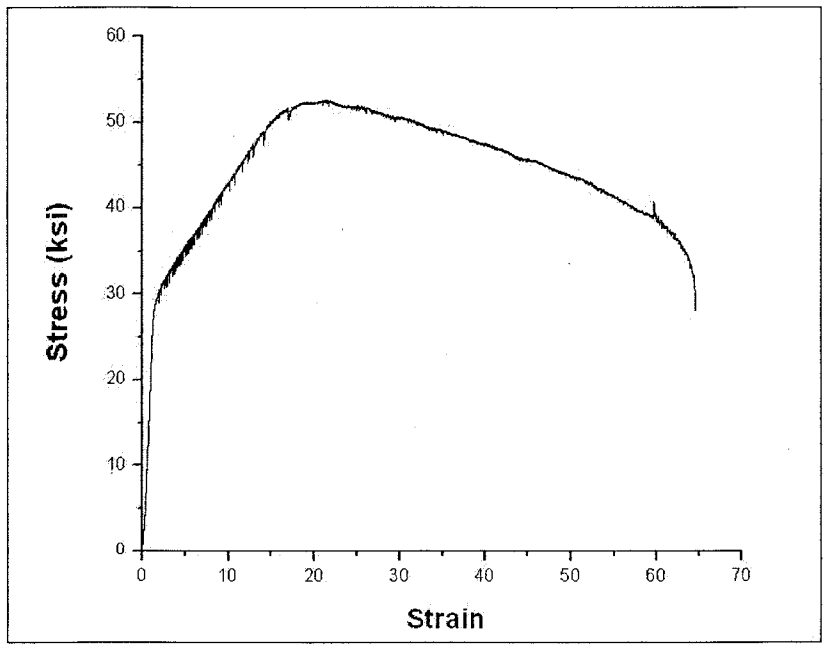

Sample 1

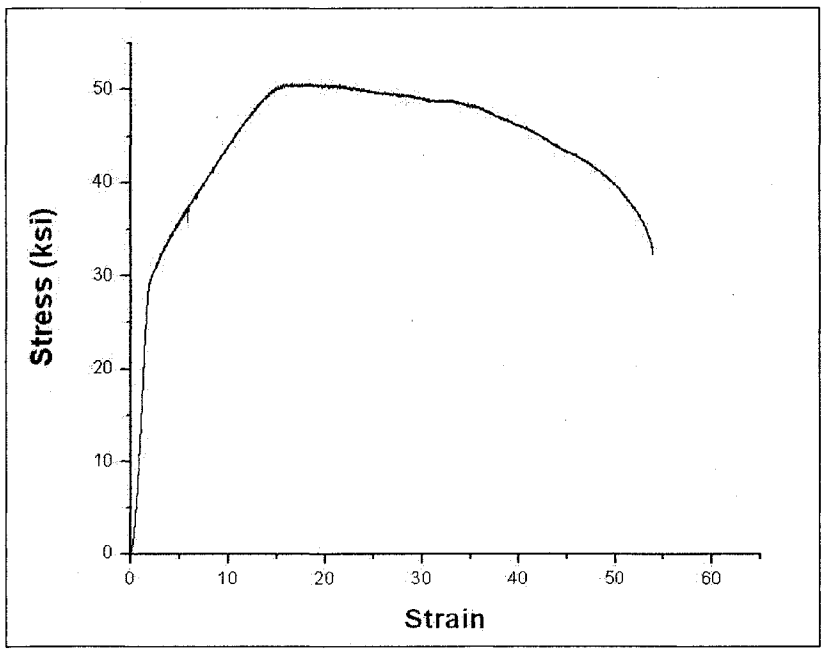

Sample 2

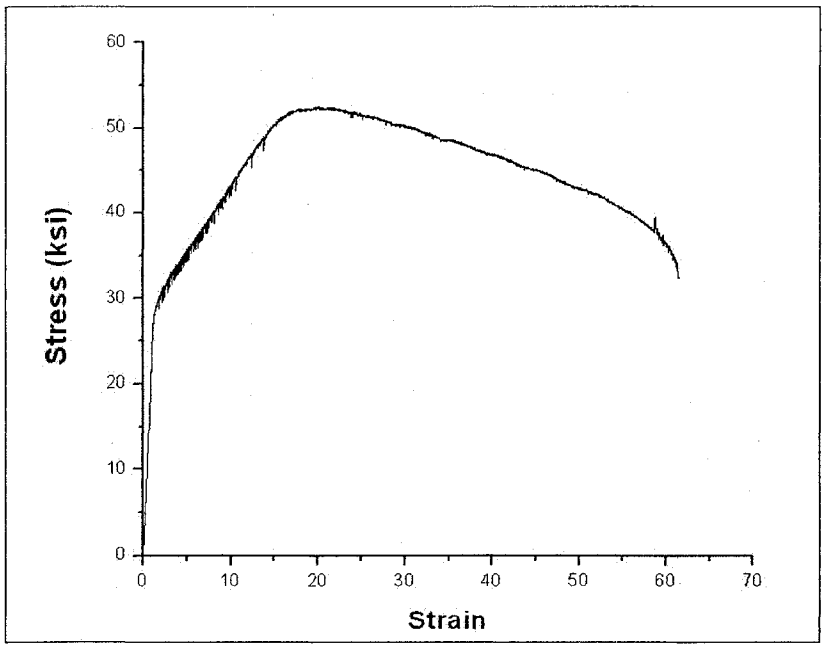

Sample 3

A1.10 Stress-Strain Diagrams at 900°C

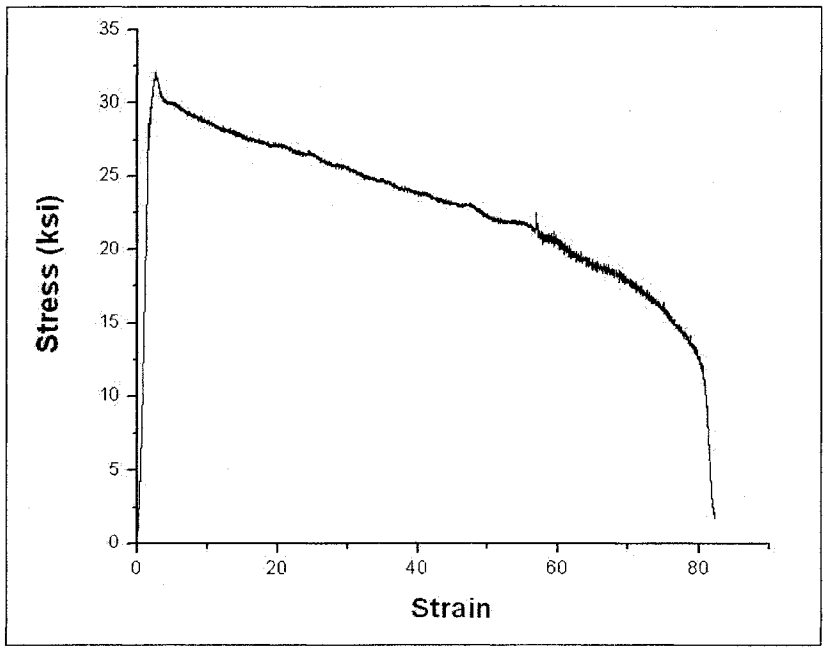

Sample 1

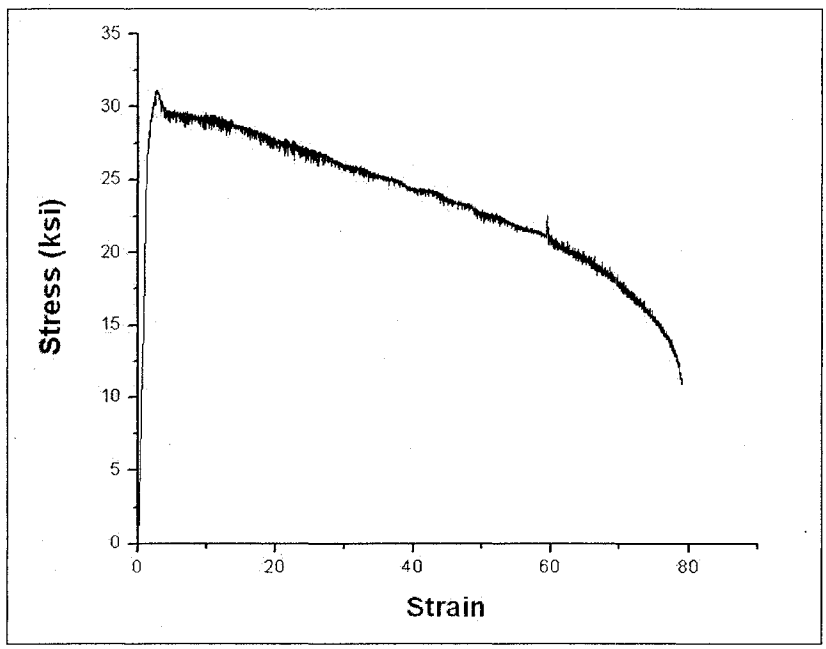

Sample 2

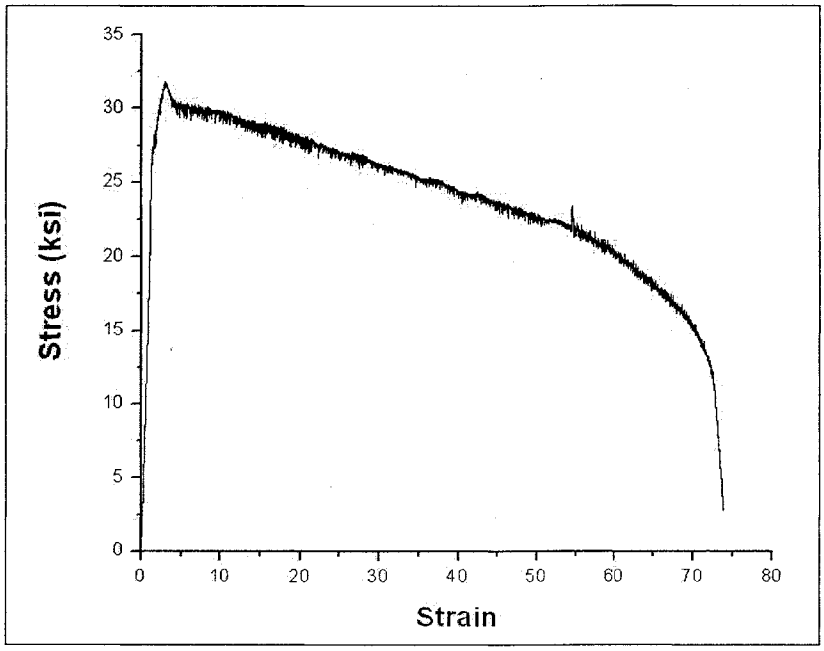

Sample 3

A1.11 Stress-Strain Diagrams at 1000°C

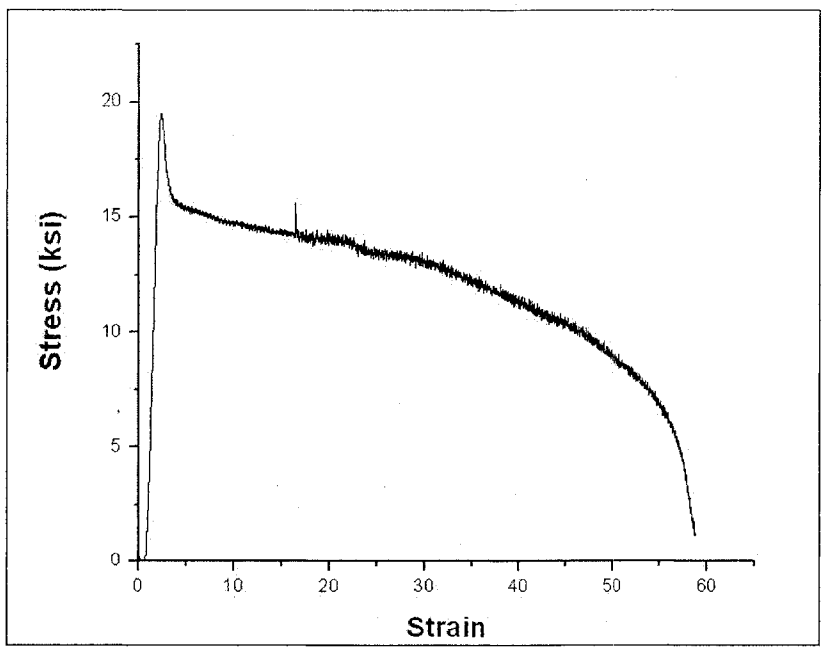

Sample 1

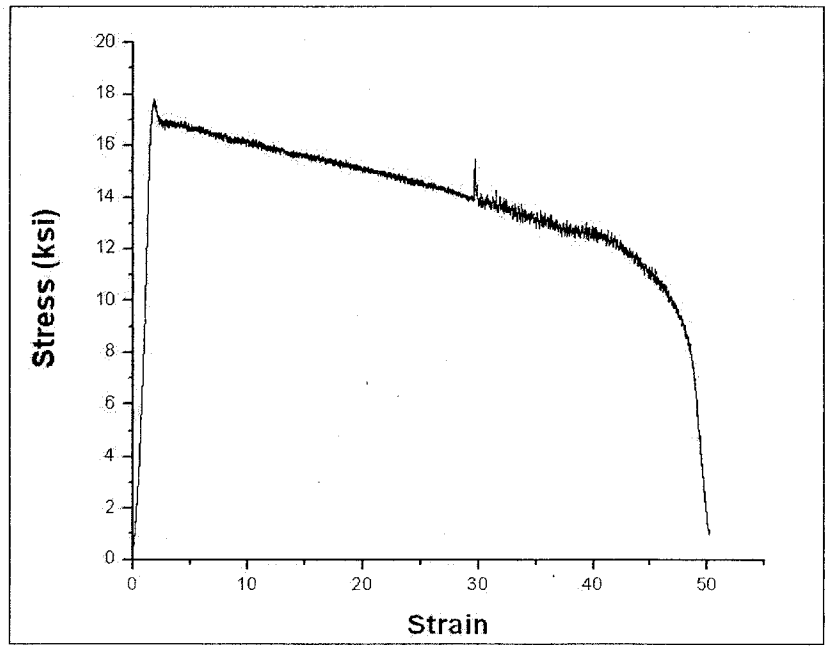

Sample 2

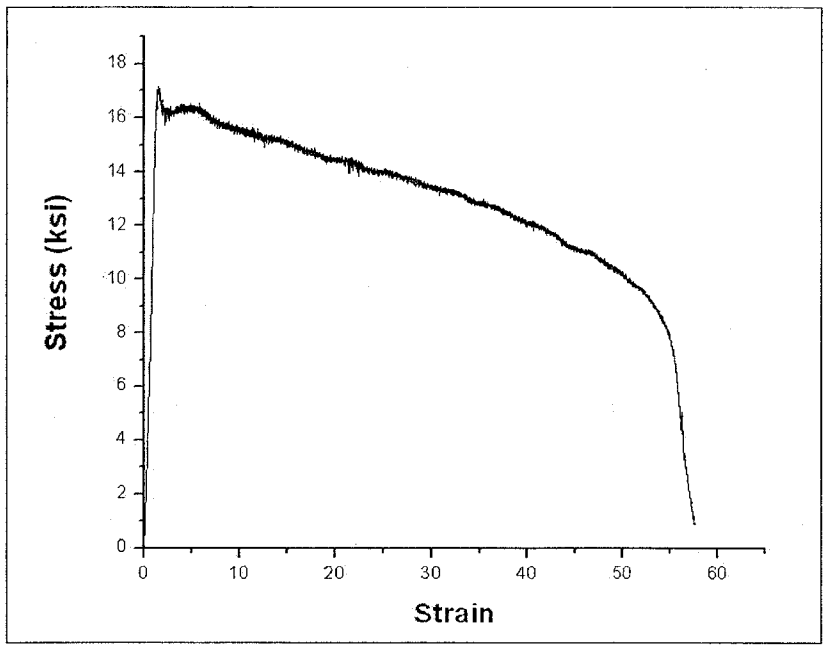

Sample 3

Table A1 Combined Tensile Properties at Strain Rate of 5×10^{-4} sec^{-1} (1ksi = 6.895 MPa)

Temperature (°C)	Sample #	YS (ksi)	UTS (ksi)	%El	%RA
RT	Sample 1	50.6	117.1	83.5	74.7
	Sample 2	51.7	112.8	90.1	78.6
	Sample 3	51.8	115.6	86.8	81.7
100	Sample 1	44.8	107.5	81.4	71.7
	Sample 2	42.4	100.4	87.0	76.7
	Sample 3	47.0	107.2	86.1	81.6
200	Sample 1	36.5	102.5	82.9	74.8
	Sample 2	39.7	96.8	87.4	77.2
	Sample 3	42.1	102.9	81.3	75.8
300	Sample 1	36.0	101.9	79.2	67.7
	Sample 2	37.3	96.5	85.9	72.1
	Sample 3	40.0	98.2	88.9	77.9
400	Sample 1	33.0	97.5	80.0	69.2
	Sample 2	33.9	93.7	88.0	74.6
	Sample 3	34.9	96.9	85.6	74.9
450	Sample 1	32.6	97.4	87.1	76.3
	Sample 2	32.4	91.7	92.3	78.6
	Sample 3	32.2	95.0	84.9	73.4
600	Sample 1	30.0	90.3	81.3	65.4
	Sample 2	31.5	86.0	83.6	65.4
	Sample 3	31.0	91.2	84.9	71.0
700	Sample 1	28.8	72.5	66.9	54.4
	Sample 2	30.8	73.7	65.2	52.9
	Sample 3	30.7	75.0	65.5	51.0
800	Sample 1	28.6	52.7	64.3	52.2
	Sample 2	29.6	50.7	52.9	46.3
	Sample 3	28.4	52.5	61.1	46.6
900	Sample 1	28.3	32.0	82.8	63.5
	Sample 2	27.4	31.2	79.3	59.5
	Sample 3	28.1	31.8	74.5	61.4
1000	Sample 1	19.4	19.5	59.5	57.1
	Sample 2	17.4	17.8	50.2	40.8
	Sample 3	16.7	17.2	57.4	41.6

A2 Stress-Strain Diagrams using Smooth Specimens Tested at a Strain Rate of 10^{-3} sec^{-1}.

(Conversion factor of 1 ksi = 6.895 MPa can be used wherever applicable)

A2.1 Stress-Strain Diagrams at 200°C

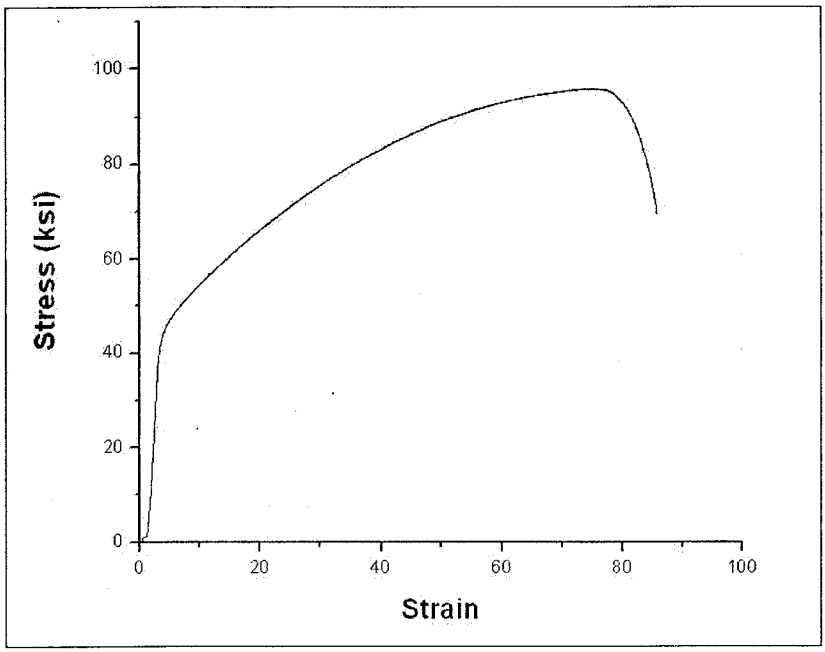

Sample 1

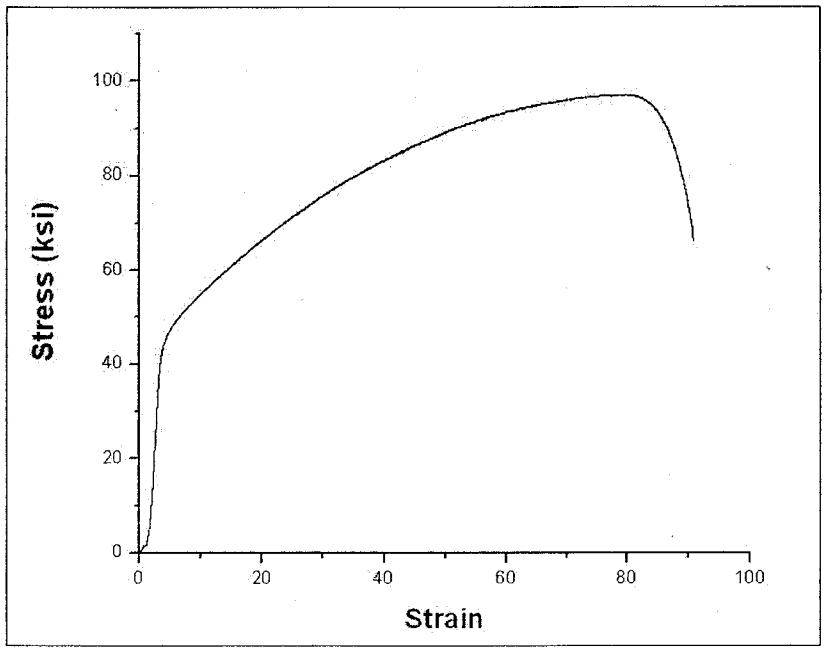

Sample 2

A2.2 Stress-Strain Diagrams at 300°C

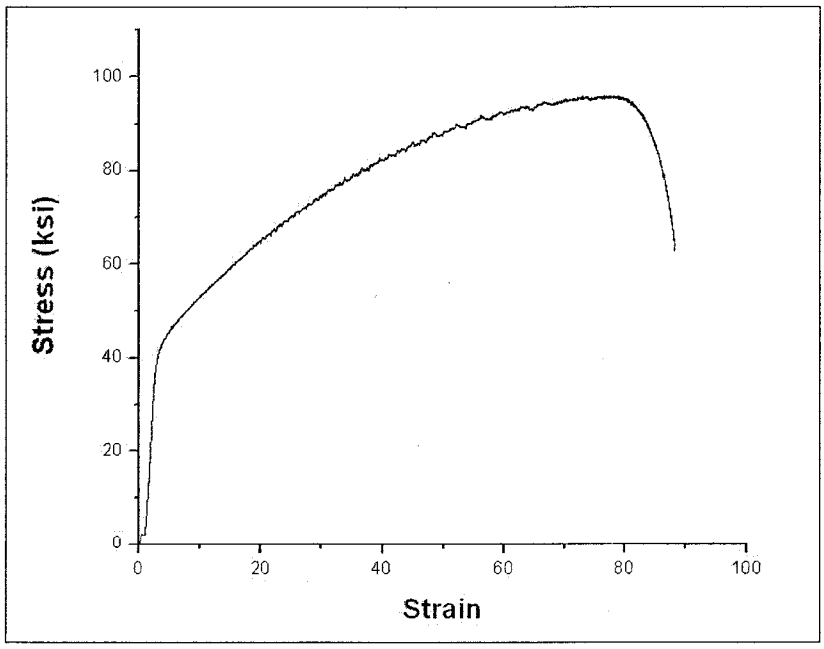

Sample 1

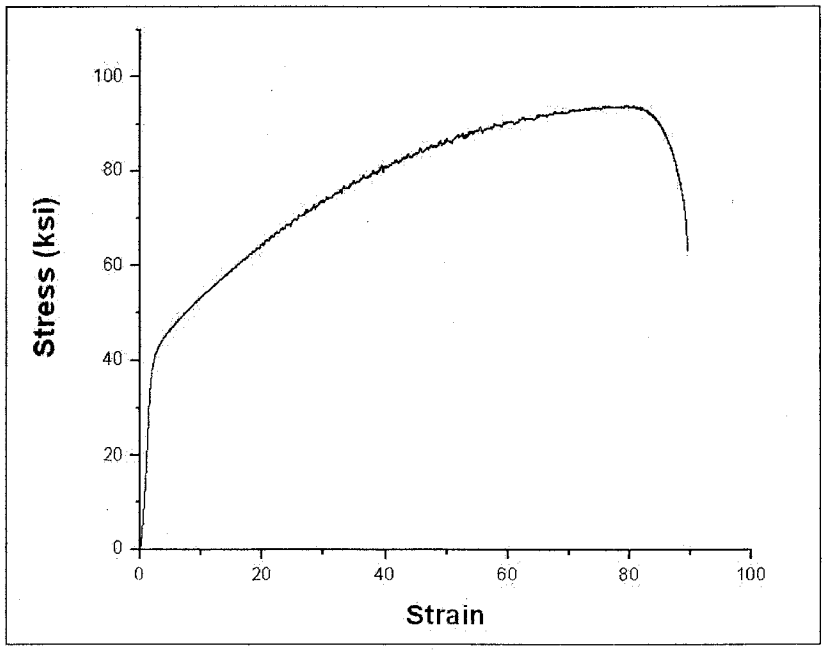

Sample 2

A2.3 Stress-Strain Diagrams at 400°C

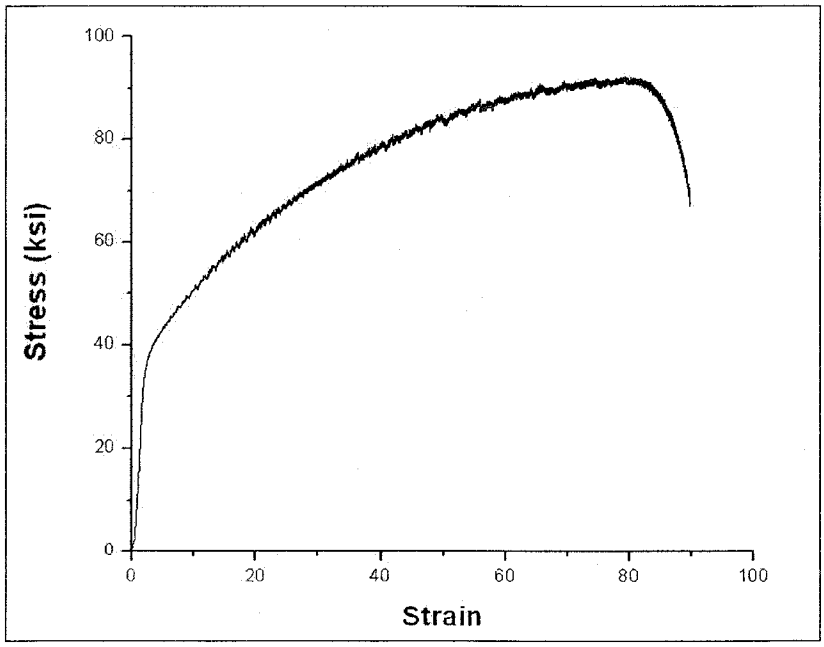

Sample 1

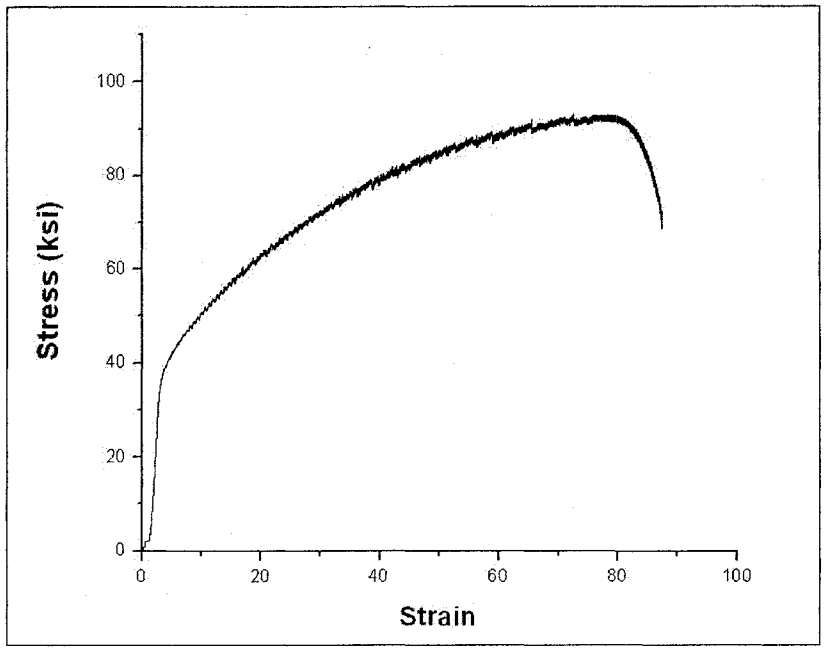

Sample 2

A2.4 Stress-Strain Diagrams at 450°C

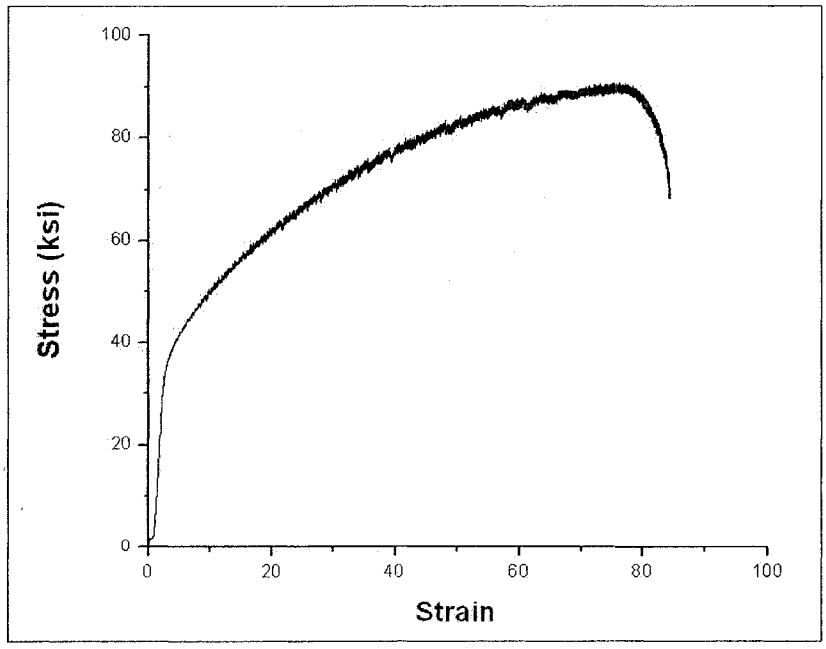

Sample 1

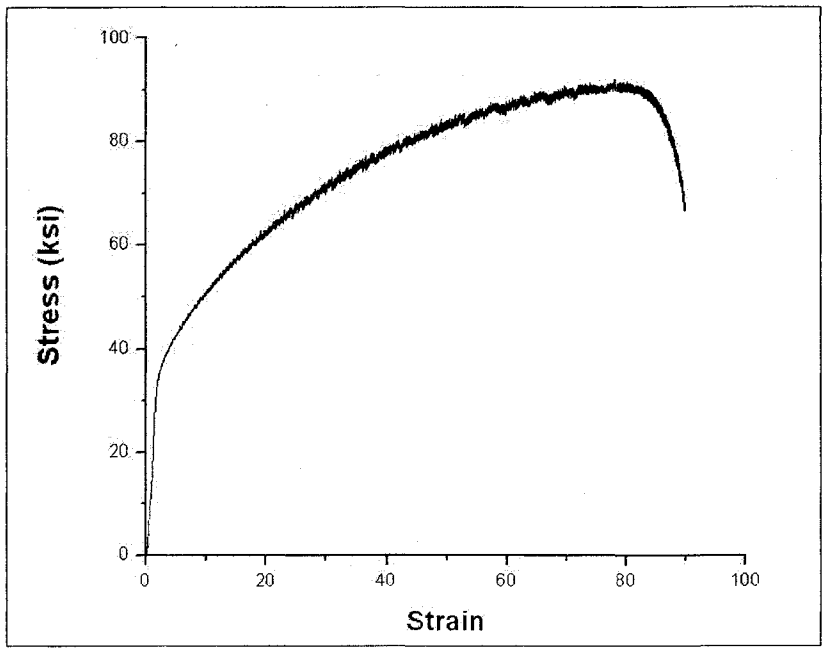

Sample 2

A3 Stress-Strain Diagrams using Smooth Specimens Tested at a Strain Rate of 10^{-4} sec^{-1}.

(Conversion factor of 1 ksi = 6.895 MPa can be used wherever applicable)

A3.1 Stress-Strain Diagrams at 200°C

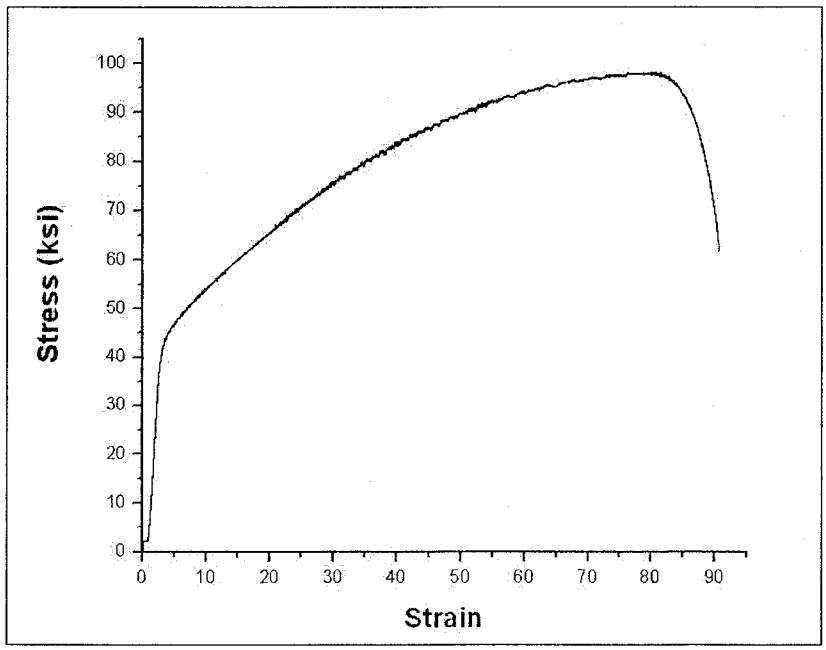

Sample 1

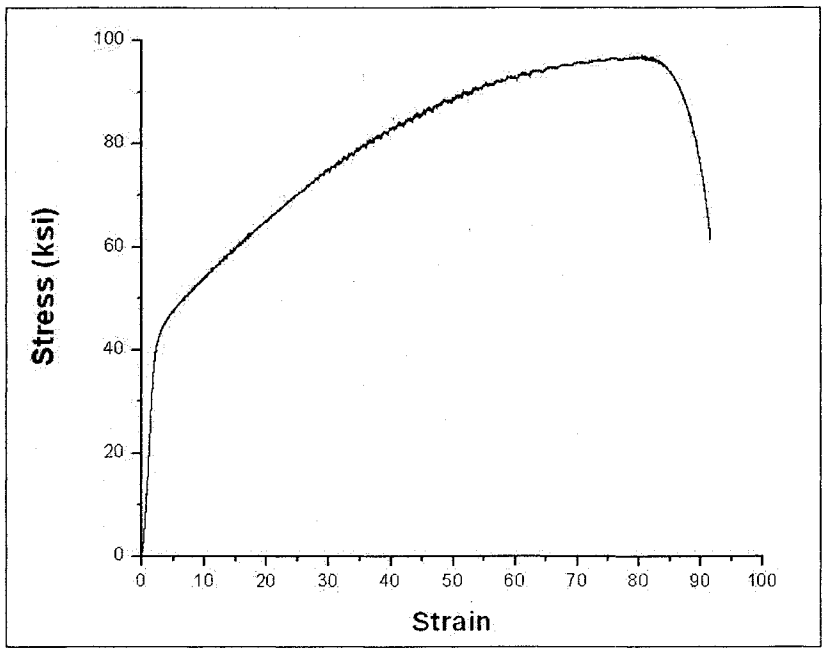

Sample 2

A3.2 Stress-Strain Diagrams at 300°C

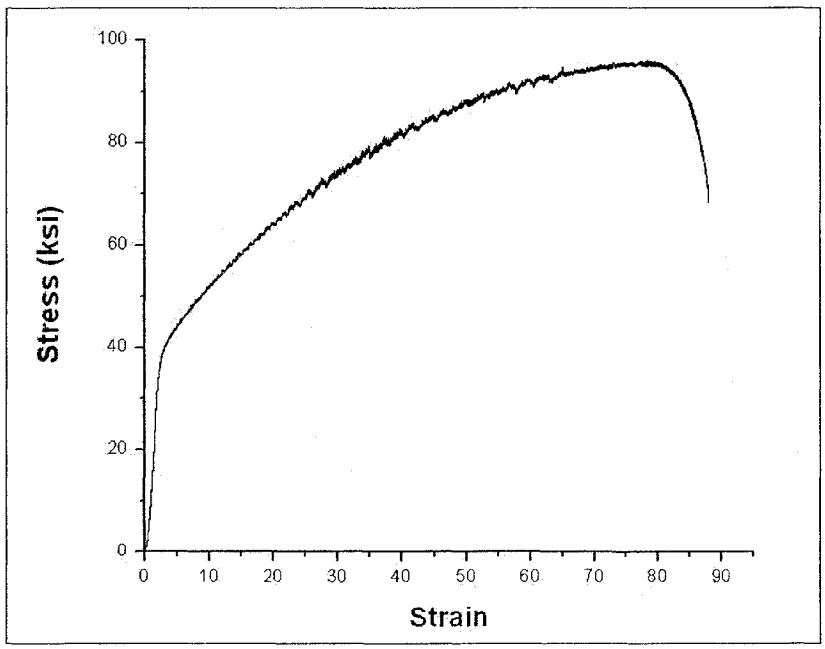

Sample 1

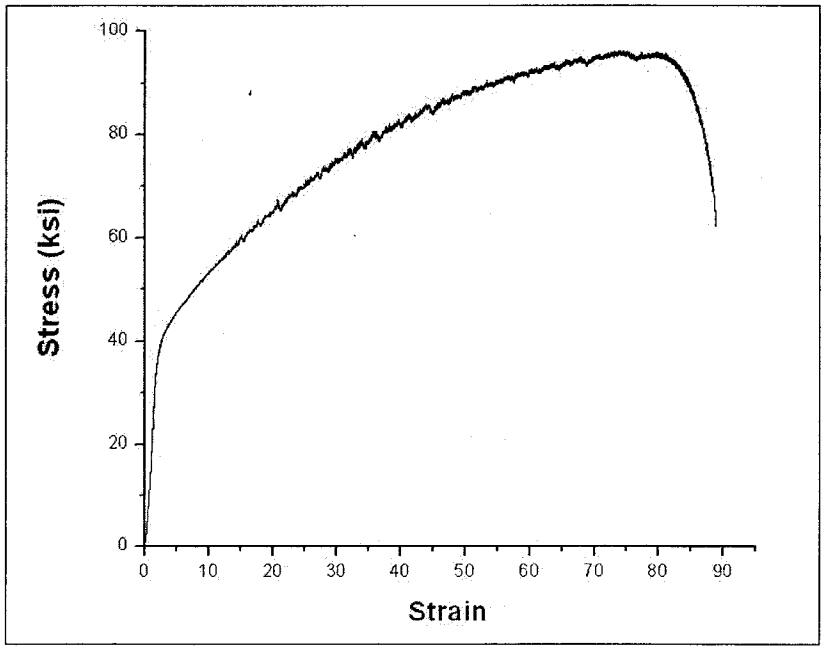

Sample 2

A3.3 Stress-Strain Diagrams at 400°C

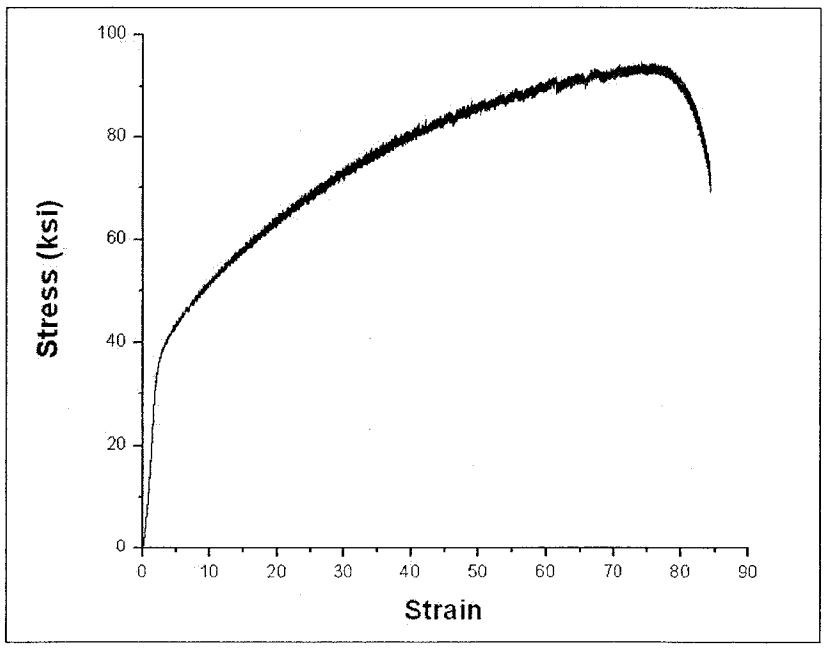

Sample 1

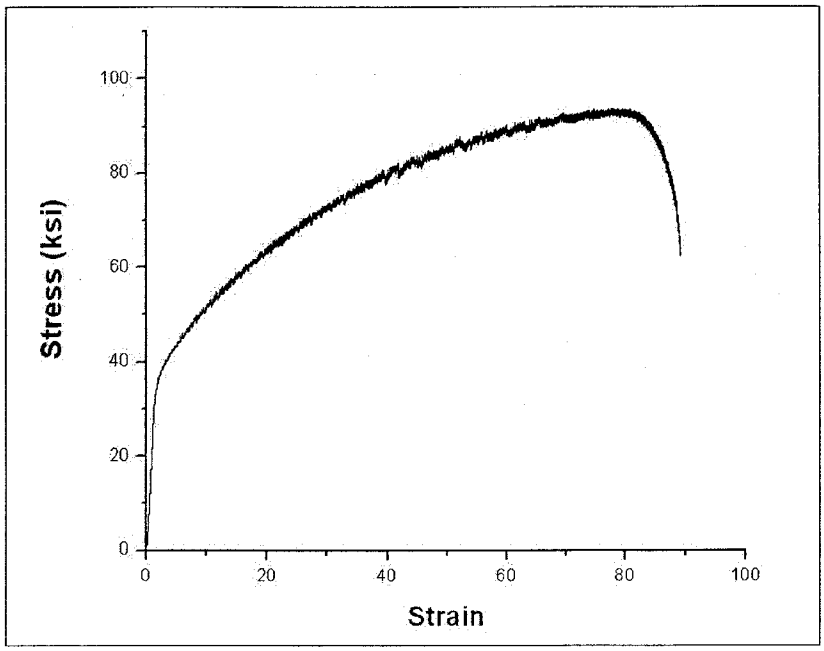

Sample 2

A3.4 Stress-Strain Diagrams at 450°C

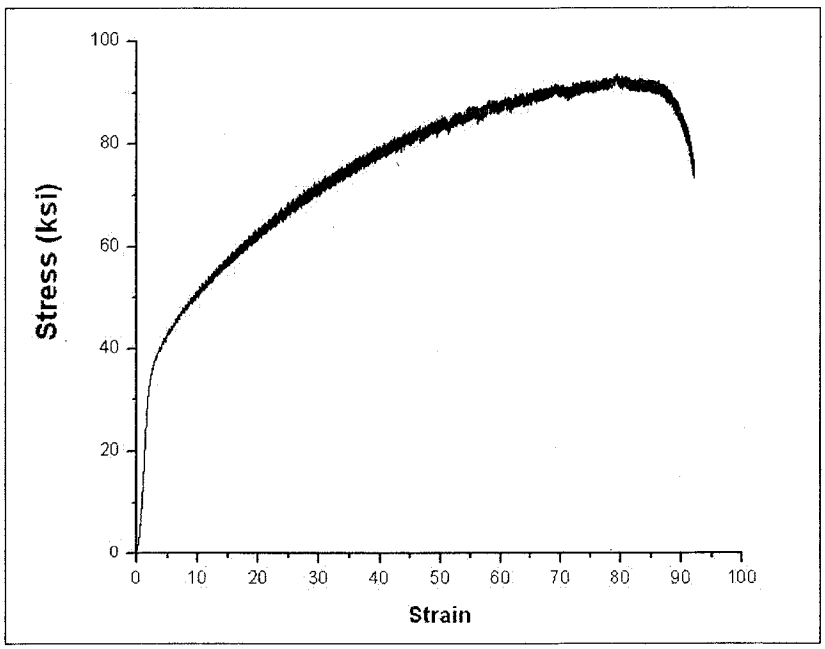

Sample 1

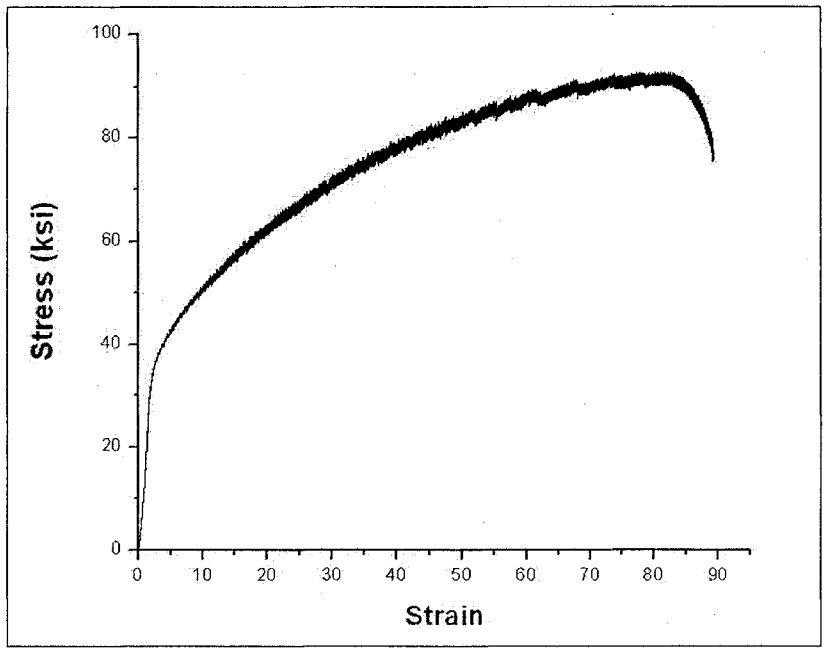

Sample 2

A5 Strain Hardening Exponent (n) vs. Temperature

A5.1 n vs. Temperature at a Strain Rate of 5×10^{-4} sec^{-1}

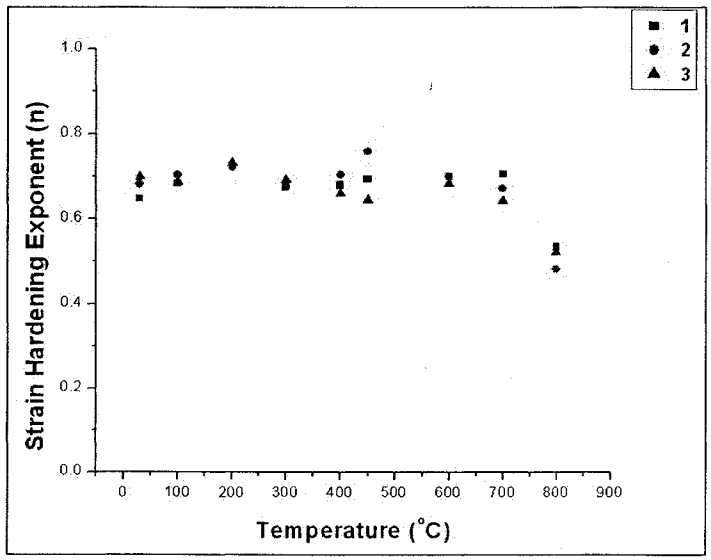

n vs. Temperature (3 Sets of Experimental Data)

A5.2 n vs. Temperature at 3 Strain Rates (10^{-3}, 5×10^{-4} and 10^{-4} sec^{-1})

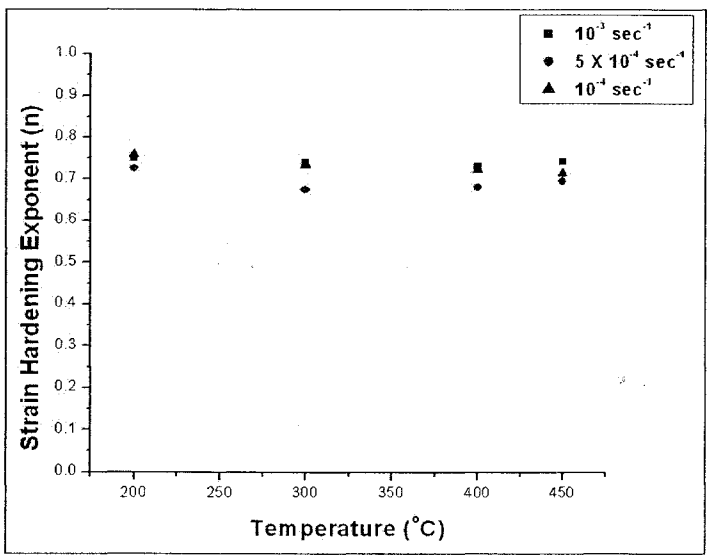

Set 1

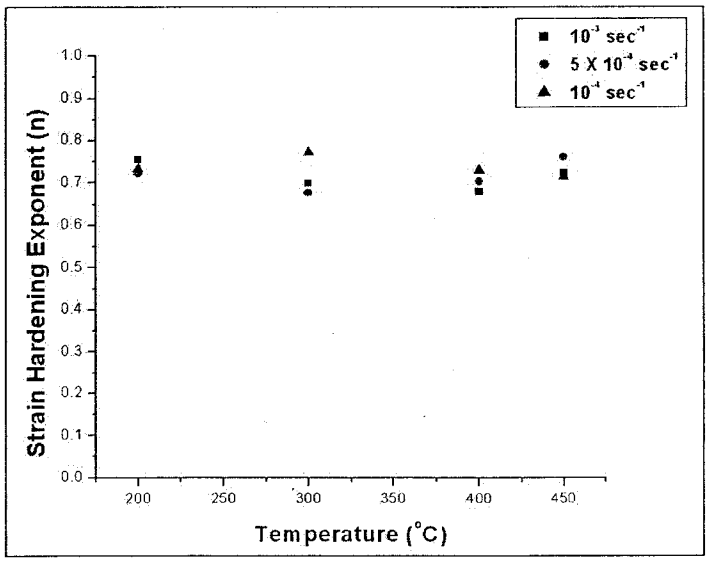

Set 2

APPENDIX B

SCANNING ELECTRON MICROGRAPHS

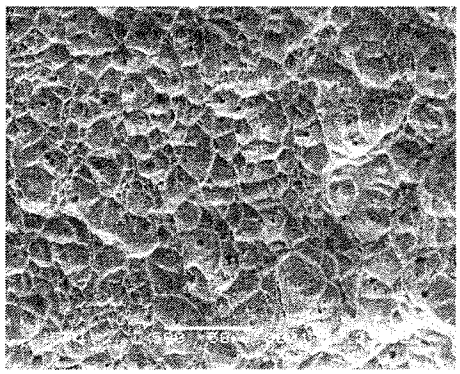

Ambient Temperature, 500X

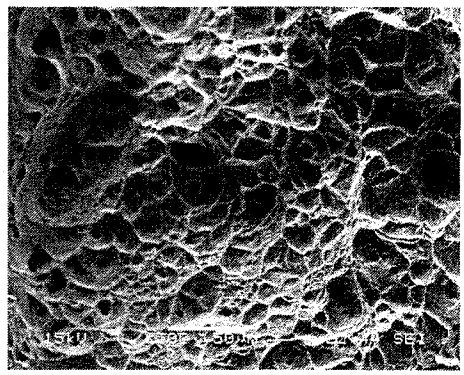

100°C, 500X

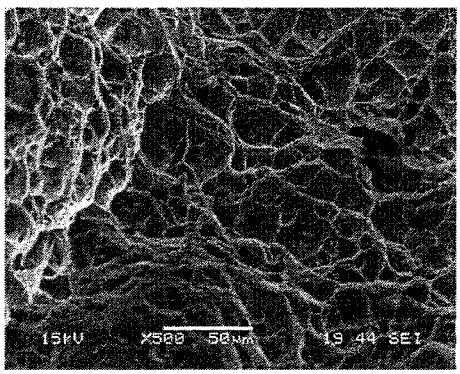

200°C, 500X

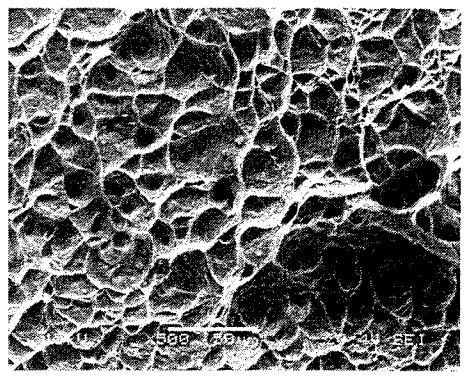

300°C, 500X

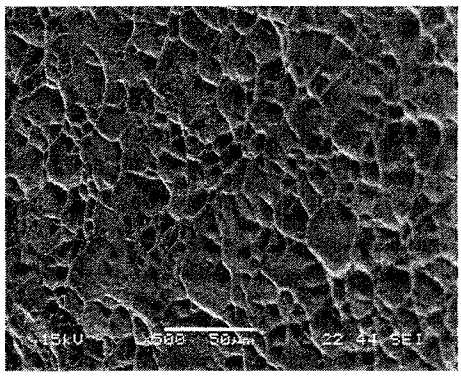

400°C, 500X

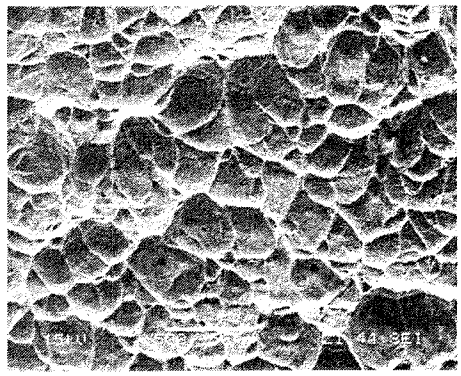

450°C, 500X

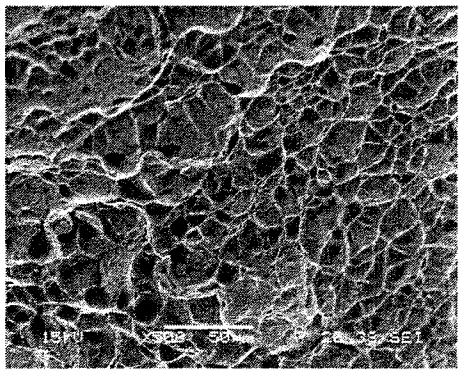

600°C, 500X

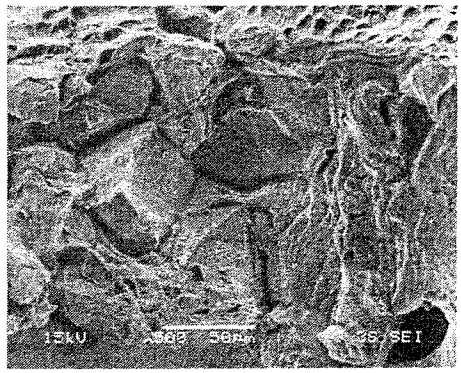

700°C, 500X

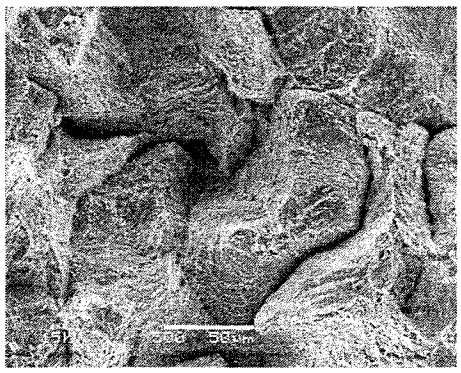

800°C, 500X

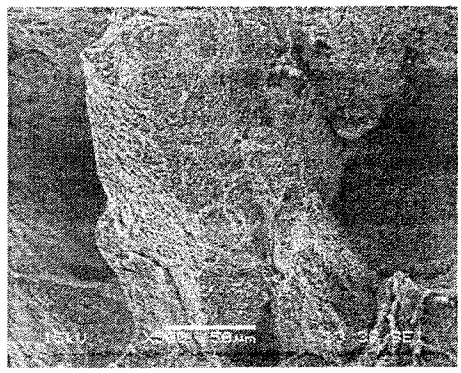

900°C, 500X

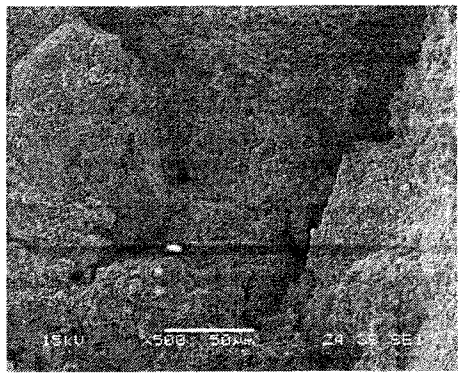

1000°C, 500X

APPENDIX C

TRANSMISSION ELECTRON MICROGRAPHS

C1 TEM Micrographs of Specimen Tested at Room Temperature

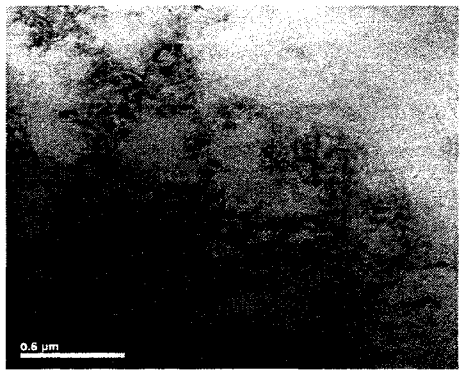

17000X

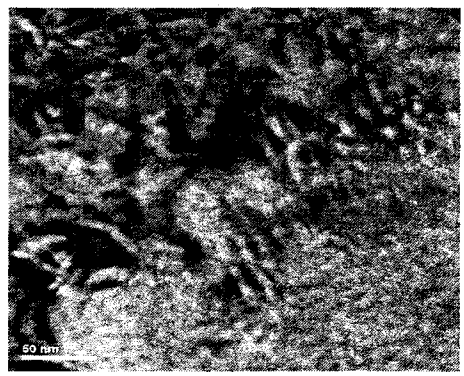

120000X

C2 TEM Micrographs of Specimen Tested at 100°C

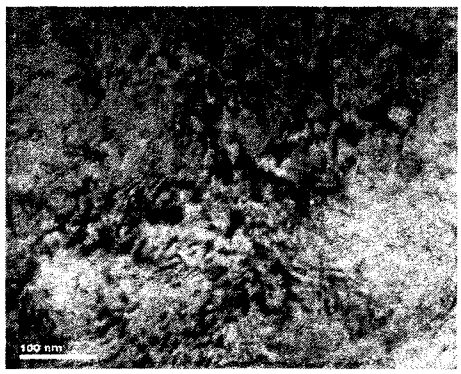

63000X

63000X

C3 TEM Micrographs of Specimen Tested at 200°C

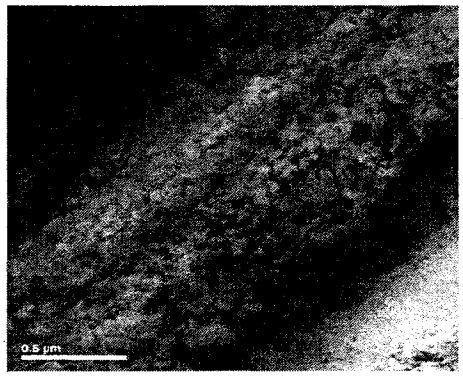

17000X

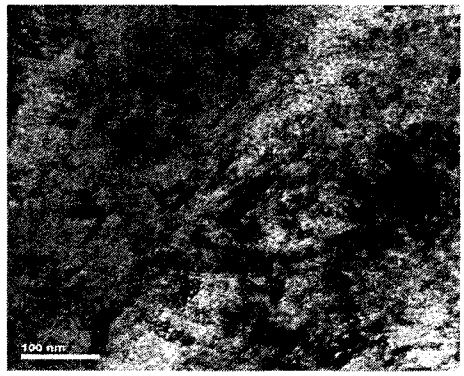

63000X

C4 TEM Micrographs of Specimen Tested at 300°C

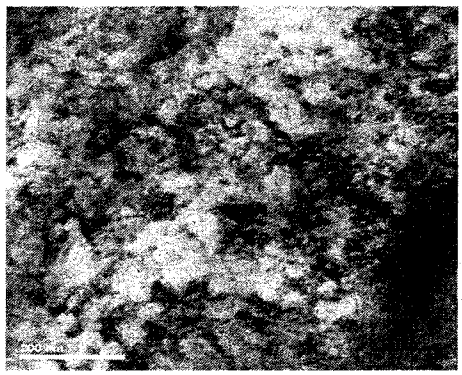

42000X

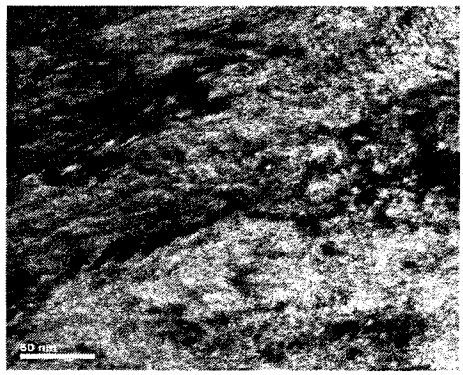

120000X

C5 TEM Micrographs of Specimen Tested at 450°C

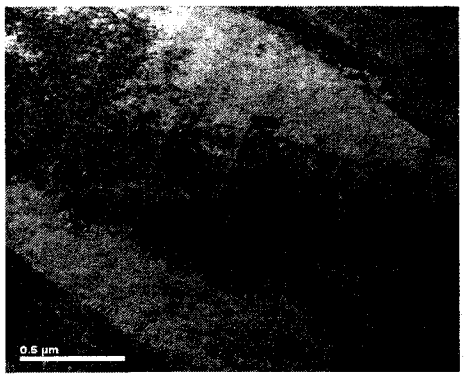

17000X

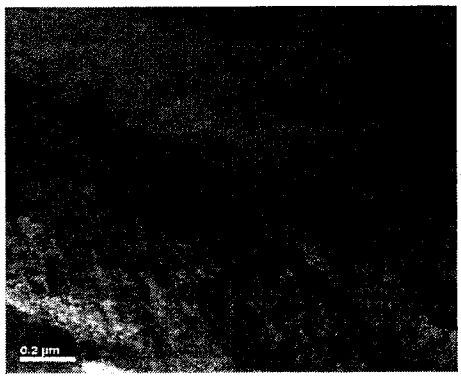

22500X

APPENDIX D

UNCERTAINTY ANALYSES OF EXPERIMENTAL RESULTS

A precise method of estimating uncertainty in experimental results has been presented by Kline and McClintock. The method is based on a careful specification of the uncertainties in the various primary experimental measurements. [60]

When the plus or minus notation is used to designate the uncertainty, the person making this designation is stating the degree of accuracy with which he or she believes the measurement has been made. It is notable that this specification is in itself uncertain because the experiment is naturally uncertain about the accuracy of these measurements.

If a very careful calibration of an instrument has been performed recently, with standards of very high precision, then the experimentalist will be justified in assigning a much lower uncertainty to measurements than if they were performed with a gage or instrument of unknown calibration history. [60]

Most of the instruments in the Materials Performance Laboratory (MPL) were calibrated on a regular basis by Bechtel Nevada using standards with very high precision. Thus, it is expected that the resultant data presented in this thesis would have very insignificant uncertainty. The uncertainties in the results of this investigation are

calculated by using the Kline and McClintock Method. The equation used for this method is given below. [60]

$$W_R = \left[\left(\frac{\partial R}{\partial x_1} w_1 \right)^2 + \left(\frac{\partial R}{\partial x_2} w_2 \right)^2 + \cdots + \left(\frac{\partial R}{\partial x_n} w_n \right)^2 \right]^{\frac{1}{2}} \qquad \text{Equation 1}$$

Where, W_R = the uncertainty in the results

R = the given function of the independent variables $x_1, x_2, \ldots\ldots x_n$)

$R = R(x_1, x_2, \ldots\ldots x_n)$

$w_1, w_2, \ldots\ldots w_n$ = the uncertainty in the independent variables

E1 Uncertainty Calculation in Instron Results

The results generated from the MTS testing are stress (σ), percentage elongation (%El), and percentage reduction in area (%RA). The stress is based on the load (P) and the initial cross-sectional area (A_i) of the tested specimen. The %El is based on the change in length (Δl) during the testing and the %RA is based on the initial and final cross-sectional areas (A_i and A_f). The magnitude of P was obtained from the load-cell of the Instron unit. The values for Δl, A_i, and A_f were calculated based on measurements by a caliper. The uncertainties in load-cell and caliper were ± 0.03% lbs and ± 0.001 inch, respectively, obtained from the calibration. The uncertainty in the initial notched diameter was ± 0.001, which was provided by the manufacturer and the uncertainty in the final notched diameter was ± 0.001 obtained by using the caliper.

E1.1 Calculation of Uncertainty in Stress ($_u\sigma$)

$_u\sigma = {}_u(P, A_i)$

$_uA_i = (uD_i)^2$

Uncertainty in load-cell $= \pm 0.03\%$ lb

Uncertainty in caliper $= \pm 0.001$ inch.

Sample calculation:

For yield stress (YS) $= 50.6$ ksi

Uncertainty in load ($_uP$) $= 2514 \times 0.0003$

$= \pm 0.7542$

Uncertainty in cross-sectional area ($_uA_i$) for the smooth tensile specimen:

Initial Diameter (D_i) $= 0.2515$ inch.

Uncertainty in diameter ($_uD$) $= \pm 0.001$ inch.

$$\text{Area } (A_i) = \frac{\pi D_i^{\,2}}{4}$$

$$= 0.0497 \text{ inch}^2$$

$$\frac{dA_i}{dD_i} = \frac{\pi D_i}{2}$$

$$= 0.395$$

$$\text{Uncertainty in area, } {}_uA_i = \left[\left(\frac{dA_i}{dD_i} \cdot {}_uD_i\right)^2\right]^{\frac{1}{2}}$$

$$= 0.395 \times 0.001$$

$$= \pm 0.000395$$

Uncertainty in stress, $${}_u\sigma = \left[\left(\frac{\partial\sigma}{\partial P}\cdot {}_uP\right)^2 + \left(\frac{\partial\sigma}{\partial A_i}\cdot {}_uA_i\right)^2\right]^{\frac{1}{2}}$$ Equation 1-1

$$\sigma = \frac{P}{A_i}$$

$$\frac{\partial\sigma}{\partial P} = \frac{1}{A_i}$$

$$= 20.121$$

$$\frac{\partial\sigma}{\partial A_i} = -\frac{P}{A_i^2}$$

$$= -1017776.68$$

Now providing all the numerical values in Equation 1-1 obtained from the calculation, it is found that,

$${}_u\sigma = \left[(20.121\times 0.7542)^2 + (-1017776.68\times 0.000395)^2\right]^{\frac{1}{2}}$$

$$= 402.31 \text{ psi}$$

$$= \pm 0.40 \text{ ksi}$$

One example of the use of the uncertainty analysis is shown in this section. This can be implemented to all experimental results discussed in this thesis.

E1.2 Calculation of Uncertainty in Percentage Elongation ($_u$%El)

Sample calculation:

Change in length (Δl) = 0.83 inch.

Gage length (l) = 1 inch.

$$\%El = \frac{\Delta l}{l}\cdot 100$$

Uncertainty in Δl ($_u\Delta$l) = $\pm$ 0.001

Uncertainty in %El ($_u$%El),

$$ {}_u\%El = \left[\left(\frac{d\%El}{d\Delta l} \cdot {}_u\Delta l \right)^2 \right]^{\frac{1}{2}} \qquad \text{Equation 1-2} $$

$$ \frac{d\%El}{d\Delta l} = \frac{100}{l} $$

$$ = 100 $$

Providing all the calculated values in Equation 1-2, it is found that,

$$ {}_u\%El = \left[(100 \times 0.001)^2 \right]^{\frac{1}{2}} $$

$$ {}_u\%El = \pm 0.1 $$

One example of the use of the uncertainty analysis is shown in this section. This can be implemented to all experimental results discussed in this thesis.

E1.3 Calculation of Uncertainty in Percentage Reduction in Area ($_u$%RA)

Sample calculation:

For %RA = 74.7%

Uncertainty in initial cross-sectional area ($_uA_i$) for the smooth specimen:

Initial Diameter (D_i) = 0.2515 inch.

Uncertainty in initial diameter,

$$ ({}_uD_i) = \pm 0.001 \text{ in} $$

$$ \text{Area } (A_i) = \frac{\pi D_i^{\,2}}{4} $$

$$ = 0.0497 \text{ inch}^2 $$

$$\frac{dA_i}{dD_i} = \frac{\pi D_i}{2}$$

$$= 0.395$$

Uncertainty in initial cross-sectional area,

$${}_u A_i = \left[\left(\frac{dA_i}{dD_i} \cdot {}_u D_i \right)^2 \right]^{\frac{1}{2}}$$

$$= 0.395 \times 0.001$$

$$= \pm 0.000395$$

Uncertainty in final cross-sectional area ($_uA_f$) for the smooth specimen:

Final Diameter (D_f) = 0.1265 inch.

Uncertainty in final diameter ($_uD_f$),

$$= \pm 0.001 \text{ inch.}$$

$$\text{Area } (A_f) = \frac{\pi D_f^{\,2}}{4}$$

$$= 0.01257 \text{ inch}^2$$

$$\frac{dA_f}{dD_f} = \frac{\pi D_f}{2}$$

$$= 0.1987$$

Uncertainty in final cross-sectional area,

$${}_u A_f = \left[\left(\frac{dA_f}{dD_f} \cdot {}_u D_f \right)^2 \right]^{\frac{1}{2}}$$

$$= 0.1987 \times 0.001$$

$$= 0.0001987$$

Uncertainty in ${}_u$%RA,

$$ {}_u\%RA = \left[\left(\frac{\partial \%RA}{\partial A_i} \cdot {}_u A_i \right)^2 + \left(\frac{\partial \%RA}{\partial A_f} \cdot {}_u A_f \right)^2 \right]^{\frac{1}{2}} \qquad \text{Equation 1-3} $$

$$ \%\text{RA} = \left(\frac{A_i - A_f}{A_i} \right) \times 100 $$

$$ = \left(1 - \frac{A_f}{A_i} \right) \times 100 $$

$$ \frac{\partial \%RA}{\partial A_i} = \frac{100 A_f}{A_i^{\,2}} $$

$$ = 508.89 $$

$$ \frac{\partial \%RA}{\partial A_f} = -\frac{100}{A_i} $$

$$ = -2012.07 $$

Now assigning all the calculated values in Equation 1-3, it is found that,

$$ {}_u\%RA = \left[(508.89 \times 0.000395)^2 + (-2012.07 \times 0.0001987)^2 \right]^{\frac{1}{2}} $$

$$ = 0.45 $$

One example of the use of the uncertainty analysis is shown in this section. This can be implemented to all experimental results discussed in this thesis.

BIBLIOGRAPHY

1. Haynes International Inc.
2. Pankaj Agarwal and A.H. Shabaik, "High temperature deformation of Hastelloy C-276", Proceedings of the Third International Symposium, September 1976, pp. 237-244.
3. Special Metals Corporation, "Technical Bulletin – Inconel Alloy C-276", Products – Alloy Portfolio.
4. R. Kishore, R.N. Singh, T.K. Sinha and B.P. Kashyap, "Effect of Dynamic Strain Ageing on the Tensile Properties of a modified 9Cr-1Mo Steel", Journal of Materials Science, vol. 32, 1997, pp. 437-442.
5. Y. Ilino and M. Nakahara, "Effect of High Temperature Plastic Strain with Dynamic Strain Ageing on Sensitization of Type 304 Stainless Steel", Journal of Materials Science, vol. 26, no. 21, 1991, pp. 5904-5910.
6. K.G. Samuel, S.L. Mannan and P. Rodriguez, "Serrated Yielding in AISI 316 Stainless Steel", Acta Metallurgica, vol. 36, no. 8, 1988, pp. 2323-2327.
7. S.L. Mannan, K.G. Samuel and P. Rodriguez, "Dynamic Strain Ageing in Type 316 Stainless Steel", Trans. Indian Inst. Met., vol. 36, no. 4, 1983, pp. 313-320.
8. Vani Shankar, M. Valsan, K. Bhanu Shanakara Rao and S.L. Mannan, "Effects of Temperature and Strain Rate on Tensile Properties and Activation Energy for Dynamic Strain Aging in Alloy 625", Metallurgical and Materials Transactions. A, vol. 35A, no. 9, 2004, pp. 3129-3139.

9. Soon H. Hong, Hee Y. Kim, Jin. S. Jang and Il H. Kuk, "Dynamic Strain Aging Behavior of Inconel 600 Alloy", Superalloys, 1996, The Minerals, Metals and Materials Society.

10. A. Girones, L. Llanes, M. Anglada and A. Mateo, "Dynamic Strain Aging Effects on Super duplex Stainless Steels at Intermediated Temperatures", Material Science and Engineering A, 2004, pp. 322-328.

11. Kaiping Peng, Kuangwu Qian and Wenzhe Chen, "Effect of Dynamic Strain Aging on High Temperature Properties of Austenitic Stainless Steel", Materials Science and Engineering A, 2004, pp. 372-377.

12. H.M. Tawancy, N.M. Abbas and A.I.Al Mana, "Thermal Stability of Advanced Ni-base Superalloys", Journal of Materials Science, vol. 29, 1994, pp. 2445-2458.

13. Metallography and Microstructures, "Role of Elements in Superalloys", ASM Handbook, vol. 9, pg. 309, table 7.

14 Fry Steel Company.

15. ASTM Designation E 8-2004, "Standard test methods for tensile testing of metallic materials", American Society for Testing and Materials (ASTM) International.

16. ASTM Designation E 399-1999, "Standard Test Method for Linear-Elastic Plane-Strain Fracture Toughness K_{IC} of Metallic Materials," American Society for Testing and Materials (ASTM) International.

17. ASTM Designation E 1820-2001, "Standard Test Method for Measurement of Fracture Toughness," American Society for Testing and Materials (ASTM) International.

18. ASTM Designation E 647-2000, "Standard Test Method for Measurement of Fatigue Crack Growth Rates," American Society for Testing and Materials (ASTM) International.

19. NACE Standard Double-Cantilever-Beam Test, 1990. NACE Standard TM0177-90, Method D, NACE International, Houston, TX, pp. 17–22.

20. ASTM Designation G 38-2001, "Standard Practice for Making and Using C-Ring Stress-Corrosion Test Specimens," American Society for Testing and Materials (ASTM) International.

21. ASTM Designation G 30-1997, "Standard Practice for Making and Using U-Bend Stress-Corrosion Test Specimens," American Society for Testing and Materials (ASTM) International.

22. Fast Track 8800, "Bluehill 2 Software", Instron Material Testing Systems.

23. Instron Testing Systems, "Specifications – Model 8862", Dynamic and Fatigue Test Systems – High Precision Electric Actuator Systems.

24. L.H. de Almeida and P.R.O. Emygdio, "Activation Energy Calculation and Dynamic Strain Aging in Austenitic Stainless Steel", Scripta Metallurgica et Materialia, vol. 31, no. 5, 1994, pp. 505-510.

25. P. Rodriguez, "Serrated plastic Flow", Bulletin of Materials Science, vol. 6, 1984, pp. 653-664.

26. P.G. McCormick, "A Model for the Portevin-Le-Chatelier Effect in Substitutional Alloys", Acta Metallurgica, vol. 20, 1972, pg. 351.

27. V. Raghavan, "Mechanical Properties" Physical Metallurgy, Chapter 5, pp. 141-146.

28. Key To Steel, "True Stress – True Strain Curve", Article, The Steel Database.

29. K.G. Samuel, "Limitations of Hollomon and Ludwigson Stress-Strain Relations in Assessing the Strain Hardening Parameters", Journal of Physics D, vol. 39, 2006, pp. 203-212.

30. Hollomon H., Trans. AIME, vol. 162, 1945, pg. 268.

31. K.G. Samuel, S.L. Mannan and V.M. Radhakrishnan, "The Influence of Temperature and Prior Cold Work on the Strain-hardening Parameters of a Type 316 LN Stainless Steel", International Journal of Pressure Vessel and Piping, vol. 52, 1992, pp. 151-157.

32. E. Issac Samuel, B.K. Chowdhary and K. Bhanu Sankara Rao, "Influence of Temperature and Strain Rate on Tensile Work Hardening Behaviour of Type 316 LN Austenitic Stainless Steel", Scripta Materialia, vol. 46, 2002, pp. 507-512.

33. Ludwigson D.C., "Modified Stress-strain Relation for FCC Metals and Alloys", Metallurgical and Materials Transactions A, vol. 2, no. 10, 1971, pp. 2825-2828.

34. Choudhary B.K. Ray, S.K. Bhanu Sankara Rao K and Mannan S.L., Berg Huttenmann Monatsh, vol. 137, 1992, pp. 439-445.

35. P.P. Date and K.A. Padmanabhan, "Deformation behaviour of Sheets of Three Aerospace Al-Alloys", Journal of Materials Processing Technology, vol. 112, 2001, pp. 68-77.

36. A.K. Roy, D.L. Fleming, D.C. Freeman and B.Y. Lum, "Stress Corrosion Cracking of Alloy C-22 and Ti Gr-12 Using Double-cantilever-beam Technique", Micron, vol. 30, 1999, pp. 649-654.

37. Vinay Virupaksha, "Use of Alloy 800H for Applications in Hydrogen Generation using Nuclear Power", M.S. Thesis, Department of Mechanical Engineering, University of Nevada, Las Vegas, Spring 2006.

38. Mars G. Fontana, "Corrosion Principles", Corrosion Engineering, Chapter 2, pp. 13-14.

39. Buehler Limited, "Nickel and Alloys", Commonly Used Etchants for Metals and Alloys, An Article on Etching.

40. Metallography and Microstructures, "Microetchants for Wrought Heat-resistant Alloys", ASM Handbook, vol. 9, pg. 308, table 4.

41. Longzhou Ma, "Comparison of Different Sample Preparation Techniques in TEM Observation of Microstructure of Inconel Alloy 783 Subjected to Prolonged Isothermal Exposure", Micron, vol. 30, 2004, pp. 273-279.

42. Paul E. Fischione, "Materials Specimen Preparation for Transmission Electron Microscopy", E.A.Fischione Instruments, Inc. Export, PA, USA.

43. Subhra Bandyopadhyay, "Residual Stress Characterization and Defects Analyses by Microscopy", M.S. Thesis, Department of Mechanical Engineering, University of Nevada, Las Vegas, Fall 2005.

44. Metallography and Microstructures, ASM Handbook, vol. 9, pg. 308, table 5.

45. Kozue Yabusaki and Hirokazu Sasaki, "Specimen Preparation Technique for a Microstructure Analysis Using the Focused Ion Beam Process", Furukawa Review, no. 22, 2002.

46. Hirsch P., Howie A., Nicholson R., Pashley D.W., Whelan M.J., "Electron Microscopy of Thin Crystals", Malabar, Krieger Publishing Company, 1977.

47. Loretto M.H., "Electron Beam Analysis of Materials", London, Chapman and Hall, 1994.

48. J. Pesicka, R. Kuzel, A. Dronhofer and G. Eggeler, "The Evolution of Dislocation Density During Heat Treatment and Creep of Tempered Martensitic Ferritic Steels", Acta Materialia, vol. 51, issue 16, 2003, pp. 4847-4862.

49. R.F. Egerton, "Electron Energy Loss Spectroscopy in Electron Microscope", Plenum Press, 1986, pp. 291-352.

50. International Centre for Diffraction Data (ICDD), "Chromium Cobalt Molybdenum Carbide", Reference Code: 00-037-1229.

51. ICDD, "Cobalt Molybdenum", Reference Code: 00-029-0489.

52. M. Raghavan, B.J. Berkowitz and J.C. Scanlon, "Electron Microscopic Analysis of Heterogeneous Precipitates in Alloy C-276", Metallurgical and Materials Transactions. A, vol. 13A, no. 6, 1982, pp. 979-984.

53. M. Sundararaman, P. Mukhopadhyay and S. Banerjee, "Carbide precipitation in Nickel Base Superalloys 718 and 625 and their effect on Mechanical Properties", Superalloys, 1997, The Minerals, Metals and Materials Society.

54. W.V. Youdelis and O. Kwon, "Carbide Phases in Cobalt Base Superalloy: Role of Nucleation Entropy in Refinement", Metal Science, vol. 17, 1983, pp. 379-384.

55. H.M. Tawancy, "Precipitation Characteristics of μ-phase in Wrought Nickel-Base Alloys and its Effect on Their Properties", Journal of Materials Science, vol. 31, 1996, pp. 3929-3936.

56. Mean Free Path Calculation, "The Inelastic Mean Free Path of Electrons in Solids", Surface and Interface Science.

57. Paul J. Schields, "Bragg's Law and Diffraction: How waves reveal the Atomic Structure of Crystals", Center for High Pressure Research, Department of Earth & Space Sciences, State University of New York, Stony Brook, NY 11794, November 2004.

58. V. Raghavan, "Mechanical Properties", Chapter 5, Physical Metallurgy, pp. 164-165.

59. Metallography and Microstructures, "Wrought Heat-resistant Alloys", ASM Handbook, vol. 9, pp. 314-329.

60. Jack P. Holman, "Experimental Methods for Engineers," McGraw-Hill Book Company, 4th Edition, pg. 50

VITA

Graduate College
University of Nevada, Las Vegas

Joydeep Pal

Local Address:
1173 Maryland Circle, Apt # 3
Las Vegas, NV 89119

Degrees:
Bachelor of Science in Mechanical Engineering, 2000
Jadavpur University,
Kolkata, India.

Special Honors and Awards:

- Nevada Beta Chapter of Tau Beta Pi, The Engineering Honor Society, Fall 2006.

Publications:

- Joydeep Pal, Ajit Roy, "Tensile Properties and Corrosion Susceptibility of Alloy C–276 in S–I Environment", presented at the AICHE conference, Oct 30 – Nov 4, 2005, Cincinnati, Ohio.
- Joydeep Pal, Ramasekhar Koripelli and Jagadesh Yelavarthi, "Deformation Characteristics of Nickel-base Alloys at Elevated Temperatures under Tensile Loading", presented at the ANS student conference, March 29 – April 1, 2006, RPI Troy, NY.
- Joydeep Pal, Ajit Roy and et al, "The Corrosion Behavior of Nickel-base Austenitic Alloys for Nuclear Hydrogen Generation", presented at the MRS Spring Meeting, April 20 – 21, 2006, San Francisco, CA.
- Joydeep Pal, Ajit Roy and et al, "High-Temperature Tensile Properties of Nickel-base Alloys for Hydrogen Generation", presented at the SAMPE conference, April 30 – May 4, 2006, Long Beach, CA.
- Joydeep Pal and Ajit Roy, "Tensile Properties and Stress Corrosion Crack Growth Studies of Alloy C-276", presented at the AMPT conference, July 30 – August 3, 2006, Las Vegas, NV
- Joydeep Pal and Ramasekhar Koripelli, "Tensile Properties and Fracture Toughness of Super Alloys for Hydrogen Generation", presented at MS & T 2006, Oct 15 – 19, 2006, Cincinnati, Ohio

Thesis Title: "Tensile Properties, Fracture Toughness and Crack Growth Study of Alloy C-276"

Thesis Examination Committee:

Chairperson, Dr. Ajit K. Roy, Ph. D.
Committee Member, Dr. Anthony E. Hechanova, Ph.D.
Committee Member, Dr. Daniel Cook, Ph. D.
Graduate Faculty Representative, Dr. Edward S. Neumann, Ph.D.